

Energy Level Alignment in Hybrid Bulk Heterojunctions and New Redox Mediators for
Quantum Dot Solar Cells

Andrew J. Haring

Thesis submitted to the faculty of the Virginia Polytechnic Institute and State University
in partial fulfillment of the requirements for the degree of

Master of Science

In

Chemistry

Amanda J. Morris, Chair

John R. Morris

Harry W. Gibson

May 11, 2016

Blacksburg, VA

Keywords: polymer, TiO₂, heterojunction, photovoltaic, redox mediator, polaron

Chapters 2 and 3 © 2014 by American Chemical Society Publications

Appendix Creative Commons Attribution License CC BY 3.0

Energy Level Alignment in Hybrid Bulk Heterojunctions and New Redox Mediators for Quantum Dot Solar Cells

Andrew J. Haring

Abstract

The advancement of quantum dot sensitized solar cell (QDSSC) technology depends on optimizing directional charge transfer between light absorbing quantum dots, TiO₂, and a redox mediator. Kinetically, reduction of oxidized quantum dots by the redox mediator should be rapid and faster than the back electron transfer between TiO₂ and oxidized quantum dots to maintain photocurrent. Thermodynamically, the reduction potential of the redox mediator should be sufficiently positive to provide high photovoltages. To satisfy both criteria and enhance power conversion efficiencies, we introduced charge transfer spin-crossover Mn^{II/III} complexes as promising redox mediator alternatives in QDSSCs. High photovoltages ~1 V were achieved by a series of Mn poly(pyrazolyl)borates, with reduction potentials ~0.51 V vs Ag/AgCl. Back electron transfer rates were slower than Co(bpy)₃, where bpy = 2,2'-bipyridine. This is indicative of a large barrier to recombination imposed by spin-crossover in these complexes. By capitalizing on these characteristics, efficient Mn^{II/III}-based QDSSCs can be achieved with more soluble Mn-complexes.

In hybrid bulk heterojunction solar cells (HBHJs), light-absorbing conjugated polymers are interfaced with films of nanostructured TiO₂. Photovoltaic action requires photoelectrons in the polymer to transfer into the TiO₂, and therefore, polymers are designed with lowest unoccupied molecular orbital levels higher in energy than the conduction band of TiO₂ for thermodynamically favorable electron transfer. Currently, the energy level values used to guide solar cell design are referenced from the separated

materials, neglecting the fact that upon heterojunction formation material energetics are altered. With spectroelectrochemistry, we discovered that spontaneous charge transfer occurs upon heterojunction formation between poly(3-hexylthiophene) (P3HT) and TiO₂. It was determined that deep trap states in TiO₂ accept electrons from P3HT and form hole polarons in the polymer. This equilibrium charge separation alters energetics through the formation of interfacial dipoles and results in band bending that inhibits desired photoelectron injection into TiO₂, limiting HBHJ solar cell performance. New guidelines for improved photocurrent are proposed by tuning the energetics of the heterojunction to reverse the direction of the interfacial dipole, enhancing photoelectron injection.

Attributions

Chapter 2 Mn^{II/III} Complexes as Promising Redox Mediators in Quantum Dot Sensitized Solar Cells

Michelle Pomatto, an undergraduate researcher in Amanda Morris' group, assisted with synthesis, device fabrication, and photovoltaic characterization.

Miranda Thornton, a masters graduate from Amanda Morris' research group, assisted with synthesis and characterization of Mn-complexes.

Reprinted and adapted with permission from Haring, A., Pomatto, M., Thornton, M., and Morris, A. *ACS Applied Materials & Interfaces* **2014** *6*, 15061-15067. Copyright 2014 American Chemical Society.

Chapter 3 Rethinking Band Bending at the P3HT-TiO₂ Interface

Spencer Ahrenholtz, a current doctoral candidate in Amanda Morris' research group, assisted by performing X-ray photoelectron spectroscopy characterization of films.

Reprinted and adapted with permission from Haring, A., Ahrenholtz, S., and Morris, A. *ACS Applied Materials & Interfaces* **2014** *6*, 4394-4401. Copyright 2014 American Chemical Society.

Appendix Controlling Morphological Parameters of Anodized Titania Nanotubes for Optimized Solar Energy Applications

Reprinted and adapted from Haring, A.; Morris, A.; Hu, M. *Materials* **2012**, *5*, 1890-1909. Creative Commons License.

Table of contents

| | |
|--|------|
| Abstract..... | ii |
| Attributions..... | iv |
| Table of Contents..... | v |
| List of Figures..... | vi |
| List of Tables..... | viii |
| | |
| Chapter 1 Introduction..... | 1 |
| | |
| Chapter 2 Mn ^{II/III} Complexes as Promising Redox Mediators in Quantum Dot Sensitized Solar Cells | |
| 2.1 Introduction..... | 15 |
| 2.2 Experimental..... | 17 |
| 2.3 Results and Discussion..... | 20 |
| 2.4 Conclusion..... | 31 |
| 2.5 Supplemental Information..... | 32 |
| | |
| Chapter 3 Rethinking Band Bending at the P3HT-TiO ₂ Interface | |
| 3.1 Introduction..... | 37 |
| 3.2 Experimental..... | 39 |
| 3.3 Results and Discussion..... | 41 |
| 3.4 Conclusion..... | 55 |
| 3.5 Supplemental Information..... | 56 |
| | |
| References..... | 59 |
| | |
| Appendix Controlling Morphological Parameters of Anodized Titania Nanotubes for Optimized Solar Energy Applications..... | A-1 |

List of Figures

| | | |
|------------|---|-----|
| Figure 1-1 | Renewable Energy Sources..... | 1 |
| Figure 1-2 | Solar Cell Generations..... | 2 |
| Figure 1-3 | Schematic of Quantum Dot Sensitized Solar Cells..... | 3 |
| Figure 1-4 | Schematic of Hybrid Bulk Heterojunction Solar Cells..... | 5 |
| Figure 1-5 | Integer Charge Transfer Model..... | 7 |
| Figure 1-6 | TiO ₂ -Quantum Dot Sensitization Methods..... | 10 |
| Figure 1-7 | TiO ₂ Nanostructures Synthesis..... | 11 |
| Figure 1-8 | TiO ₂ Nanotube Arrays vs. Nanoparticle Films..... | 12 |
| Figure 1-9 | Solar Cell Fabrication..... | 14 |
| Figure 2-1 | Quantum Dot Sensitized Solar Cells Charge Transfer Processes..... | 20 |
| Figure 2-2 | UV-Visible Light Absorption Spectra of Redox Mediators..... | 22 |
| Figure 2-3 | Photocurrent-Voltage Plots of Solar Cells Using Mn-Redox Mediators..... | 24 |
| Figure 2-4 | Cyclic Voltammograms of Mn-Redox Mediators..... | 26 |
| Figure 2-5 | Plots of Electron Lifetimes in Solar Cells Using Mn-Redox Mediators..... | 27 |
| Figure 2-6 | Incident-Photon-to-Current Efficiency of Solar Cells..... | 29 |
| Figure 3-1 | Band Diagrams of Possible Energy Alignment Regimes..... | 43 |
| Figure 3-2 | Spectroelectrochemistry of P3HT-TiO ₂ Heterojunctions..... | 45 |
| Figure 3-3 | X-Ray Photoelectron Spectra of P3HT-TiO ₂ Heterojunctions..... | 48 |
| Figure 3-4 | Potential Step Spectroelectrochemistry of P3HT-TiO ₂ | 49 |
| Figure 3-5 | Density of States of TiO ₂ Shallow Traps with P3HT..... | 50 |
| Figure 3-6 | Density of States of TiO ₂ Shallow Traps with Thiophene Derivatives..... | 52 |
| Figure 3-7 | Band Diagrams of Ideal Heterojunction and P3HT-TiO ₂ Heterojunction..... | 53 |
| Figure A-1 | Anodization Setup for Nanotube Formation..... | A-1 |
| Figure A-2 | Solid State TiO ₂ Nanotube Solar Cell..... | A-2 |
| Figure A-3 | Scanning Electron Micrographs of TiO ₂ Nanotubes..... | A-3 |
| Figure A-4 | Nanotube Formation During Anodization..... | A-4 |

| | | |
|-------------|--|------|
| Figure A-5 | Dependence of Nanotube Growth on Water Content and Voltage..... | A-5 |
| Figure A-6 | Dependence of O ₂ Reduction on Nanotube Length..... | A-6 |
| Figure A-7 | Dependence of Solar Cell Efficiency on Nanotube Length..... | A-7 |
| Figure A-8 | Dependence of Nanotube Diameter on Water Content and Voltage..... | A-8 |
| Figure A-9 | Dependence of Solar Cell Efficiency on Nanotube Porosity..... | A-9 |
| Figure A-10 | Dependence of Solar Cell Efficiency on Nanotube Diameter..... | A-10 |
| Figure A-11 | Mixed-TiO ₂ Crystallinity Band Energetics..... | A-12 |
| Figure A-12 | Schematics of TiO ₂ Nanotube Solar Cells | A-13 |
| Figure A-13 | Nanotube Solar Cell Fabrication Process..... | A-14 |
| Figure A-14 | Scanning Electron Micrographs of Nanotubes After Milling..... | A-15 |
| Figure A-15 | Dependence of Solar Cell Efficiency on Nanotube Barrier Layer..... | A-15 |

List of Tables

| | | |
|-----------|--|------|
| Table 2-1 | Figures of Merit for Quantum Dot Sensitized Solar Cells..... | 24 |
| Table A-1 | Range of Anodization Parameters..... | A-4 |
| Table A-2 | Parameters to Achieve Long Nanotubes..... | A-5 |
| Table A-3 | Parameters to Vary Nanotube Diameter..... | A-8 |
| Table A-4 | Anodization Solvent Viscosities..... | A-10 |
| Table A-5 | Dependence of Solar Cell Efficiency on Nanotube Crystallinity..... | A-11 |

Chapter 1. Introduction

Why new solar cells

Alternative energy sources need to become more efficient to contribute to the world's rising energy demands and have less environmental impact than nonrenewable energy sources.^{1,2} Current alternative energy sources for electricity in the United States include solar, geothermal, wind, and hydropower. Although photovoltaics currently contribute to only 1% of the total U.S. electricity, the contribution is expected to dramatically increase in the next 25 years, Figure 1-1.³ For this increase to be feasible, photovoltaics need to become more efficient at converting solar energy to electrical energy while reducing the cost of manufacturing.

Sources of U.S. Electricity Generation, 2012

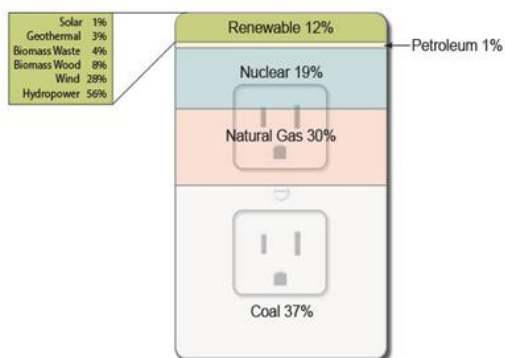


Figure 83. Renewable electricity generation by type, including end-use generation, 2008-2040 (billion kilowatthours)

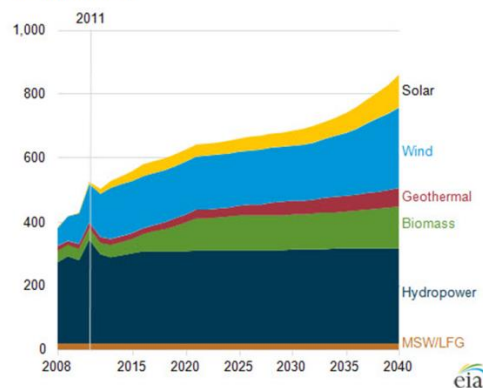


Figure 1-1. Renewable energy sources make up a small but increasing portion of electricity generation. Image from reference 3.

First generation solar cells, based on expensive silicon p-n junctions currently cost around \$4/W and are projected to level off around \$1.50/W, Figure 1-2.⁴ Second generation solar cells employ thin films of cadmium telluride and copper indium gallium selenide (CIGS), a cheaper light absorbing semiconductor, reducing manufacturing costs to \$1.25/W.⁴ Third generation and next

generation solar cells include many types that have the potential to reduce cost even further by employing multiple p-n junctions or high surface area junctions and molecular light absorbers: dye-sensitized solar cells (DSSCs), organic heterojunction solar cells (OBHJs), quantum dot solar cells (QDSCs), and hybrid bulk heterojunction solar cells (HBHJs).⁴ For DSSCs, QDSCs, and HBHJs, the use of cheap and abundant inorganic semiconductors, such as TiO₂ and ZnO, in conjunction with readily synthesized ruthenium polypyridyl, metal chalcogenide, or conjugated polymer light absorbers has been an area of active research.

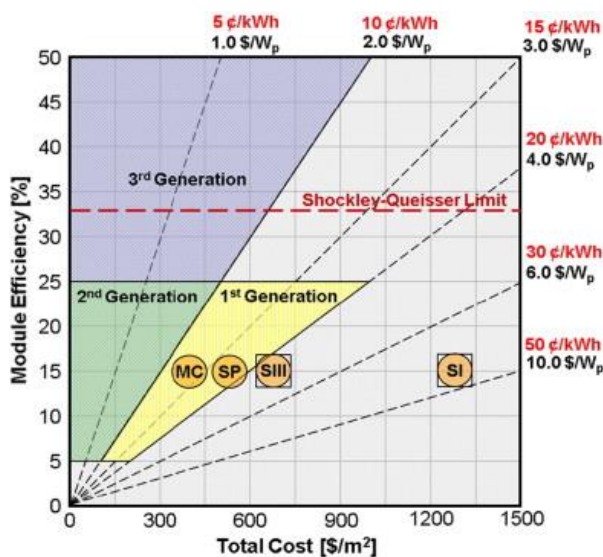


Figure 1-2. Cost efficiencies of solar cells. MC: manufacturing cost, SP: sale price, SIII: utility installed cost, SI: residential installed cost. Reprinted with permission from⁵. Copyright 2009 Elsevier.

Redox mediators in quantum dot sensitized solar cells

In QDSCs, the conversion of light to electrical energy is fundamentally different than in silicon p-n junction solar cells, Figure 1-3. Metal chalcogenide quantum dots, adsorbed to a mesoporous crystalline semiconductor, e.g., TiO₂, ZnO, absorb photons, and electrons are excited

from the valence band (VB) to conduction band (CB).^{11,12} The photoelectrons are injected into the CB of the metal oxide, which is lower in energy than the quantum dots' CB.¹¹ The electrons travel through the metal oxide, across particle and grain boundaries, and into fluorine-doped tin oxide (FTO-glass).¹¹ After passing through the external circuit, the electrons reduce the redox mediator at a catalytic counter electrode, such as platinum.^{11, 12} To complete the cycle, reduced redox mediator species diffuse to the oxidized quantum dots, where they replenish the oxidized VB.^{11,12}

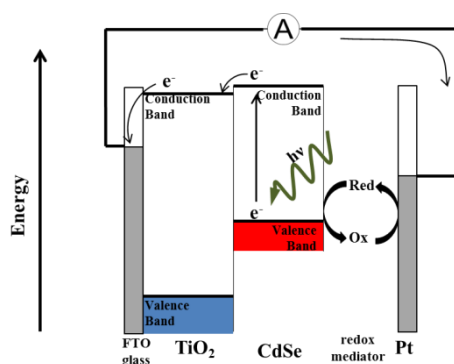


Figure 1-3. Schematic of a typical QDSC: Photoelectrons in light-absorbing quantum dots (CdSe) inject into TiO₂ and are transported to the FTO-glass electrode. Electrons in the quantum dot valence band are replenished by the reduced form of the redox mediator. Figure is the author's work.

The undesired recombination of electrons from the TiO₂ or ZnO CB with oxidized forms of the quantum dots and redox mediator presents a challenge in maximizing the efficiency of QDSCs. Systematically redeveloping and tuning the redox mediator can minimize unfavorable recombination processes by kinetically selecting the favorable processes, e.g., fast quantum dot-regeneration kinetics and slow reduction by electrons in TiO₂ or ZnO. Partly for its favorable recombination kinetics, iodide/triiodide has historically been employed as the most common redox mediator.⁶ However, it has several drawbacks, including an unfavorable redox potential (0.34 V

vs NHE), competing light absorption, the formation of the diiodide radical, and the inability to tune its redox potential.⁶

Within the past decade, outer-sphere metal complexes have demonstrated their advantages as redox mediators in DSSCs.⁷ In particular, cobalt bipyridine complexes absorb minimal light, have tunable redox potentials by changing ligands, and have led to solar cell efficiencies >12% when coupled with expensive ruthenium-based dyes.⁸ In contrast, the efficiency of QDSCs is currently limited to <8% using sulfide/polysulfide as the redox mediator.⁹ However, alternative redox mediators for QDSCs have not been investigated and, therefore, one of my research goals is to design and characterize metal complexes for redox mediators to improve their efficiency. Manganese pyrazolborate complexes undergo a low-spin to high-spin crossover upon reduction of Mn^{III} to Mn^{II}, providing an energetic barrier that should slow the unfavorable reduction of Mn^{III} species by photoelectrons in TiO₂.¹⁰

Energy level alignment in hybrid bulk heterojunction solar cells

Hybrid bulk heterojunction solar cells (HBHJs) operate in a similar manner to QDSCs except that a light-absorbing conjugated polymer replaces the function of quantum dots and redox mediators.¹¹ Photoelectrons in the polymer, such as poly(3-hexylthiophene) (P3HT), inject into the CB of a nanostructured metal oxide (TiO₂/ZnO) where they are collected by FTO-glass and enter the external circuit, Figure 1-4. Holes are transported from the polymer-metal oxide heterojunction, through the polymer layer, and recombine with electrons at the gold counter electrode. The alignment of polymer and TiO₂ energy levels for thermodynamically favorable photoelectron transfer is paramount for HBHJ device function.¹¹

However, an accurate model of the heterojunction energetics is not typically employed when designing polymers with optimum energy levels. Salaneck et al. recently

developed the Integer Charge Transfer (ICT) model relevant to heterojunctions with polymers, but it has not yet been used for HBHJs.¹²

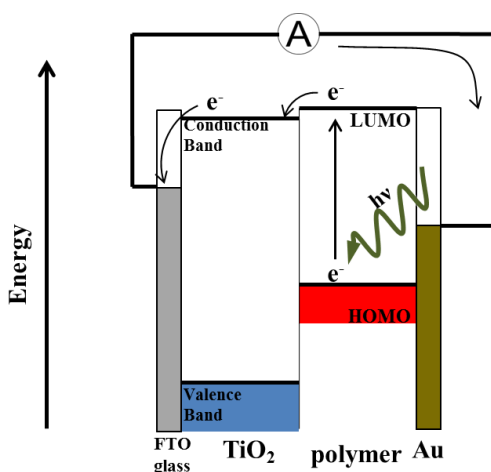


Figure 1-4. Schematic of a typical HBHJ: Electron-hole pairs, excitons, are created in the light-absorbing polymer. If the exciton reaches TiO₂ before recombination, the electron transfers into the electron acceptor and is transported to the FTO-glass electrode, producing photocurrent. Figure is the author's work.

Currently used models for ideal energy alignment in HBHJs

Upon illumination, photoelectrons in the LUMO energy level of the polymer are electrostatically bound to the hole created in the HOMO by 0.1-0.3 eV.¹¹ The LUMO energy level must be situated at least 0.3 eV above the conduction band of TiO₂, E_{CB} , for efficient electron transfer from the polymer into TiO₂.^{13,14} At the same time, a larger energy gap between E_{CB} and the polymer HOMO energy level allows for greater photovoltage. However, the polymer's optical energy gap must also be optimized to absorb sufficient sunlight (~1.6-2.0 eV). Therefore, ideal materials have a $\Delta E_{LUMO-CB} \geq 0.3$ eV while maintaining highest $\Delta E_{CB-HOMO} (>1$ eV). This ideal energy alignment imposes requirements on both materials and provides general guidelines for synthetically designing light absorbing polymers. Thus, synthesizing polymers with different

energetic characteristics has garnered much attention in pursuit of HBHJs delivering high power conversion efficiencies.^{15,16,17,11,18}

However, materials' energetics shift upon formation of a heterojunction and this complicates the application of these general guidelines. For example, at inorganic semiconductor p-n junctions, two inorganic semiconductors with different Fermi levels (E_F) are contacted, leading to charge transfer and the creation of an interfacial dipole that shifts energy levels at the interface (vacuum level offset).¹⁹ At thermodynamic equilibrium, the Fermi level (chemical potential of electrons) must be constant throughout the semiconductor junction.¹⁹ Before equilibrating, when two semiconductors with different Fermi levels come into electrical contact, there will be an initial chemical potential gradient at the interface; electrons spontaneously transfer down the gradient, from the semiconductor with higher E_F into the semiconductor with lower E_F .^{19,20} Thermodynamic equilibrium is attained when the new charge distribution creates an electric field, extending distances up to and beyond 100 nm either side of the interface (interfacial dipole), that prevents further electron transfer.^{19,21} Since the conduction and valence band represent the potential energy of electronic states, in the region of the electric field they bend upwards or downwards in energy.

Integer charge transfer model applied to HBHJs

Charge transfer and band bending can also occur at the interfaces of polymers with nanoparticulate TiO_2 , but the model of inorganic semiconductors cannot be directly applied.^{22,23,24} Whereas in semiconductor junctions, energy level alignment is determined by the initial Fermi level gradient at the interface, in TiO_2 -polymer junctions it is determined by the TiO_2 Fermi level and the polaronic levels in the polymer (E_{CT+} , E_{CT-}), Figure 1-5.^{12,25} Adding excess electrons or holes to organic materials distorts the molecular geometry, and the excess charge couples with the relaxed geometry, creating polarons with energies in the HOMO-LUMO gap.²⁶ Charge transfer

and band bending occur when polaron formation is thermodynamically favorable (vacuum level offset), Figure 1-5a,c.^{12,25} Forming hole polarons in the polymer leads to upward band bending, which inhibits photoelectron injection into the TiO₂, Figure 1-5a. In contrast, forming electron polarons in the polymer improves photoelectron injection into the TiO₂ Figure 1-5c. However, within the solar cell research community, no charge transfer is assumed to occur at polymer-TiO₂ heterojunctions, with no justification, as in Figure 1-5b.

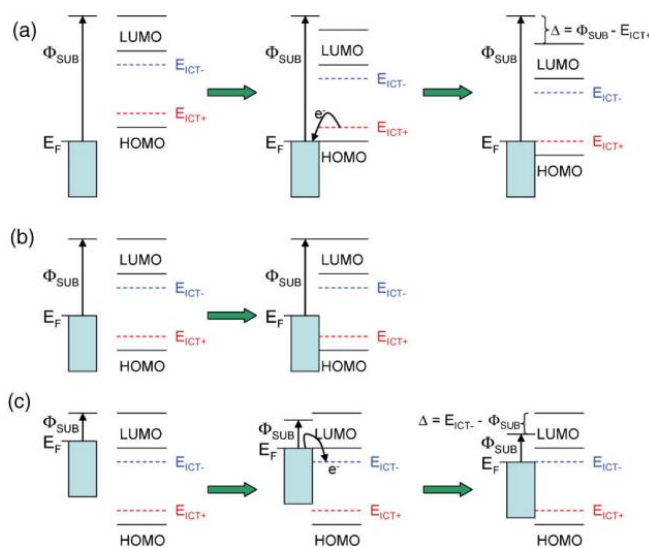


Figure 1-5. Illustration of the Integer Charge Transfer model. Energy level alignment lead to a) hole polaron formation in the polymer and a vacuum level shift, Δ , b) no charge transfer or vacuum level shift, or c) electron polaron formation a vacuum level shift in the opposite direction. Band bending is not illustrated in this simplified diagram but still exist. Reprinted with permission from¹². Copyright 2009 Wiley.

Synthesis and fabrication of solar cells

In HBHJs and QDSCs, conjugated polymers or quantum dots absorb visible light while TiO₂ or ZnO collects electrons. In HBHJs the conjugated polymer can also act as the hole transport layer, carrying holes away from the semiconductor and to a counter electrode such as gold. In QDSCs, a liquid redox mediator reduces the quantum dot and oxidized species diffuse to the counter electrode.

Polymers as hole-transporters and light absorbers

The discovery and advancement of conductive light absorbing polymers, such as P3HT, enabled them to serve as both the sensitizer and the hole conductor, taking the place of dyes and electrolytes in DSSCs.^{17, 18, 27} The light absorbance, electron-hole pair separation, and hole conductivity can be adjusted to optimize hybrid BHJs.²⁸ The HOMO-LUMO gap can be adjusted to tune the absorbance spectrum to match the solar spectrum, while dipole features help separate excitons and reduce geminate recombination.²⁸ When excitons reach the polymer-semiconductor interface, the electric field from the LUMO-conduction band gap separates the exciton into a free electron in the semiconductor and a free hole in the polymer. Excitons in the polymer typically have binding energies on the order of 0.1 eV and a 0.3 eV gap is generally sufficient to separate the exciton and provide the driving force for electrical current to flow into the semiconductor.²⁸ An energy gap greater than 0.3 eV is wasted as thermal energy, although there is greater driving force for photocurrent to flow.

Quantum dots as light absorbers

Metal chalcogenide quantum dots are synthesized by three routes including a hot injection method, a solvothermal method and a Successive Ionic Layer Adsorption and Reaction method (SILAR), Figure 1-6.^{28, 38, 39} The hot injection method uses cadmium oxide and selenium-trioctylphosphine (Se-TOP) precursors.²⁸ The cadmium oxide is

dissolved in a high temperature solvent (trioctylphosphine oxide) at 320°C under nitrogen and the Se-TOP is injected into the solution.²⁸ The quantum dots' size and absorbance spectra depend on the growth time (15-90 seconds) and ranges from 2-5 nm with optical absorbance peaks between 500 and 600 nm.²⁸ The solvothermal method uses cadmium oleate dissolved in toluene and Se-TOP precursors. The solution is heated at 180°C for one to three hours to form quantum dots with absorbance peaks between 500 and 600 nm.

By soaking TiO₂ films in mercaptopropanoic acid, MPA, or other thiol carboxylic acids, and subsequently soaking in the quantum dot solution, TiO₂ nanostructures are sensitized by the adsorption of colored CdSe quantum dots. The linker molecules are adsorbed to the quantum dots through thiol moieties and to the semiconductor through carboxylic acid moieties.^{29, 30}

To eliminate the need for linker molecules which impede electron transport, the CdSe quantum dots can be directly adsorbed to TiO₂ by electrophoretic deposition (EPD), Figure 1-6.³¹ Many quantum dots have an unequal amount of Cd²⁺ and Se²⁻ and are therefore charged. By applying ~70 volts between two TiO₂ films in a solution of CdSe quantum dots in a toluene/acetonitrile mixture, the charged quantum dots are adsorbed to the TiO₂ electrodes, producing opaque CdSe films.³¹

In contrast, the SILAR method grows the CdSe quantum dots directly on TiO₂ through a layer-by-layer reaction, Figure 1-6.³⁰ TiO₂ films are soaked in a 30 mM cadmium nitrate/ethanol solution for 30 seconds to adsorb a layer of Cd²⁺. An ethanol rinse cycle removes weakly adsorbed ions. The film is then soaked in a solution of 30 mM Se²⁻/ethanol (SeO₂ reduced by sodium borohydride) to react with the adsorbed Cd²⁺, forming CdSe quantum dots.³⁰ The dip cycles are repeated 8 times to increase the size of the quantum dots, producing opaque brown-red films of CdSe. While the hot injection and solvothermal methods produce quantum dots with narrow size

distributions, allowing for size-effect studies, the SILAR method produces a large size distribution, which absorbs more wavelengths of light. In addition to absorbing more light, SILAR quantum dots are grown directly on the TiO_2 surface, eliminating the linker molecules and improving photoelectron transport between the materials.

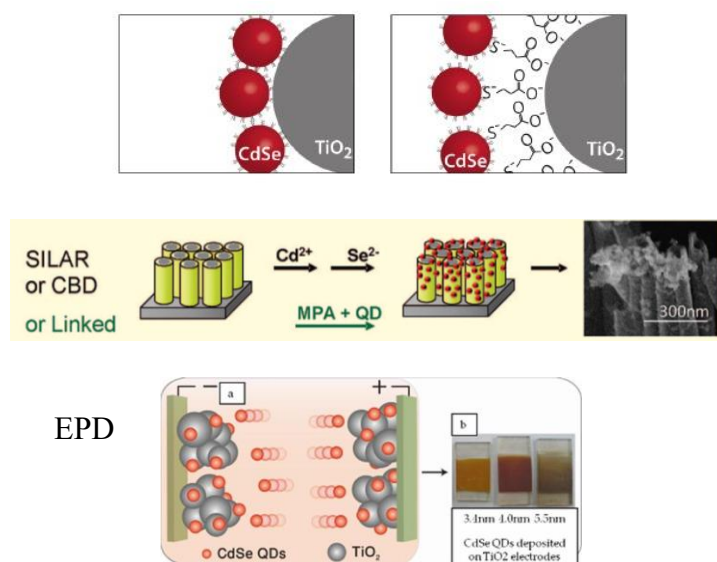


Figure 1-6. Semiconductor nanostructures can be sensitized by CdSe by several routes to adsorb them directly to TiO_2 , EPD and SILAR, or linked through thiol and carboxylic acid moieties. SILAR: successive ionic layer adsorption and reaction. CBD: chemical bath deposition. EPD: electrophoretic deposition. Reprinted with permission from^{11, 31}. Copyright 2010 American Chemical Society.

Metal oxide transport layer

TiO_2 and ZnO are used to accept electrons from light absorbers, and, therefore, nanostructuring the metal oxide increases the surface area available to load more light absorbers. Nanostructure morphology of metal oxide semiconductors is controlled through synthetic parameters to create wide-band gap photoanodes, Figure 1-7. Titanium dioxide nanoparticles (~20 nm) are synthesized hydrothermally by hydrolysis of titanium alkoxide and subsequent exposure

to a high temperature and pressure environment, $\sim 150\text{-}200\text{ }^\circ\text{C}$.⁴³ A film of nanoparticles on the order of $1\text{ }\mu\text{m}$ thick is made on a conductive glass substrate from the aqueous suspension of nanoparticles by the doctor-blade technique. The additive poly(ethylene glycol) reduces aggregation of the nanoparticles in solution. Since amorphous TiO_2 has poor electrical conduction properties, the film is sintered and annealed to the anatase crystalline phase of TiO_2 by heat treatment at $450\text{ }^\circ\text{C}$.⁴³

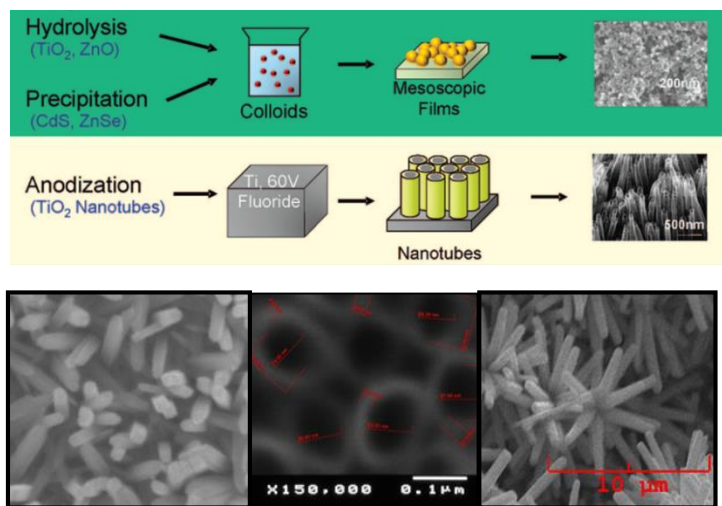


Figure 1-7. TiO_2 nanostructures, particles, rods, and tubes can be synthesized by several routes. Reprinted with permission from¹¹. Copyright 2011 Royal Society of Chemistry. SEM micrographs of TiO_2 nanorods and nanotubes and ZnO nanoflowers; author's work.

In contrast to nanoparticles, vertically aligned TiO_2 nanorods direct electron transport to the substrate, potentially collecting more photoelectrons, Figure 1-8.³² Titanium dioxide nanorods are grown directly on FTO-glass by slow hydrolysis of titanium alkoxide in an acidic hydrothermal synthesis.^{30, 31} Since the substrate, fluorine-doped tin oxide, has similar unit cell dimensions as crystalline TiO_2 in the rutile phase, rutile TiO_2 grows perpendicularly from the FTO-glass surface with a glycine catalyst.³⁰ However, the anatase crystalline phase of TiO_2 has higher electron mobility and surface area than rutile and is preferred in solar cell applications.³³ Anatase does not

match the unit cell dimensions of the substrate and has not been grown directly on FTO-glass.³⁴ Efforts are ongoing to synthesize anatase nanorods directly on FTO-glass in a similar manner.³⁴ To increase the number density of the nanorods and area for sensitizer loading, the spacing between the nanorods has been decreased by facilitating the nucleation of TiO₂ with the addition of a polymer precursor.³³

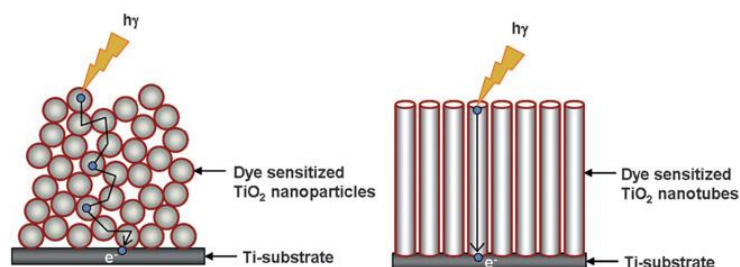


Figure 1-8. Nanostructures aligned perpendicularly to the conductive substrate allow for direct electron transport, eliminating undesired lateral electron transport. Reprinted with permission from³². Copyright 2011 Wiley.

Vertically aligned TiO₂ nanotubes have the same benefit of directed electron transport, while offering higher surface area than nanorods for increased sensitizer loading. They are synthesized by an anodization technique; titanium foil is electrochemically oxidized (~60V) to form a planar layer of TiO₂ and dissolved by fluoride ions (~0.1M) to form a nanotube layer, Figure 1-7.^{32, 35} The length of the nanotubes is primarily varied by the duration of the applied voltage (length \propto duration) while the nanotube diameter is primarily varied by adjusting the voltage (diameter \propto voltage).³⁵ Typically, the vertically aligned nanotubes are not separated but contact each other, allowing for undesired lateral electron transport and decreasing exposed surface area. However, nanotubes have been grown 100 nm apart by increasing the fluoride concentration and using viscous di(ethylene glycol) as the electrolyte solvent.³⁶ After formation, the TiO₂

nanotube layer must be transferred from the opaque titanium foil to a transparent conductive substrate or the solar cell must be illuminated through the transparent counter electrode.³¹

Zinc oxide nanoflowers also have the benefit of directed electron transport, Figure 1-7, 8. They are hydrothermally synthesized by the hydrolysis of zinc acetate in an ammonium solution to form a zinc-ammonium precursor complex.^{37, 38} They can be grown in solution or directly on FTO-glass and their sizes are typically on the order of microns, Figure 1-7. If their sizes can be reduced, they could potentially be grown directly within TiO₂ nanotubes, offering additional electron acceptor surface area to collect more photoelectrons from the sensitizer.

Redox Mediators

Historically, many different redox mediators have been investigated in DSSCs, including metal complexes based on Co, Cu, Ni, and Fe.³⁹ However, applying the same redox mediators to QDSCs has not been as successful and a smaller variety of redox mediators has even been investigated.³⁹ Since the traditional iodide/triiodide electrolyte used in DSSCs corrodes metal chalcogenide quantum dots, a sulfide/polysulfide electrolyte was found to be less corrosive.²² Although sulfide/polysulfide readily corrodes CdTe, CdSe is more stable and a sulfoselenide layer forms that protects against corrosion.²³ However, the use of sulfide/polysulfide requires novel counter electrodes, i.e., reduced graphene oxide with Cu₂S, that are stable and allow fast charge transfer and high current density.²² Alternatively, novel non-corrosive electrolytes can be synthesized that are characterized by reduced recombination, a tunable redox potential, high diffusion coefficient, and minimal light absorption.

A series of manganese pyrazolborate complexes are synthesized from pyrazole and potassium borohydride followed by cation exchange with manganese chloride.¹⁰ The Mn(II/III) redox potentials in these complexes are on the order of 200 mV further from the vacuum energy

than iodide/triiodide and sulfide/polysulfide. Therefore, the new redox mediators have produced higher open-circuit voltages, although low photocurrent currently impedes greater solar cell efficiencies. Manganese pyrazolborate complexes have redox potentials around 0.8 V vs NHE, much higher and more favorable than sulfide/polysulfide (0.35 V vs NHE).¹⁰

Solar cell fabrication

After the photoanode and redox mediator are synthesized, they must be paired with a transparent counter electrode for characterization of the complete solar cell. For the counter electrode in QDSCs, FTO-glass is sputter-coated with platinum to catalyze the reduction of the redox mediator. A hot-melt plastic film adheres the anode and cathode and provides space for the redox mediator between the electrodes, Figure 1-9. For the counter electrode in HBHJs, films of gold are evaporated directly onto the polymer layer.

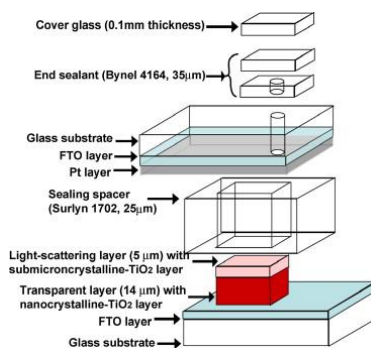


Figure 1-9. The photoanode consists of the sensitized TiO₂ layer on FTO-glass. The cathode consists of platinum-coated FTO-glass. The sealing spacer makes room for the redox electrolyte between the cathode and photoanode and the hole in the cathode allows for injection of the electrolyte. Reprinted with permission from³². Copyright 2011 Wiley.

Chapter 2. Mn^{II/III} Complexes as Promising Redox Mediators in Quantum Dot Sensitized Solar Cells

2.1 Introduction

The 1985 discovery of fast photoelectron injection and slow recombination at TiO₂-Ru dye interfaces pioneered the modern field of light harvesting from sensitized TiO₂.⁴¹ The observed long-lived charge separated state allowed Grätzel to capitalize on the efficient charge transfer by collecting the photoelectrons from TiO₂ as photocurrent with unprecedented efficiency.⁴² By using mesoporous TiO₂ films with ~2,000-fold higher surface area, O'Regan and Grätzel improved the dye adsorption yield and power conversion efficiency (7.1%) in dye-sensitized solar cells (DSSC).^{43, 44} As an alternative to molecular dye sensitizers, type II-VI semiconductor quantum dots (CdS and CdSe) exhibit fast photoelectron injection rates and have been employed in quantum dot-sensitized solar cells (QDSSC).⁴⁵⁻⁴⁹ However, QDSSCs (record efficiencies ~7%) have yet to compete with that of DSSCs (13%) and remain the subject of continued research.⁵⁰⁻⁵²

In DSSCs, the iodide/triiodide couple serves to efficiently regenerate the ground state sensitizer, acting as a redox mediator to complete the electrical circuit between sensitized TiO₂ and the counter electrode. Much work has contributed to understanding the redox chemistry involved and the criteria necessary for optimization of the redox mediator, electrolyte additives, and solvent.⁵³⁻⁵⁶ However, QDSSCs sensitized with cadmium chalcogenide quantum dots are unstable in the presence of iodide/triiodide due to photoanodic dissolution and the formation of cadmium iodide.⁵⁷ Therefore, sulfide/polysulfide electrolytes and suitable counter electrodes were developed to achieve stable QDSSCs.^{58, 59} Unfortunately, the unfavorably low redox potential, ~ 0.15 V vs. Ag/AgCl, of the sulfide/polysulfide redox mediator system currently limits the performance of record liquid-junction QDSSCs. The resultant low photovoltages, ~ 0.6 V, have generated a need

for the development of alternative redox mediators to improve photovoltages and overall efficiencies. To that end, metal complexes based on $\text{Co}^{\text{II/III}}$ centers, with tunable reduction potentials $\sim 0.3\text{-}0.5$ V vs. Ag/AgCl , have garnered much attention as alternatives to the iodide/triiodide couple in DSSCs,⁶⁰⁻⁶⁵ but to a lesser extent in QDSSCs.^{30, 66, 67}

The effectiveness of $\text{Co}^{\text{II/III}}$ mediators in DSSCs ($> 10\%$)⁶³ may be partly due to slow reduction kinetics of Co^{III} complexes, which undergo charge transfer-induced spin crossover transitions and internal reorganization upon electron transfer (d^6 to d^7).²² Ideally, the oxidized redox mediator species M^{ox} , present at the TiO_2 surface, should not significantly reduce the lifetime of TiO_2 conduction band electrons ($\text{TiO}_2(e^-)$ s) before M^{ox} diffuses to the counter electrode. The undesired recombination reaction between $\text{TiO}_2(e^-)$ s and M^{ox} limits charge collection, as with the ferrocene/ferrocenium couple, and constrains the choice of alternative mediators.⁶⁸ Some Mn^{III} complexes are known to undergo a spin change upon reduction (d^4 to d^5) that can slow the undesired recombination and have recently been employed in DSSCs.⁶⁹ Herein, the efficacy of $\text{Mn}^{\text{II/III}}$ complexes for use in QDSSCs is probed and shown to be attractive alternatives as redox mediators.

A series of Mn poly(pyrazolyl)borates, with reduction potentials more positive than $\text{Co}(\text{bpy})_3$, where $\text{bpy} = 2,2'$ -bipyridine, and sulfide/polysulfide, delivered photovoltages ~ 1 V when coupled with CdS/CdSe co-sensitized TiO_2 photoanodes. Photocurrents and incident-photon-to-current efficiency (IPCE) spectra similar to cells employing $\text{Co}(\text{bpy})_3$ established the ability of the Mn^{II} complexes to regenerate ground state CdS and CdSe. Favorably, the Mn poly(pyrazolyl)borates display slower recombination at the TiO_2 photoanodes compared to $\text{Co}(\text{bpy})_3$, resulting in higher quasi-Fermi levels and, in turn, higher photovoltages. Thus, $\text{Mn}^{\text{II/III}}$ complexes are promising alternative redox mediators as they deliver efficiencies on average up to 50% higher than $\text{Co}(\text{bpy})_3$.

However, the low solubility of these complexes exacerbates mass transport limitations on redox mediators with slow diffusion properties and leads to limited photocurrents. Therefore, Mn poly(pyrazolyl)borates with higher solubility are the subject of continued research.

2.2 Experimental Methods

Chemicals and Materials. Fluorine-doped tin oxide-coated glass (FTO-glass, 12-14 Ω cm⁻²) from Hartford Glass Co., titanium (IV) chloride from Sigma Aldrich, and Solaronix T/SP TiO₂ paste were used for photoanode preparation. Cadmium nitrate tetrahydrate (98%), cobalt chloride (98%), lithium perchlorate (99.99%), manganese chloride (97%), selenium dioxide (99.9%), sodium borohydride (98%), sodium sulfide (97%), and zinc acetate (99.99%) from Sigma Aldrich were used without further purification. 2,2'-Bipyridine (99%) was obtained from Acros Organics, nitrosium hexafluoroantimonate (97%) from Strem Chemicals, and sodium hexafluorophosphate (98%) from Oakwood Products. Ethanol from Decon Laboratories, methanol and acetone from Spectrum Chemical, and γ -butyrolactone from Sigma Aldrich were used as solvents without further purification.

Synthesis of Mn^{II/III} Complexes. Mn^{II}(pzTp)₂, Mn^{II}(Tp)₂, Mn^{II}(Tp*)₂, where pzTp = tetrakis(pyrazolyl)borate, Tp = hydrotris(pyrazolyl)borate and Tp* = hydrotris(3,5-dimethylpyrazolyl)borate, and the oxidized salts Mn^{III}(pzTp)₂SbF₆, Mn^{III}(Tp)₂SbF₆ and Mn^{III}(Tp*)₂SbF₆ were synthesized as previously described.¹⁰ MnCl₂ was added to an aqueous solution of the respective poly(pyrazolyl)borate potassium salt (2 mol equiv., Strem Chemicals, 98%) and the Mn-poly(pyrazolyl)borate immediately precipitated. The Mn^{II} complexes were filtered, washed with copious amounts of water, and vacuum dried. Oxidation of the complexes to Mn^{III} salts was achieved by addition of NOSbF₆ to the Mn^{II} complexes (1 mol equiv.) in 1:1

acetonitrile/dichloroethane solutions and subsequent rotary evaporation and recrystallization from hot acetonitrile.

Synthesis of Co^{II/III} Complexes. Co^{II}(bpy)₃(PF₆)₂ was synthesized as previously, where bpy = 2,2'-bipyridine.⁷⁰ A methanolic solution of 2,2'-bipyridine (3.5 mmol) was added dropwise to an aqueous solution of CoCl₂ (2 mmol). With continued stirring, aqueous NaPF₆ (6.7 mmol) was added to precipitate the product. The precipitate was then filtered, dried, recrystallized from hot ethyl acetate, and dried under vacuum to obtain Co^{II}(bpy)₃(PF₆)₂.

Co^{III}(bpy)₃(PF₆)₃ was synthesized by chemically oxidizing Co^{II}(bpy)₃²⁺ before adding NaPF₆. A solution of 2,2'-bipyridine and CoCl₂ was prepared as above. Concentrated HCl and 30% H₂O₂ were added simultaneously to the stirring mixture (2 mL each).⁶³ The solution was heated at 50 °C for 45 min, during which time a burnt orange color developed. Aqueous NaPF₆ (6.7 mmol) was added to precipitate the product. The precipitate was then filtered, dried, recrystallized from hot ethyl acetate, and dried under vacuum to obtain Co^{III}(bpy)₃(PF₆)₃.

Device Fabrication

Photoanode Preparation. FTO-glass was ultrasonicated for 15 minutes in aqueous Alconox™ detergent and rinsed with deionized water. The sonication/rinsing cycle was repeated with ethanol and acetone, respectively. A compact TiO₂ layer was deposited by heating FTO-glass in 40 mM TiCl_{4(aq)} for 30 min before doctor-blading Solaronix T/SP paste (100% anatase, 15-20 nm). The TiO₂ films were heated at 80 °C for 30 min before a 7 °/min ramp to 450 °C and held at 450 °C for 30 min.

Successive Ionic Layer Adsorption and Reaction. (SILAR) A SILAR method was used to sequentially deposit CdS, CdSe, and ZnS onto the mesoporous TiO₂ films.³⁰ Each SILAR cycle consists of soaking the annealed TiO₂ films in cationic solutions (Cd²⁺ or Zn²⁺) for 1 min, rinsing

with the respective neat solvent, soaking in anionic solutions (S^{2-} or Se^{2-}) for 1 min, and rinsing again with neat solvent. Thus, all TiO_2 photoanodes are coated first, with CdS quantum dots, second, with a layer of CdSe, and lastly, with a passivation layer of ZnS, as verified by absorption spectroscopy.^{71, 72} For CdS SILAR deposition, 0.1 M $Cd(NO_3)_2$ and 0.1 M Na_2S solutions were used (1:1 methanol/water, 6 cycles). For CdSe SILAR deposition, 0.03 M cadmium nitrate and 0.03 M selenium dioxide solutions were used (ethanol, 8 cycles). Solutions of Se^{2-} were prepared from selenium dioxide by adding two equivalents of $NaBH_4$ and stirring under nitrogen atmosphere until clear. For ZnS SILAR deposition, 0.1 M $Zn(CH_3COOH)_2$ and 0.1 M Na_2S solutions were used (1:1 methanol/water, 2 cycles).

Electrochemistry. Cyclic voltammetry and potential-step chronoamperometry of Mn^{II} complexes were performed in γ -butyrolactone with 0.1 M $LiClO_4$ supporting electrolyte with a Pt mesh counter electrode, a Pt or glassy carbon working electrode, and an Ag/AgCl saturated KCl reference electrode, calibrated with $K_4[Fe(CN)_6]$ from Fisher Scientific. Potentials were applied with a BASi Epsilon potentiostat (0.01-10 V/s). For potential-step chronoamperometry, potentials were applied sufficiently reductive so that the current measured was diffusion limited.

Photovoltaic Characterization. The Mn-complexes were tested and compared to $Co(bpy)_3$ as redox mediators in conjunction with the photoanodes fabricated above. A three-electrode arrangement was employed with the quantum dot-sensitized photoanode as the working electrode, a Pt mesh counter electrode, and an Ag/AgCl reference electrode. The electrolyte (0.35 mL) consisted of 0.1 M $LiClO_4$, 50 mM M^{II} , and 5 mM M^{III} in γ -butyrolactone, where M^{II} and M^{III} represent the reduced and oxidized form of the respective redox mediator complex. Among common liquid-junction solar cell solvents, the Mn-complexes were most soluble in γ -butyrolactone.⁷³ A masked area of 0.1256 cm^2 was illuminated at various intensities with a

Newport LCS-100 solar simulator (AM 1.5G spectrum) and current-voltage responses were recorded at a scan rate of 25 mV/s. Incident-photon-to-current efficiency (IPCE) spectra were collected at short-circuit conditions using a monochromatized light source from Optical Building Blocks (OBB). Open circuit voltage decay measurements were collected by interrupting the illumination and monitoring the voltage decay at 50 ms data intervals.⁷⁴

2.3 Results and Discussion

The operation of sensitized solar cells depends on directional and regenerative photoelectrochemical charge transfer upon illumination in order to convert incident photons to photocurrent. Therefore, in QDSSCs efficient generation of photocurrent is mediated by 1) fast electron injection from photoexcited QDs to TiO₂, 2) fast reduction of the oxidized QDs by reduced redox mediator species, and 3) slow charge recombination between TiO₂(e⁻)s and the M^{ox} species (Equation 1), Figure 2-1. Within the TiO₂(e⁻) lifetime, τ_e , photoelectrons must be transported through the mesoporous film and collected at the FTO-glass substrate.

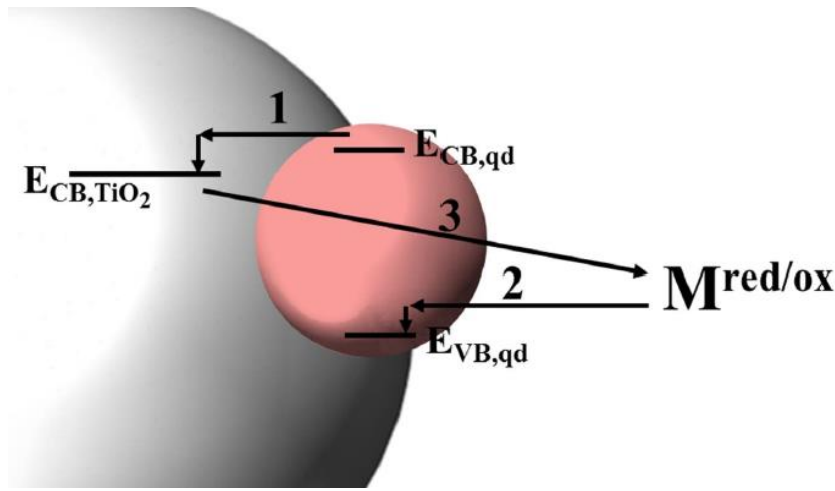
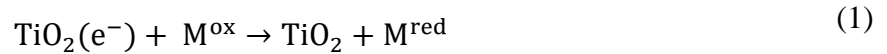


Figure 2-1. Energy schematic of electron transfer at the quantum dot-TiO₂ interface: 1) photoelectron injection from the quantum dot conduction band ($E_{CB,qd}$) into the TiO₂ conduction band (E_{CB,TiO_2}), 2) reduction of the quantum dot into the valence band ($E_{VB,qd}$) by reduced mediator species, 3) undesired recombination of TiO₂(e⁻)s with oxidized mediator species.

Thus, a series of Mn-complexes, Mn^{II}(pzTp)₂, Mn^{II}(Tp)₂, and Mn^{II}(Tp*)₂, with slow reduction kinetics were chosen to avoid shortening τ_c by the charge transfer from TiO₂(e⁻)s to Mn^{III}. The one-electron reduction of Mn^{III}poly(pyrazolyl)borates results in a low spin to high spin transition ($t_{2g}^4 \rightarrow t_{2g}^3 e_g^2$; $S = 1 \rightarrow 5/2$).³¹ Due to this charge transfer-induced spin crossover, the standard electrochemical rate constants are slow (Fc^{0/+}: 10⁰ cm/s > Co^{II/III}: 10⁻¹ cm/s > Mn^{II/III}: 10⁻⁴ cm/s) and decrease in the ligand series Tp* > pzTp > Tp.^{10, 75, 76} At the TiO₂ anode surface, an additional thermodynamic barrier is imposed by the spin transition and reorganization energy associated with the transition, which should slow recombination (process 3 in 2- 1).

Additionally, maximization of the photocurrent generated from illumination of QDs requires minimization of competitive light absorption by other solar cell components, including the redox mediator. Therefore, the ideal species should absorb minimally in the absorption range of CdS/CdSe quantum dots (700-400 nm). Compared to sulfide redox mediator, manganese poly(pyrazolyl)borates display less absorption in the desired range, Figure 2-2. Mn^{II} species have no appreciable absorbance above ~ 420 nm (< 3 M⁻¹cm⁻¹), Figure S2-3. The absorbance of Mn^{III} species extends further into the visible region, with absorbance at ~ 440 nm (~ 184 M⁻¹cm⁻¹), although with a lower extinction coefficient than Na₂S/S at similar wavelengths (~ 277 M⁻¹cm⁻¹).

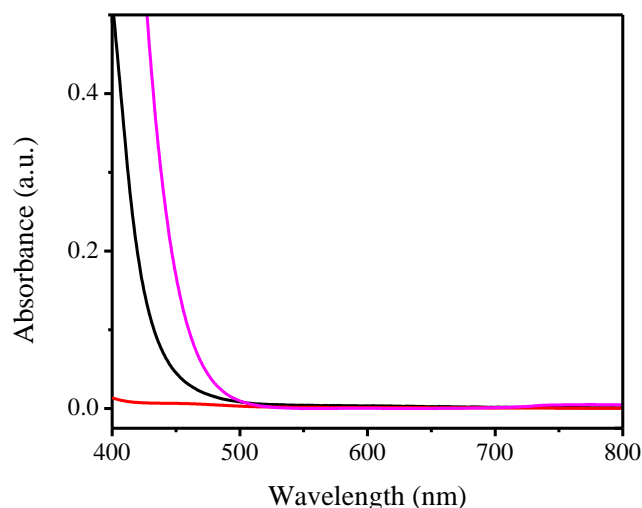


Figure 2-2. Visible absorbance spectra of redox mediators used in QDSSCs. Black: 1 mM of Mn(Tp)_2 , 0.1 mM $\text{Mn(Tp)}_2\text{SbF}_6$; Red: 1 mM $\text{Co(bpy)}_3(\text{PF}_6)_2$, 0.1 mM $\text{Co(bpy)}_3(\text{PF}_6)_3$; and Magenta: 1 mM Na_2S , 1 mM S. A baseline of the respective solvents was subtracted.

To determine the viability of Mn-complexes as redox mediators in QDSSCs, the light-harvesting performance of the photoanode/electrolyte combination was analyzed by fabricating and testing three-electrode cells. In three electrode arrangements, as opposed to complete solar cells, the performance of the photoanode/electrolyte combination is isolated from counter electrode effects (mass transport and charge transfer overpotentials). Therefore, the charge-transfer kinetics and energetics at the photoanode can be studied and optimized independently of the counter electrode kinetics. However, the spin-crossover barrier that slows recombination must be overcome by the counter electrode. As the subject of continued research, counter electrodes will be designed to sufficiently catalyze the reduction of Mn^{III} species, minimizing charge-transfer overpotentials that would reduce power conversion efficiencies. CdS/CdSe-sensitized TiO_2 served as the photoanode in contact with the respective electrolyte. Cells containing Mn-complexes were compared to

Co(bpy)₃. Sulfide/polysulfide was not compared due to its lack of chemical stability in γ -butyrolactone.

Current density-voltage (J-V) plots with QD-sensitized TiO₂ photoanodes and electrolytes with the Mn-complexes are shown with different illumination intensities in Figure 2-3. Figures of merit for 20% and 100% sun intensity are tabulated in Table 2-1 and Table 2-S1, respectively; data from individual trials are tabulated in Table 2-S2. Overall efficiency averages, η , trend as Mn(Tp*)₂ ~ Co(bpy)₃ < Mn(pzTp)₂ < Mn(Tp)₂. For Mn(Tp)₂, increases in photovoltage and fill factor lead to efficiencies competitive with the known redox mediator, Co(bpy)₃, and the best performing cells were twice as efficient. Comparison of J-V curves for Mn-complexes and Co(bpy)₃ are shown in Figure S2-5. Further insight into solar cell performance is gained by analyzing the trends in photovoltages, fill factor, and photocurrent, which compose overall efficiencies.

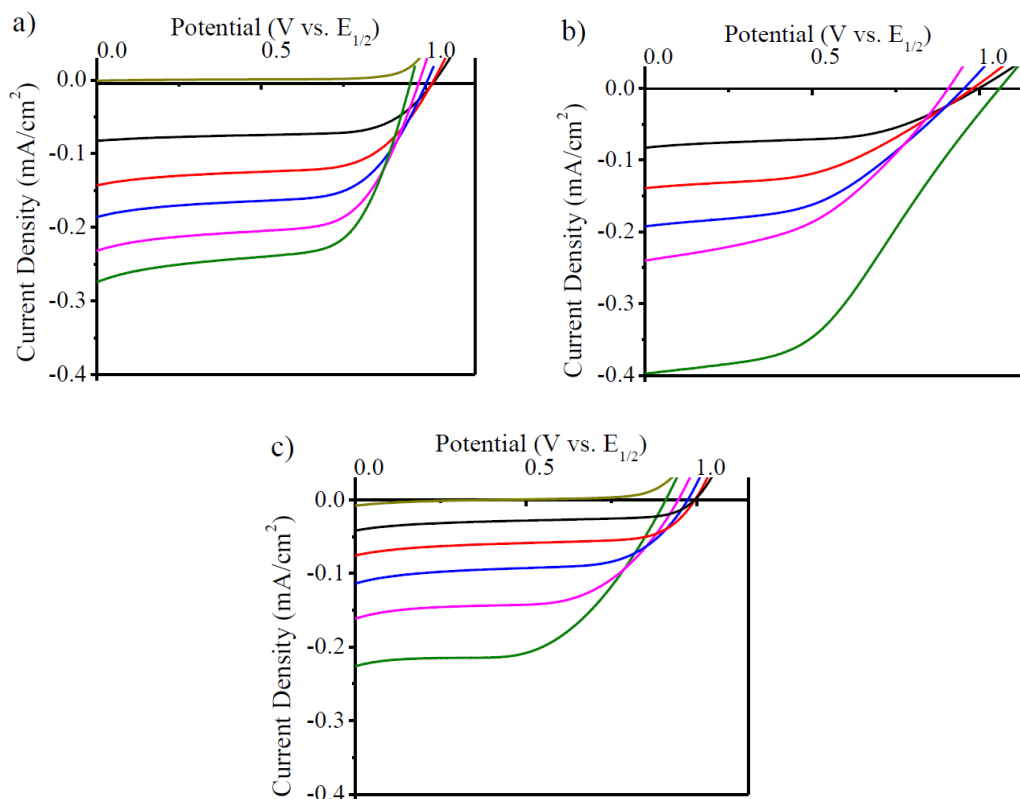


Figure 2-3. J-V plots of three-electrode arrangement with (a) 50 mM Mn(pzTp)₂ and 5 mM Mn(pzTp)₂SbF₆, (b) 50 mM Mn(Tp)₂ and 5 mM Mn(Tp)₂SbF₆, and (c) 50 mM Mn(Tp*)₂ and 5 mM Mn(Tp*)₂SbF₆. All electrolytes contain 0.1 M LiClO₄ in γ -butyrolactone. Potentials scanned from reverse to forward bias at 25 mV/s. dark yellow: dark current; black: 20% sun; red: 40% sun; blue: 60% sun; magenta: 80% sun; green: 100% sun (100 mW/cm²).

Table 2-1. Figures of Merit for Cells Containing Mn or Co Complexes at 20% Sun Intensity

| | J _{sc} (mA/cm ²) | V _{oc} (V) | Fill Factor | η (%) | E _{1/2} (V vs. Ag/AgCl) |
|-----------------------|---------------------------------------|---------------------|-------------|------------|----------------------------------|
| Mn(pzTp) ₂ | -0.08±0.02 | 1.08±0.06 | 0.66±0.2 | 0.24±0.04 | 0.52 |
| Mn(Tp) ₂ | -0.12±0.02 | 0.9±0.1 | 0.55±0.1 | 0.33±0.15 | 0.51 |
| Mn(Tp*) ₂ | -0.06±0.02 | 1.01±0.02 | 0.58±0.08 | 0.19±0.09 | 0.51 |
| Co(bpy) ₃ | -0.12±0.02 | 0.8±0.1 | 0.45±0.09 | 0.22±0.04 | 0.36 ⁷⁰ |

To maximize the photovoltage, ideal redox mediators should have sufficiently positive reduction potentials (> 0.1 vs. Ag/AgCl). In QDSSCs, the theoretical upper limit photovoltage is determined by the potential difference between the electron Fermi level in TiO₂ under illumination ($E_{F,n}$) and the redox potential of the redox mediator.^{77, 78} Photovoltages approaching the upper limit can be obtained by employing redox mediators with reduction potentials > 0.15 V vs. Ag/AgCl, while still maintaining sufficient reductive power to reduce QDs, process 2 in Figure 2-1. Cyclic voltammetry shows $E_{1/2}$ values of ~ 0.51 V vs. Ag/AgCl for the series of Mn poly(pyrazolyl)borates studied, Figure 2-4, which is 0.4 V more positive than Na₂S/S and 0.1-0.2 V more positive than typical Co^{II/III} complexes.⁶² With such positive reduction potentials, the Mn-complexes still demonstrated sufficient driving force to reduce photooxidized QDs and act as viable alternative redox mediators. The high V_{oc} values ~ 1 V (x-axis intercept) are consistent with the positive reduction potentials discussed above, as the photovoltages increase with reduction potential, $\text{Co}(\text{bpy})_3 < \text{Mn}(\text{Tp})_2 \sim \text{Mn}(\text{Tp}^*)_2 < \text{Mn}(\text{pzTp})_2$.

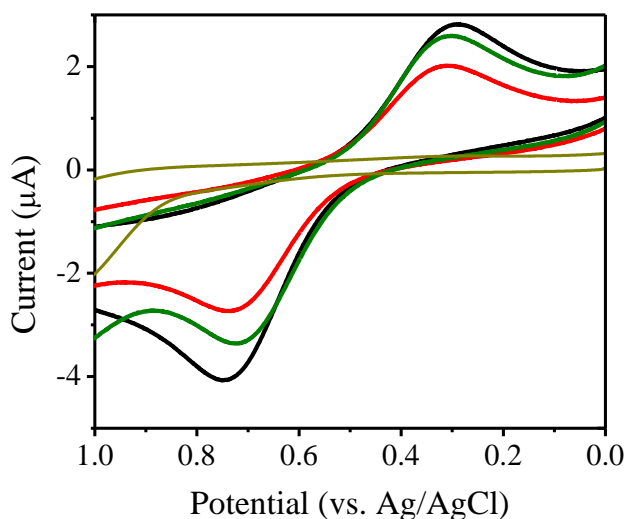


Figure 2-4. Cyclic voltammograms of $\text{Mn}(\text{pzTp})_2$ (black), $\text{Mn}(\text{Tp})_2$ (red), $\text{Mn}(\text{Tp}^*)_2$ (green), and supporting electrolyte only (dark yellow): γ -butyrolactone with 0.1 M LiClO_4 with a Pt working electrode. $E_{1/2}$ values are tabulated in Table 2-1.

Both fill factor and photovoltage are influenced by recombination kinetics. Long electron lifetimes of $\text{TiO}_2(e^-)$ s, τ_e , increase the concentration of $\text{TiO}_2(e^-)$ s and, thus, $E_{F,n}$. Therefore, long τ_e , i.e., slower recombination, contributes to a higher $E_{F,n}$ and V_{oc} . High fill factor depends on recombination kinetics by the ability to sustain photocurrent under applied bias. At applied potentials near V_{oc} , the reduction of Mn^{III} species by $\text{TiO}_2(e^-)$ s is slow, Equation 1, maintaining long τ_e . τ_e is measured by monitoring the open circuit voltage decay (OCVD) from illumination conditions to equilibrium dark conditions.^{74, 78} The time derivative of the voltage decay, scaled by the thermal voltage, is used to extract τ_e .⁷⁹

$$\tau_e = -\frac{k_B T}{e} \left(\frac{dV_{oc}}{dt} \right)^{-1} \quad (2)$$

From plots of τ_e vs. V_{oc} , recombination kinetics can be qualitatively compared between cells of different redox mediators, Figure 2-5. Lifetimes at a given voltage increase in the order $Mn(Tp^*)_2 < Mn(Tp)_2 < Mn(pzTp)_2$. Consistent with the longest lifetimes, cells employing $Mn(pzTp)_2$ demonstrate the highest fill factors and photovoltages. By extrapolating $Co(bpy)_3$ data to higher voltages, the Mn-complexes demonstrate lifetimes 2-4 orders of magnitude longer than $Co(bpy)_3$ at the same V_{oc} . For $Mn^{II/III}$, the slower undesired recombination reaction is likely due to the effective charge transfer-induced spin crossover, further supporting the viability of Mn poly(pyrazolyl)borates as alternative redox mediators. Although both $Co(bpy)_3$ and the Mn-complexes undergo charge transfer-induced spin crossover upon reduction (d^6 to d^7 for Co and d^4 to d^5 for Mn), the barrier towards reduction is larger for the Mn-complexes. Structural and electronic differences between the Co- and Mn-complexes will affect the reduction barrier through reorganization energies, electron pairing energies, and ligand field splitting.

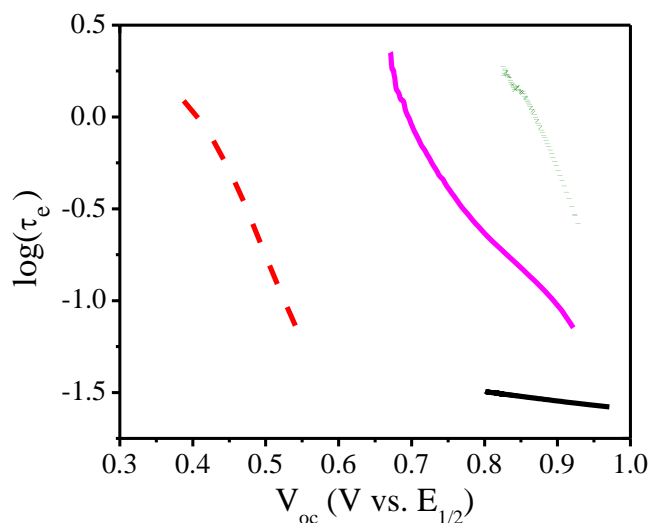


Figure 2-5. Electron lifetimes extracted from open circuit voltage decay measurements (OCVD) by Equation S2. Mn(Tp)₂ (solid magenta), Mn(pzTp)₂ (dotted green), Mn(Tp*)₂ (solid black), and Co(bpy)₃ (dashed red).

The low solubility of the Mn-complexes studied (50 mM in γ -butyrolactone) drastically limits the photocurrent, which is typically 1-3 mA/cm² in 0.1-0.3 M Co-based QDSSCs and 10-20 mA/cm² in 1-2 M sulfide-based QDSSCs.^{58, 66, 71, 80} This is not surprising given that even at typical concentrations used in DSSCs (0.1-0.3 M) Co polypyridyl complexes experience mass transport limitations not seen with the smaller iodide/triiodide or sulfide/polysulfide redox couples.^{81, 82} The effect of mass transport observed for the Mn-complexes at low concentrations is further complicated by an additional diffusive kinetic barrier, corresponding to interstitial Mn^{III} within the sensitized TiO₂. For direct comparison, tests with Co(bpy)₃ redox mediator were intentionally kept at the same concentration as the Mn-complexes.

Low photocurrent compared to optimized QDSSCs (1-3 mA/cm²), obtained with all redox mediators tested, does not diminish the promising effectiveness of Mn^{II/III} complexes. Rather, the primary contributions to the observed diffusion-limited photocurrents are likely the unoptimized porosity of the QD-sensitized TiO₂ films and the relatively long distance between the TiO₂ film and counter electrode in the experimental setup (8 mm). High photocurrents form concentration gradients of M^{red} and M^{ox} between the TiO₂ film and counter electrode that require initial concentrations of M^{red} >>50 mM. From Fick's first law of diffusion, the concentration gradient can be related to photocurrent (dependent on one electron transfer with redox species), assuming a linear concentration gradient, Equation 3,

$$D_o \frac{dC_o}{dx} = \frac{j}{F} \quad (3)$$

where D_o , the diffusion coefficient of redox mediator species, is assumed to be constant throughout the TiO_2 film and bulk solution for simplicity, F is Faraday's constant, and j is the photocurrent density. Diffusion coefficients of Mn-complexes in γ -butyrolactone were determined by potential-step Cottrell analysis shown in the Supporting Information, Figure S2-4. For QDSSC three electrode cells with $\text{Mn}^{\text{II}}(\text{Tp})_2$ ($D_o = 2 \times 10^{-5} \text{ cm}^2/\text{s}$) producing $j = 0.12 \text{ mA}/\text{cm}^2$, a concentration gradient of $60 \text{ mM}/\text{cm}^2$ forms between the electrodes ($dC_o \sim 50 \text{ mM}$). Therefore, considering an initial concentration of 50 mM , $\text{Mn}^{\text{II}}(\text{Tp})_2$ is depleted at the photoanode under 20% sun illumination ($20 \text{ mW}/\text{cm}^2$). The photocurrent is limited by diffusion rather than the ability of $\text{Mn}^{\text{II}}(\text{Tp})_2$ to reduce oxidized CdS/CdSe quantum dots. Similarly, smaller values of D_o for $\text{Mn}(\text{Tp}^*)_2$ and $\text{Mn}(\text{pzTp})_2$ ($1 \times 10^{-5} \text{ cm}^2/\text{s}$ and $0.6 \times 10^{-5} \text{ cm}^2/\text{s}$, respectively) supported lower photocurrents before being depleted at the photoanode.

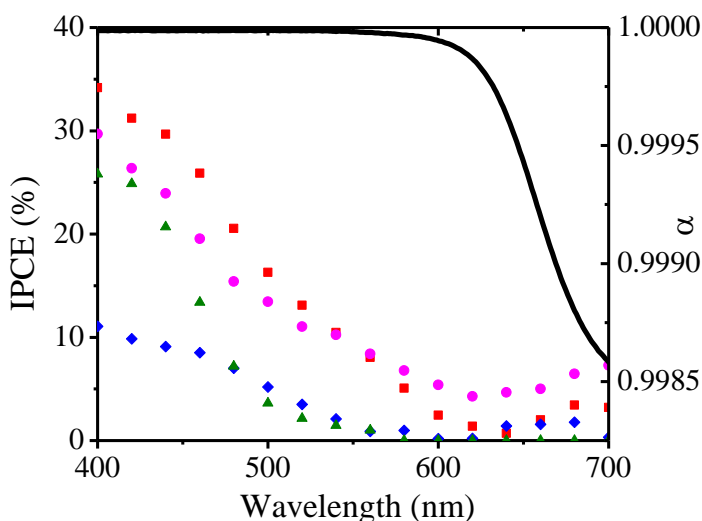


Figure 2-6. Left y-axis: Incident-photon-to-current efficiency (IPCE) spectra of three-electrode arrangement with $\text{Mn}(\text{pzTp})_2$ (green triangles), $\text{Mn}(\text{Tp})_2$ (magenta circles), $\text{Mn}(\text{Tp}^*)_2$ (blue diamonds), or $\text{Co}(\text{bpy})_3$ (red squares) redox mediator ($\sim 1 \text{ mW}/\text{cm}^2$ illumination). Right y-axis:

Light harvesting efficiency (α) of quantum dot-sensitized TiO₂ based on absorbance spectrum of sensitized films.

Incident-photon-to-current efficiency (IPCE) spectra provide a greater understanding of the observed low photocurrents, Figure 2-6. The IPCE is the product of the light harvesting (α), charge injection (η_{in}) and charge collection (η_{cc}) efficiencies according to, Equation 4.

$$\text{IPCE} = \alpha \cdot \eta_{in} \cdot \eta_{cc} \quad (4)$$

Opaque black photoanodes of CdS/CdSe-TiO₂ absorb in the visible region, minimizing the effect of α , Figure 2-6. If α is the limiting factor, then $\text{IPCE} \cong \alpha$ and the IPCE and absorbance spectra should coincide, which is not observed. Therefore, the reduced IPCE is likely due to inefficient charge injection or charge collection, which explains the difference in profile between IPCE and α . It is reasonable to assume that charge collection is the limiting factor since it depends on the reduction of oxidized CdS/CdSe quantum dots by M^{red} species, which would be depleted at the quantum dot surface as described above (diffusion limited photocurrents).

Additionally, the trend in photocurrents among the Mn-complex ligand series is consistent with the trend in standard electrochemical rate constants, mentioned above. The electrochemical rate constant for M^{ox} to M^{red} charge transfer affects the undesired recombination reaction kinetics, Equation 1. As the electrochemical rate constants of the redox mediators decrease, the initial J_{sc} values increase due to slower recombination processes, $T_p^* < pzT_p < T_p$. At steady state conditions, however, the concentration gradient of the M^{red} species imposes mass transport limits to the observed photocurrents.

2.4 Conclusions

In order to improve the efficiency of QDSSCs, new redox mediators need to be developed which display positive reduction potentials and slow charge recombination rates. Therefore, Mn poly(pyrazolyl)borate have been demonstrated as viable alternatives. The charge transfer-induced spin crossover transition, upon regenerative oxidation by photo-excited quantum dots, reduces the undesired recombination reaction at the TiO₂ surface. Slow recombination kinetics near operating voltages led to higher fill factors and contributed to higher $E_{F,n}$. Thus, coupled to positive reduction potentials, impressive photovoltages ~ 1 V result. To realize photocurrent densities in the mA/cm² range, limitations imposed by mass transport can be alleviated by designing Mn poly(pyrazolyl)borates with higher solubilities in typical QDSSC electrolyte solvents. This is the subject of continued research.

2.5 Supporting Information

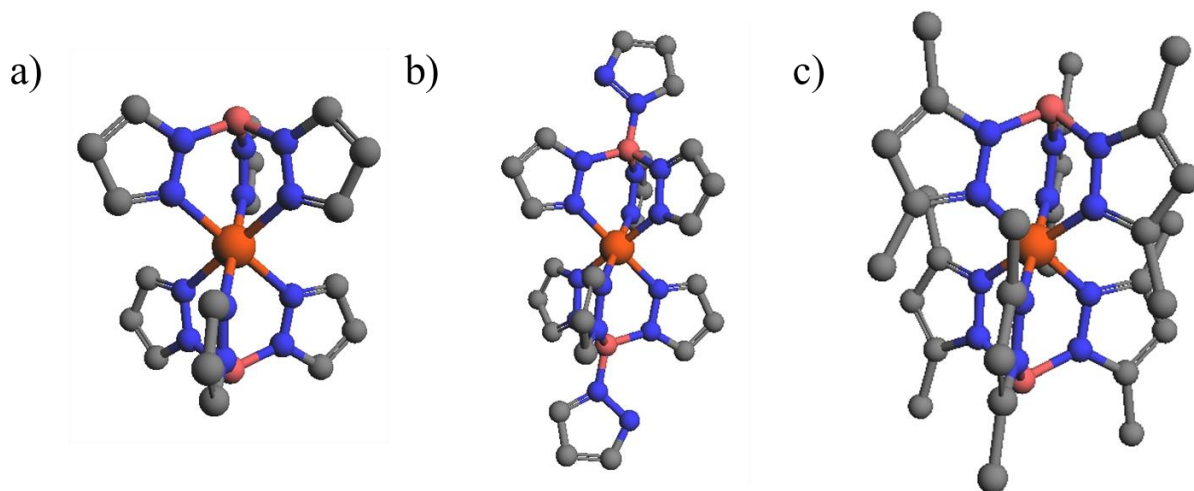


Figure S2-1. (a) $\text{Mn}(\text{Tp})_2$ (b) $\text{Mn}(\text{pzTp})_2$ (c) $\text{Mn}(\text{Tp}^*)_2$ orange: Mn; blue: N; gray: C; and pink: B. Hydrogen atoms omitted for clarity.

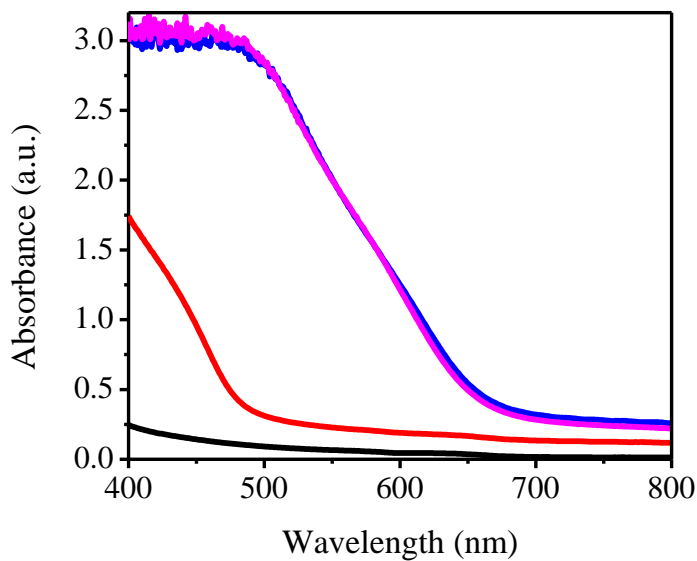


Figure S2-2. Absorbance spectra of photoanodes throughout fabrication process. Black: film of TiO_2 ; Red: film of TiO_2/CdS ; Blue: film of $\text{TiO}_2/\text{CdS}/\text{CdSe}$; Magenta: film of $\text{TiO}_2/\text{CdS}/\text{CdSe}/\text{ZnS}$. Only complete photoanodes $\text{TiO}_2/\text{CdS}/\text{CdSe}/\text{ZnS}$ were used in solar cell performance tests.

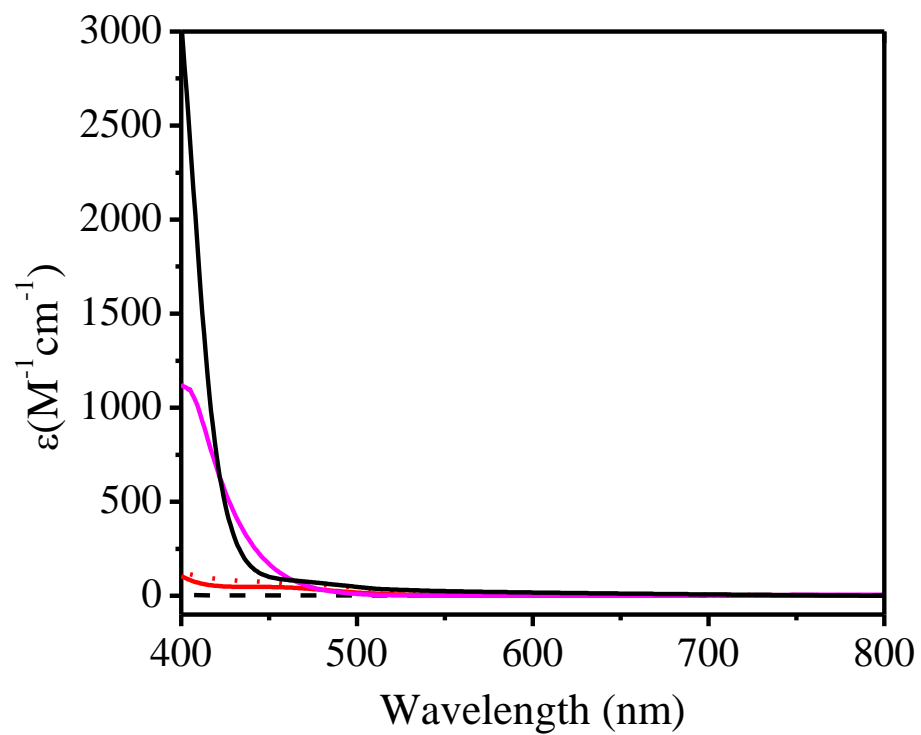


Figure S2-3. Absorbance spectra of redox mediators used in QDSSCs. Dashed Black: $\text{Mn}(\text{Tp})_2$; Solid Black: $\text{Mn}(\text{Tp})_2\text{SbF}_6$; Dashed Red: $\text{Co}(\text{bpy})_3(\text{PF}_6)_2$, Solid Red: $\text{Co}(\text{bpy})_3(\text{PF}_6)_3$; and Magenta: $\text{Na}_2\text{S/S}$.

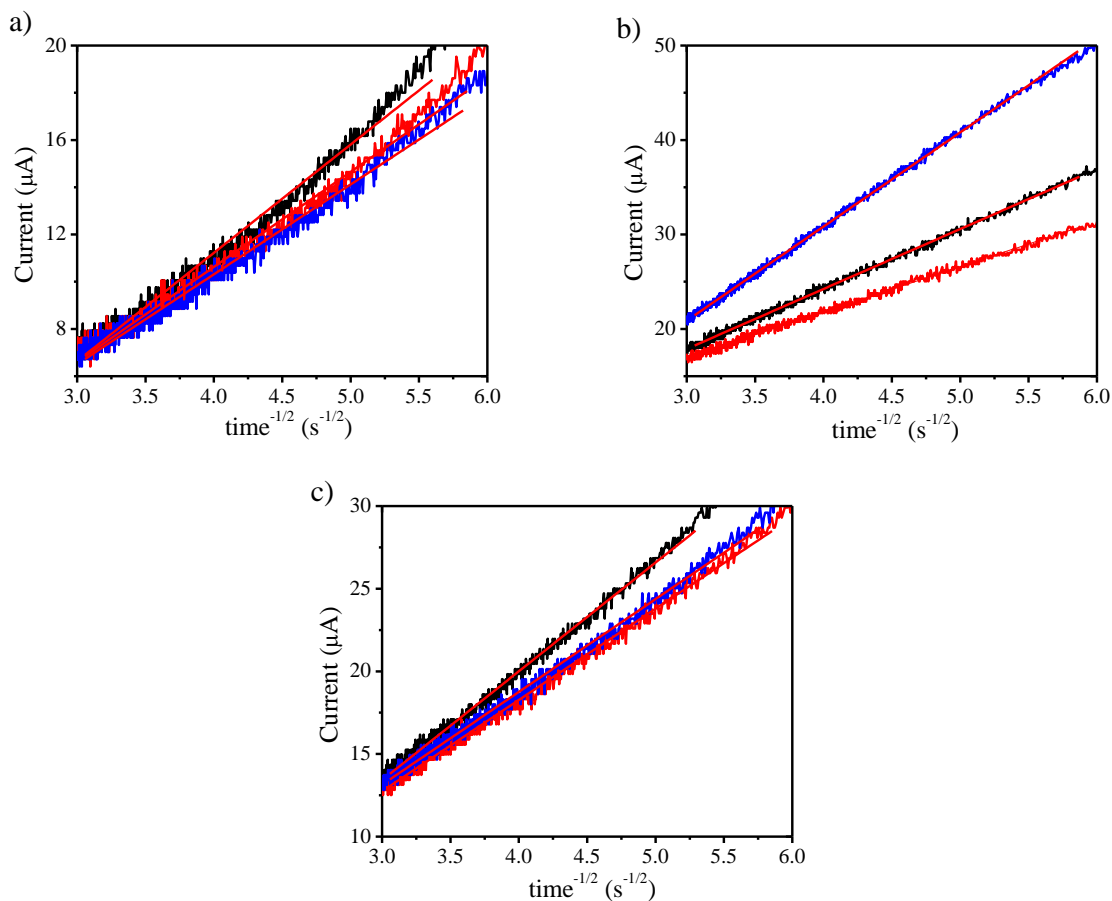


Figure S2-4. Plots of diffusion limited current vs. the inverse square root of the time from potential step experiments. (a) $\text{Mn}(\text{pzTp})_2$, (b) $\text{Mn}(\text{Tp})_2$, and (c) $\text{Mn}(\text{Tp}^*)_2$ in γ -butyrolactone with 0.1 M LiClO_4 , with a glassy carbon working, Ag/AgCl reference, and Pt mesh counter electrode. Using the Cottrell equation, diffusion coefficients are extracted from the slopes,

$$i = \frac{nFAC^*\sqrt{D_o}}{\sqrt{\pi t}} \quad (\text{S1})$$

| $D_{\text{Mn}(\text{pzTp})_2} (\text{cm}^2/\text{s})$ | $D_{\text{Mn}(\text{Tp})_2} (\text{cm}^2/\text{s})$ | $D_{\text{Mn}(\text{Tp}^*)_2} (\text{cm}^2/\text{s})$ |
|---|---|---|
| $0.6 \pm 0.1 \times 10^{-5}$ | $2 \pm 1 \times 10^{-5}$ | $1.2 \pm 0.2 \times 10^{-5}$ |

Table S2-1. Figures of Merit for Cells Containing Mn or Co Complexes at 100% Sun Intensity

| 100% sun | Jsc (mA/cm ²) | Voc (V) | Fill Factor | η (%) | E _{1/2} (V vs. Ag/AgCl) |
|-----------------------|---------------------------|-----------|-------------|-----------|----------------------------------|
| Mn(pzTp) ₂ | -0.26±0.03 | 0.99±0.07 | 0.53±0.09 | 0.14±0.03 | 0.52 |
| Mn(Tp) ₂ | -0.32±0.05 | 0.82±0.01 | 0.48±0.06 | 0.13±0.05 | 0.51 |
| Mn(Tp*) ₂ | -0.15±0.1 | 0.83±0.15 | 0.48±0.2 | 0.07±0.06 | 0.51 |
| Co(bpy) ₃ | -0.21 | 0.82 | 0.48 | 0.1 | 0.36 ⁷⁰ |

Table S2-2. Figures of Merit for Individual Cells Containing Mn Complexes at 20% Sun

Intensity

| 20% sun | Jsc (mA/cm ²) | Voc (V) | Fill Factor | η (%) |
|---------------------|---------------------------|---------|-------------|-------|
| Mn(Tp) ₂ | -0.14 | 0.99 | 0.63 | 0.44 |
| Mn(Tp) ₂ | -0.13 | 1.00 | 0.61 | 0.40 |
| Mn(Tp) ₂ | -0.10 | 0.76 | 0.42 | 0.16 |

| 20% sun | Jsc (mA/cm ²) | Voc (V) | Fill Factor | η (%) |
|----------------------|---------------------------|---------|-------------|-------|
| Mn(Tp*) ₂ | -0.06 | 1.02 | 0.58 | 0.17 |
| Mn(Tp*) ₂ | -0.04 | 1.00 | 0.50 | 0.10 |
| Mn(Tp*) ₂ | -0.08 | 1.03 | 0.67 | 0.28 |

| 20% sun | Jsc (mA/cm ²) | Voc (V) | Fill Factor | η (%) |
|-----------------------|---------------------------|---------|-------------|-------|
| Mn(pzTp) ₂ | -0.08 | 1.07 | 0.46 | 0.20 |
| Mn(pzTp) ₂ | -0.05 | 1.16 | 0.85 | 0.25 |
| Mn(pzTp) ₂ | -0.08 | 1.03 | 0.67 | 0.28 |

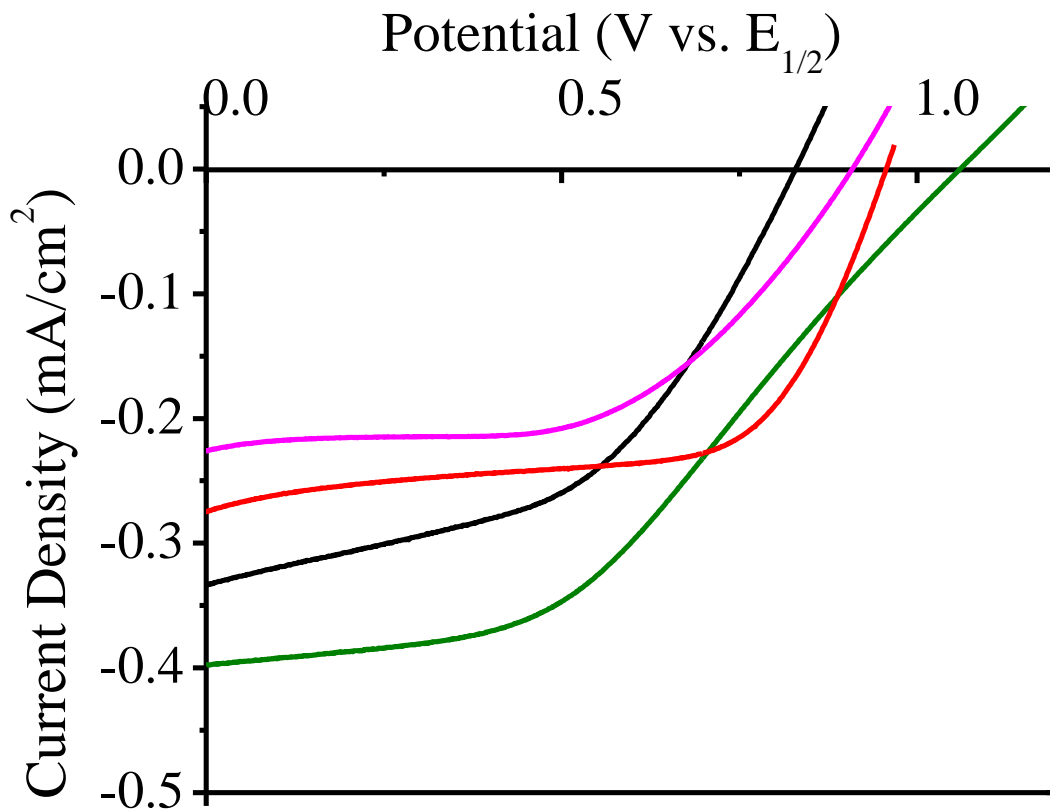


Figure S2-5. J-V plots of three-electrode arrangement with Black: 50 mM Co^{II}(bpy)₃ and 5 mM Co^{III}(bpy)₃; Red: 50 mM Mn(pzTp)₂ and 5 mM Mn(pzTp)₂SbF₆; Green: 50 mM Mn(Tp)₂ and 5 mM Mn(Tp)₂SbF₆; and Magenta: 50 mM Mn(Tp*)₂ and 5 mM Mn(Tp*)₂SbF₆. Electrolytes contain 0.1 M LiClO₄ in γ -butyrolactone. Potentials scanned from reverse to forward bias at 25 mV/s under 100% sun illumination.

Chapter 3. Rethinking Band Bending at the P3HT-TiO₂ Interface

3.1 Introduction

Next generation solar cells include low-cost, thin hybrid bulk heterojunction solar cells (HBHJs), wherein nanostructured metal oxide semiconductors act as acceptors for conjugated polymer light absorbers.^{83,84} Nanostructured metal oxides provide high surface area for charge injection from polymers, as well as directed electron transport to the electrode. Although high photocurrent can potentially be collected, only efficiencies as high as 3% have been obtained.⁸⁴ Further investigations into the optimization of the organic-inorganic interface are required to realize the full potential of HBHJs.^{15,16,17}

The alignment of donor and acceptor energy levels for thermodynamically favorable photoelectron transfer is paramount for HBHJ device function.⁸⁵ Upon illumination, photoelectrons in the LUMO of the light absorbing polymer are electrostatically bound to the hole created in the HOMO by 0.1-0.3 eV.⁸⁵ The LUMO energy level, E_{LUMO} , must be situated at least 0.3 eV above the energy of the conduction band of TiO₂, E_{CB} , for efficient electron transfer.^{13,14,86} At the same time, a larger energy gap between E_{CB} and the polymer HOMO energy level, E_{HOMO} , allows for greater photovoltage. However, the polymer's optical energy gap must also be optimized to absorb sufficient sunlight (~1.6-2.0 eV). Therefore, ideal materials have a $\Delta E_{\text{LUMO}} - E_{\text{CB}} \geq 0.3$ eV while maintaining high $\Delta E_{\text{CB}} - E_{\text{HOMO}} (\geq 1.3$ eV). This ideal energy alignment imposes requirements on both materials and provides general guidelines for designing light-absorbing polymers. Thus, synthesizing polymers with different energetic properties has garnered much attention in pursuit of HBHJs delivering high power conversion efficiencies.^{15,16,17,11,18}

However, forming a heterojunction alters materials' energetics, complicating the applicability of these general guidelines.⁸⁷ For example, at inorganic semiconductor p-n junctions and some metal-metal junctions, two materials with different Fermi levels (E_F) are brought together, leading to charge transfer and the generation of an interfacial dipole that shifts energy levels at the interface (vacuum level offset).^{88, 89} At thermodynamic equilibrium, the Fermi level (chemical potential of electrons) must be constant throughout the semiconductor junction.⁸⁸ Before equilibration, when two semiconductors with different Fermi levels come into electrical contact, an initial chemical potential gradient at the interface exists, which results in spontaneous electron transfer down the gradient, from the semiconductor with higher E_F to the semiconductor with lower E_F .⁸⁸ Thermodynamic equilibrium is attained when the new charge distribution generates an electric field, extending 10-1000 nm to either side of the interface (interfacial dipole), that prevents further electron transfer.⁸⁸ Since the conduction and valence bands represent the potential energy of electronic states in the region of the electric field, they bend downward or upward in energy.

Charge transfer and band bending can also occur at the interface of polymers with nanocrystalline TiO_2 , but the model of inorganic semiconductors cannot be directly applied.^{22,23, 90,91} Whereas energy level alignment is determined by the initial Fermi level gradient at the interface for semiconductor junctions, it is determined by the TiO_2 Fermi level and the polymer's polaronic energy levels for TiO_2 -polymer junctions.^{12,25} Adding excess electrons or holes to organic materials distorts their molecular geometry, and the excess charge couples with the relaxed geometry, creating polarons with energies in the HOMO-LUMO gap, discussed in more detail below.²⁶ Charge transfer and band bending occur when polaron formation is thermodynamically favorable (vacuum level offset).^{12,25} Forming hole polarons in the polymer leads to downward

band bending, which inhibits photoelectron injection into the TiO_2 .⁹² In contrast, forming electron polarons in the polymer improves photoelectron injection into the TiO_2 .

Herein, spontaneous charge transfer was detected in heterojunctions of poly(3-hexylthiophene) (P3HT) and nanocrystalline TiO_2 , which generates a vacuum level offset. Spectroelectrochemical studies show that TiO_2 donates holes into P3HT upon forming the heterojunction. Charge redistribution between the hole polaron level in P3HT (E_{CT^+}) and the Fermi level of TiO_2 creates an interfacial dipole that bends the P3HT energy levels downward (lower energy away from the interface). Thus, photoelectron injection is inhibited in HBHJ solar cells based on the P3HT- TiO_2 heterojunction. Additionally, raising the TiO_2 Fermi level above E_{CT^+} prevented charge transfer and led to vacuum level alignment, lending further support to the importance of the polaron levels proposed by Salaneck et al.¹² By controlling the direction and magnitude of band bending, solar cells with improved photocurrent and power conversion efficiencies can be designed. Optimized polymers should be designed with electron polaron levels (E_{CT^-}) lower than the Fermi level of TiO_2 , allowing for electron polaron formation and upward band bending that should increase solar cell photocurrent.

3.2 Experimental Methods

HPLC-grade acetonitrile (99.9%) from Spectrum Chemical was distilled once and tetrabutylammonium hexafluorophosphate (TBAPF_6 , >98.0%) from Fluka Analytical was recrystallized four times from ethyl acetate prior to use. 1,2-Dichlorobenzene, tetrahydrothiophene (THT, 99%) and thiophene (>99%) from Sigma Aldrich, 2,5-Dimethylthiophene (DMT, >98%) from Alfa Aesar, and poly(3-hexylthiophene-2,5-diyl) (P3HT, 91-94% regioregularity) from Rieke Metals were used without further purification.

Electrode Preparation. Fluorine-doped tin oxide-coated glass (FTO-glass, 12-14 Ω cm⁻²) was purchased from Hartford Glass Co. for transparent-conducting electrodes. FTO-glass slides (5 x 1 x 0.23 cm) were ultrasonicated for 15 minutes in aqueous AlconoxTM detergent and rinsed with deionized water. The sonication/rinsing cycle was repeated with ethanol and acetone, respectively. After air-drying, transparent mesoporous TiO₂ films (1 cm²) were synthesized by doctor-blading Solaronix T/SP paste (100% anatase, 15-20 nm) onto the cleaned FTO-glass. The films were heated at 450 °C for 30 minutes after a 7 °/min ramp. Reduced-TiO_{2-x} films were prepared by further annealing TiO₂ under vacuum (10⁻⁵ Torr) for 2 hours. While still warm (~80 °C), the films were soaked in vials of 1 mg/mL P3HT in 1,2-dichlorobenzene or 0.1 M thiophene, THT, or DMT in acetonitrile at 60 °C for 6 hours to sensitize the films. Hereafter, sensitized films are referred to as P3HT-TiO₂, thiophene-TiO₂, THT-TiO₂, DMT-TiO₂, or unfunctionalized-TiO₂, respectively. Prior to use, the films were air-dried and rinsed with neat acetonitrile.

Spectroelectrochemistry. The working electrodes, as prepared above, were used in a ground-glass joint quartz cuvette (Quark) with a Pt mesh counter electrode and an Ag/AgCl saturated KCl reference electrode, calibrated with K₄[Fe(CN)₆] from Fisher Scientific. All electrochemistry experiments were performed with 0.1 M TBAPF₆ in acetonitrile as the electrolyte. The electrochemical cells were sealed and purged with argon for 20 minutes to remove dissolved oxygen. Potentials were applied with a BASi Epsilon potentiostat while monitoring the absorbance of the working electrodes with a Cary 5000 UV-Vis-NIR spectrophotometer. The molar absorptivity at 950 nm of TiO₂(e⁻)s (electrons occupying shallow traps in TiO₂) was determined by comparing their absorbance at 800 nm and 950 nm, knowing that $\epsilon = 1300$ M⁻¹ cm⁻¹ at 800 nm.⁹³

X-ray photoelectron spectroscopy (XPS). XPS was conducted using a PHI 5300 spectrometer with a Perkin-Elmer Dual Anode X-ray source operating with magnesium radiation with monochromatic Mg K α radiation (h ν 1253.6 eV) at 13 kV and 250 W and a pass energy of 17.9 eV. Emitted photoelectrons were detected by a hemispherical analyzer and the operating pressure in the sampling chamber was below 10⁻⁷ Torr. The instrument work function was calibrated to adventitious carbon (C 1s peak at 284.8 eV) and an external Ag sample (Ag 3d_{5/2} peak at 383.3 eV).⁹⁴ The spectral scanning range for the valence region was 0-35 eV, with a step size of 0.125 eV and 10 sweeps averaged.

3.3 Results and Discussion

Energy Level Alignment Regimes

Energy level alignment at polymer-TiO₂ heterojunctions is characterized by vacuum level alignment or vacuum level offset. In heterojunctions where charge transfer is thermodynamically unfavorable, upon interfacing the materials, the energy levels of the separated materials are maintained at the interface and their vacuum levels align. In materials where spontaneous charge transfer occurs, an interfacial dipole forms that offsets the respective vacuum levels and bends energy levels near the interface. For vacuum level offset to occur in the polymer-TiO₂ heterojunction, charge transfer into unoccupied states must be thermodynamically favorable.

The relevant charge transfer states in the polymer are not the HOMO and LUMO, but the energy of electron or hole polarons, E_{CT-} and E_{CT+}, respectively.¹² When organic materials are ionized by electron or hole transfer, the molecular geometry distorts near the excess charge.²⁶ The charge couples with the local molecular distortion and forms a polaron, with lower energy than an excess charge on the undistorted molecule. Charge coupling with relaxed molecular distortions creates

electron or hole polaronic states that lie within the HOMO-LUMO gap. For example, electron transfer from the HOMO of neutral P3HT transforms aromatic thiophene units into their quinoid-like counterparts, and the resulting hole polarons are localized to 5-15 thiophene units, positioned 0.2-1 eV above the HOMO energy level.^{22,25,95} The presence of hole polarons in films of oxidized P3HT⁺ and similar conjugated polymers can be detected by visible light absorption changes, in addition to Raman and electron paramagnetic resonance spectroscopies (EPR).^{96,97,98,99}

Energy level alignment in the case of TiO₂ and polymers depends on the possibility of charge transfer between TiO₂ and the polaronic levels. If the Fermi level of TiO₂ is situated in-between E_{CT-} and E_{CT+}, charge transfer between the materials is thermodynamically unfavorable and will not contribute to interfacial dipoles.¹⁸ Therefore, the energy levels will align according to vacuum level alignment, Figure 3-1 a, b. If the Fermi level in TiO₂ is situated below E_{CT+}, holes will transfer to the polymer, creating hole polarons, Figure 3-1c. The resultant interfacial dipole will bend the bands in the polymer downward, inhibiting photoelectron injection. If the Fermi level is situated above E_{CT-}, electrons will transfer to the polymer, creating electron polarons, Figure 3-1d. In this case, the interfacial dipole will bend the bands in the polymer upward, improving photoelectron injection and charge separation.

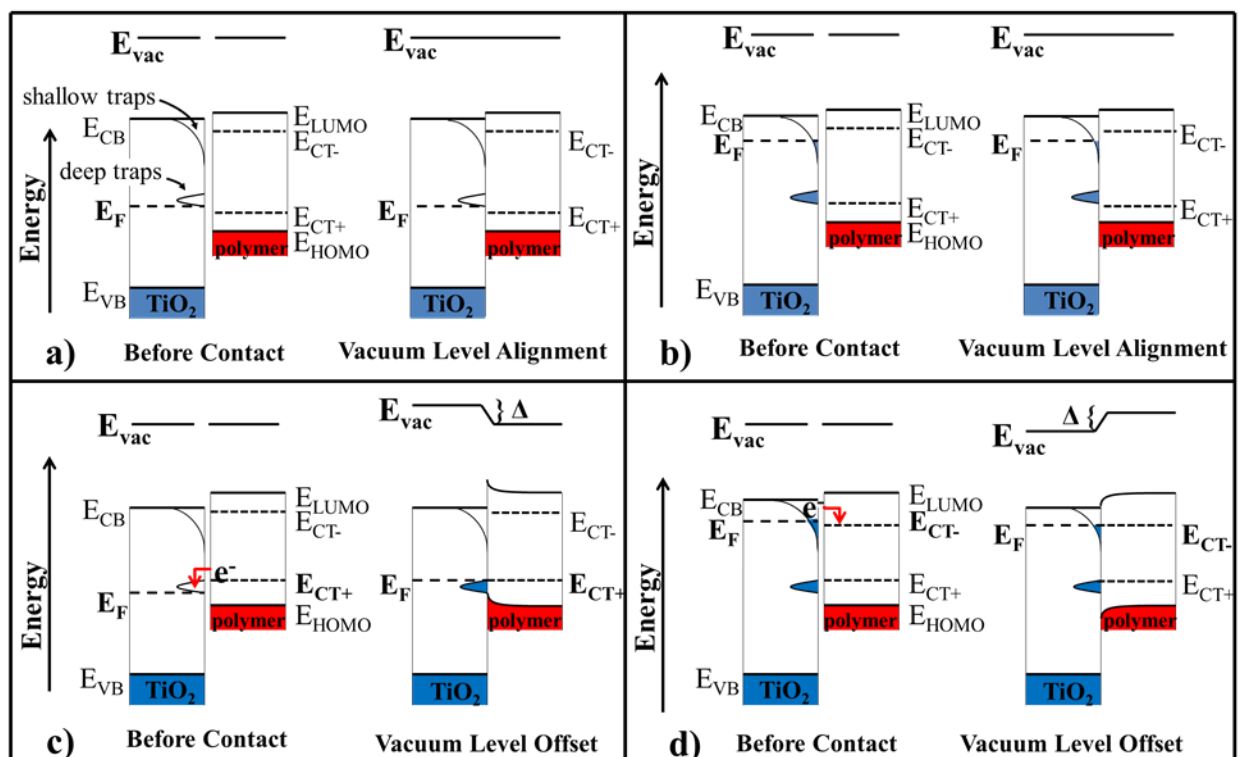


Figure 3-10. Band diagrams illustrating the possible energy alignment regimes in polymer-TiO₂ heterojunctions. The TiO₂ Fermi level between E_{CT-} and E_{CT+} prevents charge transfer and leads to vacuum level alignment, whether E_F in TiO₂ is below deep traps (a) or above deep traps (b). The TiO₂ Fermi level below E_{CT+} (c), or above E_{CT-} (d) results in charge transfer and vacuum level offset. The portion of the vacuum level offset occurring in mesoporous TiO₂ is homogenous throughout the film because band bending is limited by the nanoparticle size (15-20 nm), vide infra.

Charge Transfer between P3HT and TiO₂

Spectroelectrochemistry was utilized to investigate spontaneous charge transfer at P3HT-TiO₂ heterojunctions. Upon forming the P3HT-TiO₂ heterojunction, the P3HT absorbance spectrum exhibits two features different than films of P3HT alone. P3HT on TiO₂ displays reduced $\pi-\pi^*$

absorbance and increased sub-gap absorbance as compared to P3HT on FTO-glass. After applying -0.5 V vs. Ag/AgCl, the ground state absorbance is observed in P3HT-TiO₂, i.e. full π - π^* absorbance, Figure 3-2a.

The spectroelectrochemical response of P3HT films on FTO-glass was studied to determine the absorbance spectra of the neutral and oxidized states of P3HT. The onset of P3HT oxidation occurs at +0.2 V vs. Ag/AgCl (0.1 M TBAPF₆ in MeCN), in accord with the onset of absorbance changes. Due to electronic transitions within the HOMO-LUMO gap, formation of hole polarons in P3HT⁺ leads to increased sub-gap absorbance of near-infrared light and a concomitant bleach of ground state absorbance from π - π^* transitions in neutral P3HT, Figure 3-2b (black).⁹⁶ Unlike P3HT-TiO₂, application of -0.5 V did not affect the absorbance spectrum of P3HT alone, Figure S3-1a.

Spectroelectrochemistry of P3HT-TiO₂ heterojunctions showed features consistent with P3HT oxidation, i.e., increased near-infrared absorbance and decreased absorbance around 500 nm. Applying reductive potentials to the heterojunction leads to an increase in absorbance from π - π^* transitions and a decrease in sub-gap absorbance, Figure 3-2a (blue). Fresh P3HT films on FTO-glass display their fully neutral absorbance and are not affected by application of potentials <0.2 V vs. Ag/AgCl. In contrast, P3HT on TiO₂ is spontaneously oxidized and application of reductive potentials is necessary to observe the fully neutral absorbance, Figure 3-2a (blue). Therefore, upon making the heterojunction, electron transfer from P3HT into mesoporous TiO₂ films is spontaneous and forms hole polarons in P3HT.

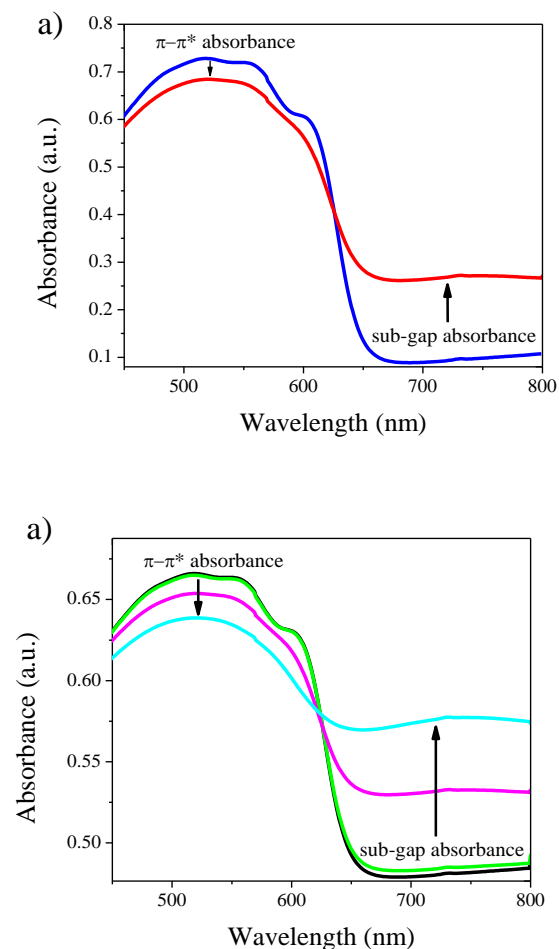


Figure 3-2. Spectroelectrochemistry of P3HT-TiO₂ and P3HT alone. a) Oxidized P3HT-TiO₂ with no applied potential (red), neutral P3HT-TiO₂ after applying -0.5 V (blue). b) Neutral P3HT (black), oxidized P3HT after applying +0.2 V vs. Ag/AgCl (green), +0.4 V (magenta), and +0.6 V (cyan).

Electron transfer is energetically favorable if unoccupied states in the TiO₂ band gap are located below the hole polaron energy level, E_{CT+} . Oxygen vacancies in TiO₂ create deep traps ~ 0.5 -1 eV below the conduction band that can accept electrons, assuming the traps are partially unoccupied.¹⁰⁰ By annealing TiO₂ films in an oxygen-deficient atmosphere (450 °C, vacuum), reduced-TiO_{2-x} forms, wherein excess negative charge on Ti³⁺ sites increases the Fermi level,

leading to occupied deep traps.^{101,102} Unlike stoichiometric TiO₂, the higher Fermi level in reduced-TiO_{2-x} does not allow spontaneous electron transfer from P3HT, Figure S3-1b. In this case, P3HT remains neutral, evidenced by an absorbance spectrum unaffected by applying reductive potentials. Reduction of TiO₂ and the resultant increase in E_F above E_{CT+} precludes favorable charge transfer, as in Figure 3-1b. Preventing oxidation by increasing the Fermi level to form reduced-TiO_{2-x} corroborates the assignment of P3HT oxidation to charge transfer, rather than chemical doping by atmospheric O₂ and ambient UV radiation catalyzed by the TiO₂ surface.^{103,104,105,106} Additionally, P3HT films alone were not significantly oxidized by ambient conditions in the experimental time-frame, Figure S3-1b.

For the first time, charge transfer was detected upon making P3HT-TiO₂ heterojunctions. Absorbance features indicative of hole polarons in P3HT were created when interfacing the polymer with TiO₂. Illustrated by Figure 3-1c, unoccupied deep traps in TiO₂ can transfer holes forming hole polarons at the E_{CT+} level in P3HT. However, reduced-TiO_{2-x}, with a higher E_F and occupied deep traps, does not allow for the oxidative charge transfer. As discussed below, the Fermi level in TiO₂ with and without P3HT can be determined by XPS, providing additional support to the charge transfer and vacuum level offset.

Vacuum Level Offset

As in semiconductor p-n junctions, upon making heterojunctions with organic layers, charge transfer results in an interfacial dipole that offsets the respective vacuum levels, Δ , Figure 3-1c,d.²³ Experimentally, vacuum levels are measured by the energy required to eject electrons from bulk materials to a location near the surface of the sample, E_{vac}(s), although theoretically the vacuum level is defined by the energy of free electrons infinitely far from the sample, E_{vac}(∞).^{95,21} In the

heterojunction, electrons near the surface feel greater affinity for the positively charged material, which has a lower $E_{\text{vac}}(s)$ than the negatively charged material, representing a vacuum level offset.²²

Vacuum level offsets are commonly determined by photoemission spectroscopy by elucidating E_{F} and $E_{\text{vac}}(s)$ of the heterojunction and separated materials.^{25, 90, 107} In XPS spectra, photoemitted electrons from the occupied valence band comprise the signal intensity near E_{F} (zero binding energy). In TiO_2 , the valence band begins 2.0 eV below E_{F} , and an optical band gap of 3.17 ± 0.02 eV (Figure S3-2) places the conduction band 1.17 eV above E_{F} , Figure 3-3 (blue). In accord with n-type materials, E_{F} rests closer to the conduction band, although its exact value depends on the synthetic and annealing procedure of the TiO_2 .¹⁰⁸ Therefore, deep traps from oxygen vacancies (~0.5-1 eV below the conduction band) would be unoccupied and available to accept electrons from P3HT.¹⁰⁰

Compared to 2.0 eV in bare TiO_2 , the valence band in the P3HT- TiO_2 heterojunction is 2.8 eV below E_{F} , Figure 3-3 (red). After equilibrating the Fermi level in TiO_2 with E_{CT^+} , charge transfer between P3HT and TiO_2 results in an interfacial dipole offsetting the vacuum levels by $\Delta = 0.8$ eV. As in Figure 3-1c, the vacuum level is higher at the surface of TiO_2 with a downward gradient towards P3HT. Thus, the barrier inhibits photoelectron injection from P3HT and the energy level alignment is unfavorable for solar cells. In accord with our XPS data, McGehee et al. used a Kelvin probe technique to determine that a 5 nm layer of P3HT on flat TiO_2 shifted its work function by 0.06 eV towards the vacuum level.¹⁰⁹ The difference in magnitude between these two independent measurements can be attributed to the thickness of the P3HT layer (5 nm vs. 1 μm) and the accessible surface area for mesoporous vs. flat TiO_2 .¹¹⁰

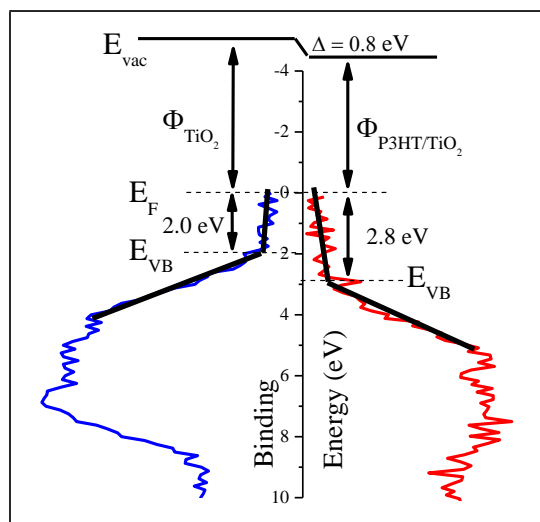


Figure 3-3. XPS spectra of the valence region of TiO_2 (blue) and P3HT- TiO_2 (red). E_{VB} is the valence band maximum and E_{F} is the Fermi level, while Δ is the vacuum level offset, 0.8 eV. The work functions Φ_{TiO_2} , and $\Phi_{\text{P3HT/TiO}_2}$, and E_{vac} are not determined from the XPS data but are represented qualitatively.

Vacuum Level Offsets from Spectroelectrochemistry

Spectroelectrochemistry has previously been utilized to quantify shifts in TiO_2 energetics upon the formation of TiO_2 /molecular interfaces.^{93,111,112} Because this technique is only sensitive to absorbance changes attributed to filled TiO_2 states, it allows for isolation of the shift within the TiO_2 alone, not across the whole junction as measured with XPS. Therefore, it is used to determine the portion of the 0.8 eV vacuum level offset that occurs in TiO_2 . Specifically, this technique probes the energetic position of shallow traps that lie 0-0.5 eV below the TiO_2 conduction band. Reductive potentials more negative than -0.6 V (vs. Ag/AgCl) inject electrons into the shallow trap states, which are quantified by their absorbance of light >400 nm. With increasing negative potential, additional electrons are injected which corresponds to higher absorbance across the

visible-near infrared region, Figure S3-3. In the P3HT-TiO₂ heterojunction, more negative potentials are required to achieve the same absorbance as TiO₂ alone, indicating a shift of the shallow traps towards the vacuum level, Figure 3-4.

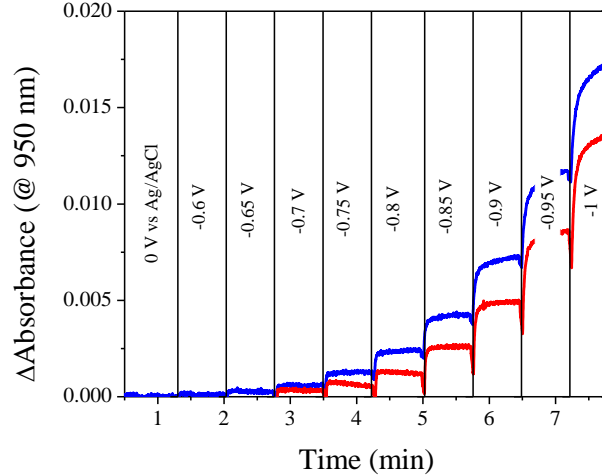


Figure 3-4. Absorbance of 950 nm light during potential-step spectroelectrochemistry is due to electrons being injected into shallow traps in TiO₂ by application of the indicated potentials (blue). In P3HT-TiO₂, more negative potentials are required to achieve the same absorbance change from TiO₂(e⁻)s (red). At these potentials, electron injection into P3HT itself does not occur, Figure S3-4.

From the modified Beer-Lambert law in Equation 1, the molar density of electronic states, Γ , is calculated from the absorbance by electrons occupying the shallow trap states,⁹³

$$\Delta A_{950 \text{ nm}} = \frac{\varepsilon(\text{M}^{-1}\text{cm}^{-1})}{1000 \text{ cm}^3/\text{L}} \Gamma \left(\frac{\text{mol}}{\text{cm}^2} \right) \quad (1)$$

where the molar absorptivity of TiO₂(e⁻)s is taken as 3300 M⁻¹ cm⁻¹ at 950 nm. Faraday's constant translates molar densities into the density of states, g , Equation 2.

$$\Gamma \left(\frac{\text{mol}}{\text{cm}^2} \right) \times 96\,485 \left(\frac{\text{C}}{\text{mol}} \right) = g \left(\frac{\text{C}}{\text{cm}^2} \right) \quad (2)$$

The energetic position of the density of states is illustrated by plotting g as a function of potential. Compared to bare TiO_2 in Figure 3-5 (blue), the onset of shallow traps is shifted towards the vacuum level from -0.6 to -0.7 V when functionalized with P3HT, Figure 3-5 (red). The spectroelectrochemical results were also confirmed with capacitance measurements using cyclic voltammetry, Figure 3S-5. Spectroelectrochemistry was a more sensitive technique, providing a higher level of signal-to-noise.

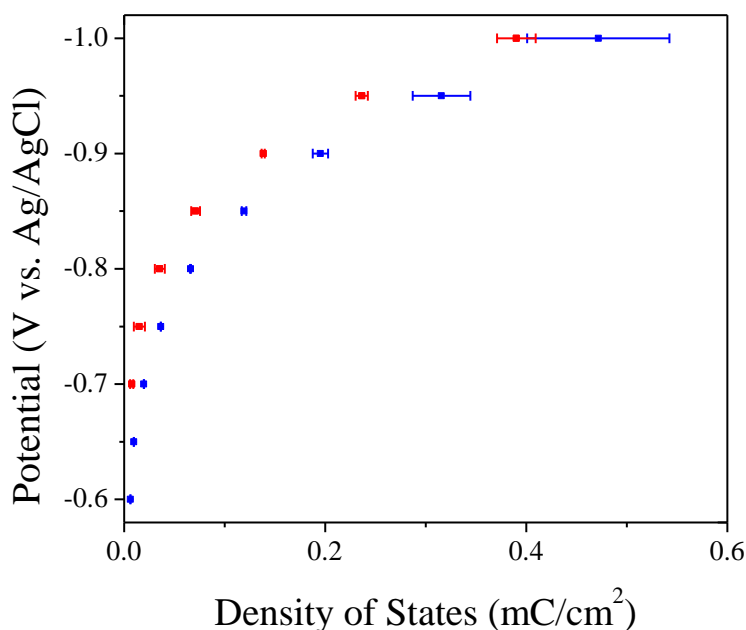


Figure 3-5. Spectroelectrochemistry maps the shallow traps that tail below the conduction band of TiO_2 . Compared to unfunctionalized- TiO_2 (blue), P3HT shifts the potential of the density of states towards the vacuum level (red).

The total vacuum level offset (0.8 eV) is comprised of the energy shift that occurs in the TiO_2 layer and that which occurs in the P3HT layer. As spectroelectrochemistry indicates, the shift of TiO_2 energetics on the vacuum scale contributes 0.1 eV; band bending in the P3HT comprises the

rest of the offset (0.7 eV). The 0.1 eV shift in TiO₂ is assumed to be homogenous over each individual nanoparticle and, therefore, the entire mesoporous film, i.e. there is no observed band bending.^{113,114,115} In contrast to planar TiO₂ films, mesoporous films cannot support an electric field because space charge gradients are limited by the radius of the nanoparticles.^{116,117,118} However, organic materials, including P3HT, can support band bending of the measured 0.7 eV magnitude, which can extend up to 700 nm from the interface.^{12,25,119}

To investigate if P3HT has structure-dependent properties contributing to vacuum level offsets other than charge transfer, molecular thiophene derivatives were used to functionalize TiO₂. By the same mechanism that interfacial dipoles created from charge transfer lead to vacuum level offsets, permanent dipoles at the surface of TiO₂ are known to shift the energetics of its states.^{12,120,3,121} Shifts reported previously have been attributed to the direction and magnitude of dipole moments in molecular monolayers chemisorbed to planar TiO₂.⁴¹ Therefore, small molecule thiophene mimics (tetrahydrothiophene (THT), thiophene, and dimethylthiophene (DMT)) were used to determine if dipole effects could contribute to the observed shift in TiO₂ energy levels. Whereas THT has a 1.87 D dipole moment and two lone pairs localized on the sulfur atom, thiophene has a smaller dipole moment (0.54 D) and only one lone pair. DMT has an even smaller dipole moment (0.51 D) and its sulfur atom is sterically hindered by methyl groups from attaining close contact with TiO₂ and chemisorbing through sulfur.¹²² Similarly, P3HT has hexyl groups sterically hindering chemisorption through sulfur.

In accord with the shift illustrated in Figure 3-6a, sulfur lone pairs on THT can donate electron density towards the shallow traps in TiO₂, thus, requiring higher potentials to further reduce TiO₂ by injecting electrons. However, when the sulfur atom is sterically hindered or the dipole moment is reduced, as in DMT and thiophene, respectively, there is no significant effect, Figure 3-6b and

c. P3HT is most analogous to DMT, in which bulky groups sterically hinder the one lone pair localized on sulfur. Therefore, P3HT is not expected to significantly contribute to energy shifts through a dipole-surface interaction.

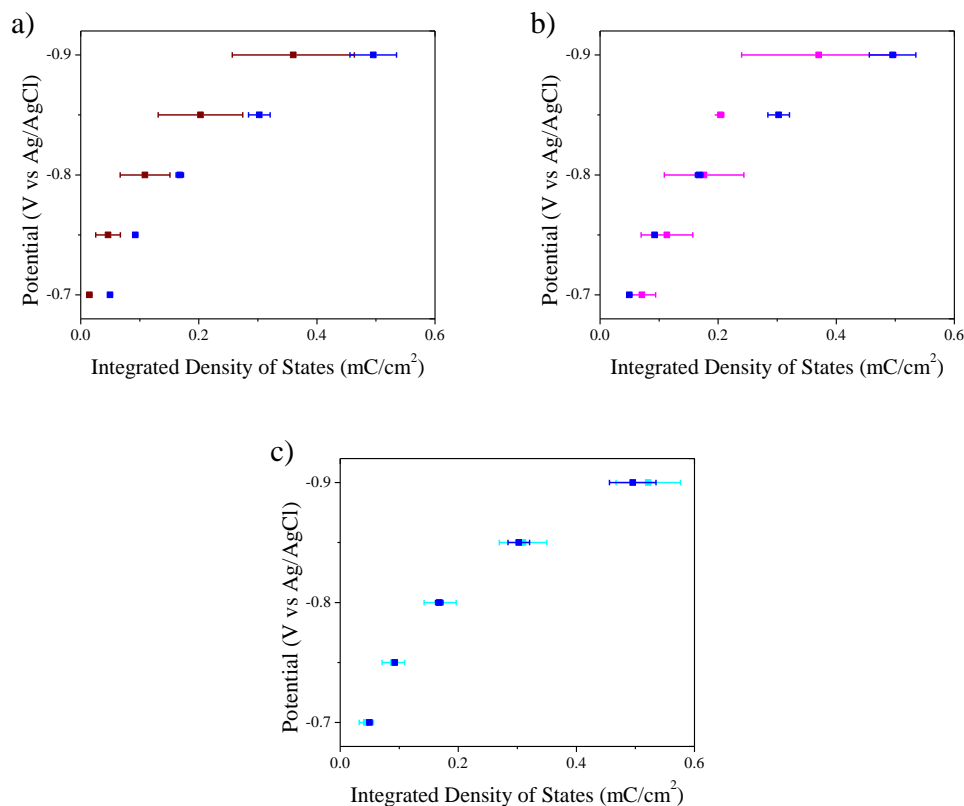


Figure 3-6. The shallow traps in TiO₂ films functionalized with a) tetrahydrothiophene (dark red) are shifted towards the vacuum level compared to unfunctionalized-TiO₂ (blue). b) 2,5-dimethylthiophene (magenta) and c) thiophene (cyan) do not have a significant effect.

Energy Level Diagrams

From the combination of spectroelectrochemical and XPS data, energy level diagrams on the vacuum scale are generated to summarize the energy level alignment in P3HT-TiO₂ heterojunctions, Figure 3-7a. Electrode potentials are translated to the vacuum scale by considering that 0 V vs. Ag/AgCl is -4.7 eV vs. the vacuum level, Figure S3-6.¹²³ The conduction band

minimum is 0.5 eV above the onset of the shallow traps in TiO₂ (-4.1 eV), while deep traps extend 0.5-1eV below the conduction band (-4.1 to -4.6 eV).¹⁰⁰ UV-Vis measurements of the optical gap of TiO₂ place the valence band 3.17 ± 0.02 eV below the conduction band at -6.8 eV, Figure S3-3. The onset of oxidation of P3HT (HOMO) places the Fermi level of TiO₂ below E_{CT+}, which is 0.5-0.9 eV above the HOMO.¹² Downward band bending in the polymer layer, due to the interfacial dipole, imparts a thermodynamic barrier, inhibiting photoelectron injection into TiO₂, contributing to low photocurrents in HBHJs based on P3HT-TiO₂ heterojunctions.

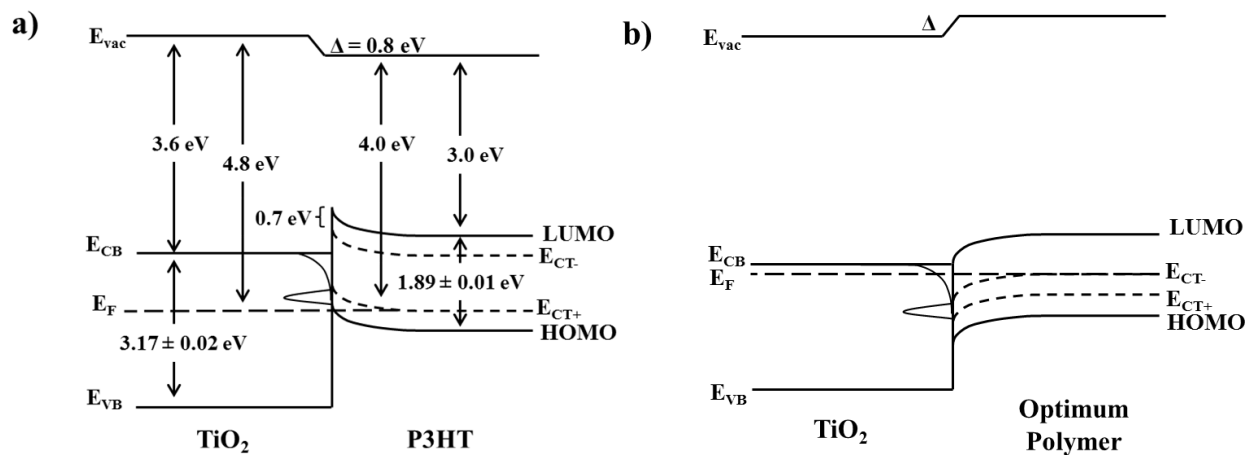


Figure 3-7. Energy level diagram of a) the P3HT-TiO₂ heterojunction and b) the optimum heterojunction. Band bending in P3HT contributes 0.7 eV to the total 0.8 eV vacuum level offset after E_F equilibrates to the hole polaron level in P3HT, E_{CT+}. In the optimized heterojunction, E_F in TiO₂ should equilibrate in the opposite direction, to the electron polaron level, E_{CT-}.

Ideal energy level alignment would result in upward band bending and, in turn, higher photocurrent, Figure 3-7b. For upward band bending, the Fermi level in TiO₂ must be above E_{CT-} but below the LUMO level. Upon making the heterojunction, charge transfer from TiO₂ would create electron polarons in the polymer, forming an electric field in the polymer that would assist

photoelectron injection. Optimized energy level alignment for efficient HBHJs requires the TiO_2 E_F to be close to E_{CB} , $\Delta E_{LUMO-CB} \geq 0.3$ eV, and $E_F > E_{CT-}$ in the separated materials.

These requirements can be met by doping TiO_2 to raise E_F and by rationally designing polymers with electron polaron levels >0.3 eV below the LUMO energy level. A possible method to raise the E_F of TiO_2 is to dope the material with Nb^{5+} forming $\text{Nb}_x\text{Ti}_{1-x}\text{O}_2$.¹²⁴ Unlike other transition metals used to dope TiO_2 , Nb-doping has previously been shown to maintain the overall crystal structure and E_{CB} , while raising E_F within 0.1 eV of the conduction band.¹²⁵ Likewise, doping with Ta^{5+} can raise E_F without significantly affecting the crystal structure or optical properties of TiO_2 .^{124,126} In contrast, even lightly doping with V^{5+} ($<0.1\%$ V:Ti ratio) significantly alters the optical properties, which would complicate the analysis of modifying E_F to optimize the polymer- TiO_2 heterojunction.¹²⁷

To fulfill the energetic requirements for the LUMO of the optimized polymer and ensure that E_{CT-} is below E_F , the E_{CT-} of the ideal polymer needs to be lower compared to P3HT. This is possible since forming E_{CT-} in the range of 0.3-1 eV below the LUMO has been reported.^{12,128} In conjugated polymers, the offset between the LUMO and E_{CT-} is partly determined by the aromaticity of the ring system, since adding an electron transforms aromatic rings to their quinoid counterparts when forming polarons. Highly aromatic homocyclic oligomers, such as pentacene, have $\Delta E_{LUMO-CT-} > 1$ eV.¹²⁸ Therefore, light-absorbing polymers containing highly aromatic units with $\Delta E_{LUMO-CB} \geq 0.3$ eV are potential candidates to achieve upward band bending in polymer- TiO_2 heterojunctions. This is the subject of continued research.

3.4 Conclusions

For the first time, charge transfer in the absence of illumination or an applied potential was detected upon making P3HT-TiO₂ heterojunctions, by spectroelectrochemistry. The resultant vacuum level offset and hole polarons in P3HT illustrate the relevance of polaronic energy levels, E_{CT+} and E_{CT-} , when designing materials for HBHJs. Due to the polaronic nature of organic materials, HBHJs cannot be modeled as a heterojunction of inorganic semiconductors, nor can vacuum level alignment be assumed to occur in all cases. Additionally, spectroelectrochemistry shows that most of the vacuum level offset is manifested as band bending in P3HT, whereas the energetics of TiO₂ are shifted by 0.1 eV throughout the mesoporous film.

Although downward band bending in P3HT-TiO₂ heterojunctions introduces a barrier toward interfacial photoelectron transport, an ideal heterojunction can be designed to impart upward band bending. To fulfill the guidelines developed above for the relative energies of the Fermi level, conduction band and polarons, synthetic modifications, which include TiO₂ doping and employing aromatized polymer structures, provide conditions for the thermodynamically favorable formation of electron polarons in the polymer. The resultant interfacial dipole at the ideal heterojunction assists the LUMO- E_{CB} gradient in splitting excitons into free charge carriers that produce photocurrent. By this route, the efficiency of HBHJs, currently plagued by low photocurrent (<5 mA/cm²), can be maximized.

3.5 Supplemental Information

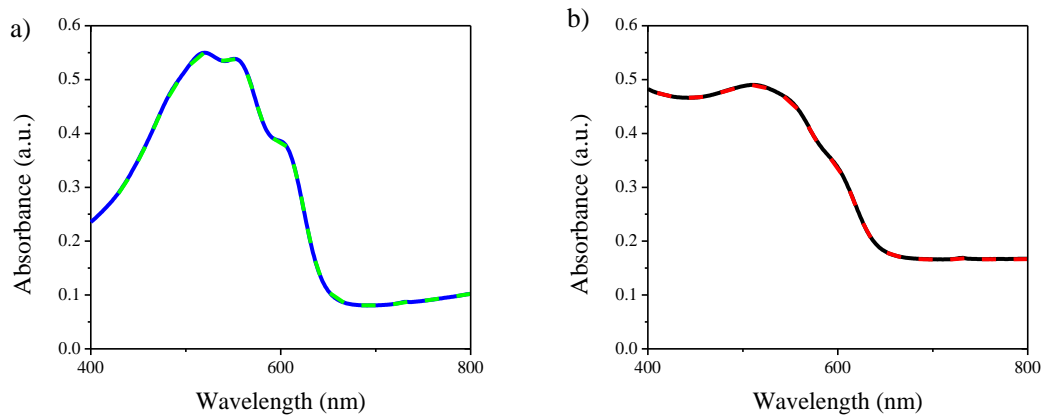


Figure S3-1. a) Films of P3HT alone are not oxidized by ambient conditions in the experimental time-frame, no potential applied (blue) and applying -0.5 V vs. Ag/AgCl (green). b) P3HT is not oxidized by reduced-TiO₂ as its absorbance is unchanged when applying -0.5 V (black and red).

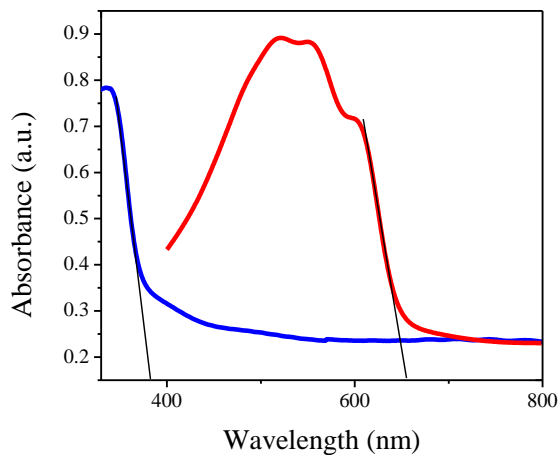


Figure S3-2. Spectra of TiO₂ (blue) and P3HT film (red) to determine band gap and HOMO/LUMO gap. For TiO₂, the edge of absorption onset is extrapolated to 389 nm = 3.17 ±0.02 eV. For P3HT, the edge of absorption onset is extrapolated to 656 nm = 1.89 ±0.01 eV.

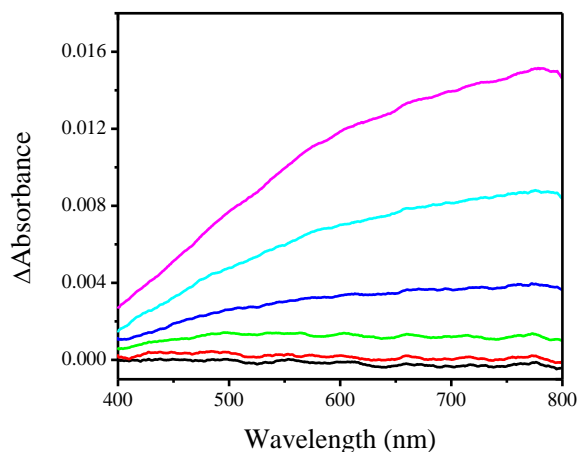


Figure S3-3. Applying potentials more negative than -0.5 V vs. Ag/AgCl to mesoporous TiO₂ films results in the increased absorbance of light by injected conduction band electrons. Black: -0.6 V, red: -0.7 V, green: -0.8 V, blue: -0.9 V, cyan: -1 V, magenta: -1.1 V.

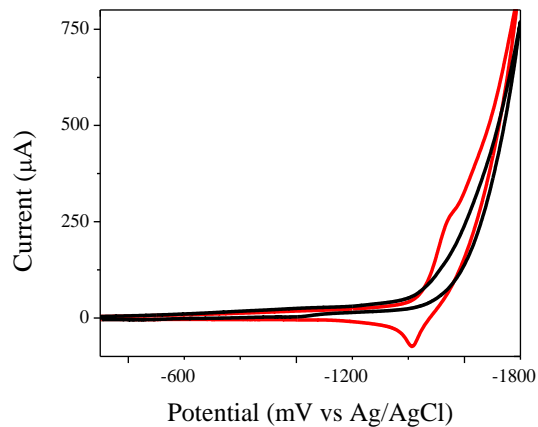


Figure S3-4. Cyclic voltammetry of a P3HT film on FTO-glass in 0.1 M TBAPF₆/MeCN purged with nitrogen. P3HT (red) is reduced by application of potentials more negative than -1.47 V vs. Ag/AgCl, compared to bare FTO-glass (black).

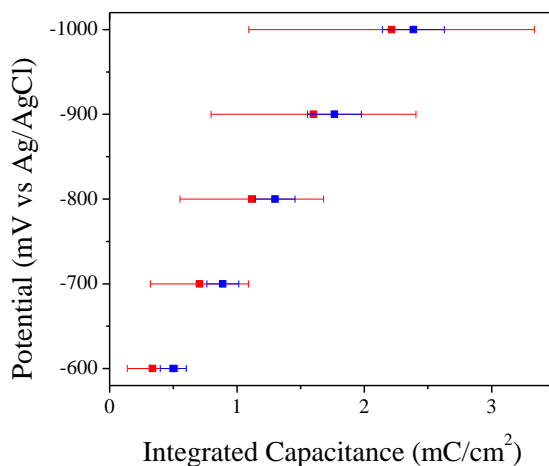


Figure S3-5. Capacitance data determined from integrating charge passed during cyclic voltammetry. There is a shift detected between working electrodes of P3HT-TiO₂ (red) and unfunctionalized-TiO₂ (blue), although standard deviations are high compared to spectroelectrochemical data, Figure 5. Three-electrode setup with an Ag/AgCl reference electrode, Pt mesh counter electrode, and 100 mM TBAPF₆/MeCN electrolyte. Capacitance at each potential is determined by integrating the charge passed during a cyclic voltammogram from 0 mV to the respective potential, scanned at 10 mV/s.

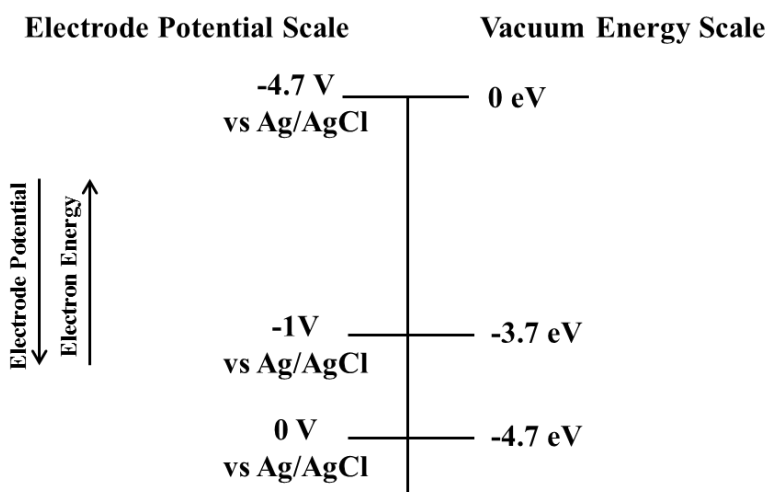


Figure S3-6. Energy scale to convert from electrode potentials to the vacuum scale.¹²³

References

1. Olah, G. A.; Molnár, A., *Hydrocarbon Chemistry*. 2nd ed.; Wiley Interscience,: New York, 2003.
2. National Oceanic and Atmospheric Administration, Trends in Atmospheric Carbon Dioxide at Mauna Loa, 2013.
3. Nazeeruddin, M. K.; Kay, A.; Rodicio, I.; Humphrybaker, R.; Muller, E.; Liska, P.; Vlachopoulos, N.; Gratzel, M., Conversion of light to electricity by cis-X₂bis(2,2'-bipyridyl-4,4'-dicarboxylate)ruthenium(II) charge-transfer sensitizers (X = Cl⁻, Br⁻, I⁻, CN⁻, and SCN⁻) on nanocrystalline TiO₂ electrodes. *Journal of the American Chemical Society* **1993**, *115*, 6382-6390.
4. Ginley, D.; Green, M. A.; Collins, R., Solar energy conversion toward 1 terawatt. *MRS Bulletin* **2008**, *33*, 355-364.
5. Hillhouse, H. W.; Beard, M. C., Solar cells from colloidal nanocrystals: Fundamentals, materials, devices, and economics. *Current Opinion in Colloid & Interface Science* **2009**, *14*, 245-259.
6. Hamann, T. W., The end of iodide? Cobalt complex redox shuttles in DSSCs. *Dalton Transactions* **2012**, *41*, 3111-3115.
7. Nusbaumer, H.; Moser, J. E.; Zakeeruddin, S. M.; Nazeeruddin, M. K.; Gratzel, M., Co-II(dbbiP)(2)(2+) complex rivals tri-iodide/iodide redox mediator in dye-sensitized photovoltaic cells. *Journal of Physical Chemistry B* **2001**, *105*, 10461-10464.
8. Yella, A.; Lee, H. W.; Tsao, H. N.; Yi, C. Y.; Chandiran, A. K., Porphyrin-sensitized solar cells with cobalt (II/III)-based redox electrolyte exceed 12 percent efficiency. *Science* **2011**, *334*, 1203-1203.
9. Wang, J.; Mora-Sero, I.; Pan, Z. X.; Zhao, K.; Zhang, H.; Feng, Y. Y.; Yang, G.; Zhong, X. H.; Bisquert, J., Core/Shell Colloidal Quantum Dot Exciplex States for the Development of Highly Efficient Quantum-Dot-Sensitized Solar Cells. *Journal of the American Chemical Society* **2013**, *135*, 15913-15922.
10. Hossain, F.; Rigsby, M. A.; Duncan, C. T.; Milligan, P. L.; Lord, R. L.; Baik, M. H.; Schultz, F. A., Synthesis, structure, and properties of low-spin manganese(III)-poly(pyrazolyl)borate complexes. *Inorganic Chemistry* **2007**, *46*, 2596-2603.

11. Xu, T. T.; Qiao, Q. Q., Conjugated polymer-inorganic semiconductor hybrid solar cells. *Energy & Environmental Science* **2011**, *4*, 2700-2720.
12. Braun, S.; Salaneck, W. R.; Fahlman, M., Energy-level alignment at organic/metal and organic/organic interfaces. *Advanced Materials* **2009**, *21*, 1450-1472.
13. Scharber, M. C.; Wuhlbacher, D.; Koppe, M.; Denk, P.; Waldauf, C.; Heeger, A. J.; Brabec, C. L., Design rules for donors in bulk-heterojunction solar cells - Towards 10 % energy-conversion efficiency. *Advanced Materials* **2006**, *18*, 789.
14. Halls, J. J. M.; Cornil, J.; dos Santos, D. A.; Silbey, R.; Hwang, D. H.; Holmes, A. B.; Bredas, J. L.; Friend, R. H., Charge- and energy-transfer processes at polymer/polymer interfaces: A joint experimental and theoretical study. *Physical Review B* **1999**, *60*, 5721-5727.
15. Duan, C. H.; Huang, F.; Cao, Y., Recent development of push-pull conjugated polymers for bulk-heterojunction photovoltaics: rational design and fine tailoring of molecular structures. *Journal of Materials Chemistry* **2012**, *22*, 10416-10434.
16. Wright, M.; Uddin, A., Organic-inorganic hybrid solar cells: A comparative review. *Solar Energy Materials and Solar Cells* **2012**, *107*, 87-111.
17. Uy, R. L.; Price, S. C.; You, W., Structure-property optimizations in donor polymers via electronics, substituents, and side chains toward high efficiency solar cells. *Macromolecular Rapid Communications* **2012**, *33*, 1162-1177.
18. Kim, B. G.; Ma, X.; Chen, C.; Je, Y.; Coir, E. W.; Hashemi, H.; Aso, Y.; Green, P. F.; Kieffer, J.; Kim, J., Energy level modulation of HOMO, LUMO, and band-gap in conjugated polymers for organic photovoltaic applications. *Advanced Functional Materials* **2013**, *23*, 439-445.
19. Ashcroft, M., *Solid State Physics*. Brooks/Cole: Belmont, CA, 1976.
20. Brennan, K., *The Physics of Semiconductors*. Press Syndicate: Cambridge, U.K., 1999.
21. Cahen, D.; Kahn, A., Electron energetics at surfaces and interfaces: Concepts and experiments. *Advanced Materials* **2003**, *15*, 271-277.

22. Palermo, V.; Palma, M.; Samori, P., Electronic characterization of organic thin films by Kelvin probe force microscopy. *Advanced Materials* **2006**, *18*, 145-164.
23. Ishii, H.; Hayashi, N.; Ito, E.; Washizu, Y.; Sugi, K.; Kimura, Y.; Niwano, M.; Ouchi, Y.; Seki, K., Kelvin probe study of band bending at organic semiconductor/metal interfaces: examination of Fermi level alignment. *Physica Status Solidi a-Applied Research* **2004**, *201*, 1075-1094.
24. Gao, Y., *Organic Electronics Materials, Processing, Devices and Applications*. CRC Press: Boca Raton Florida, 2010.
25. Davis, R. J.; Lloyd, M. T.; Ferreira, S. R.; Bruzek, M. J.; Watkins, S. E.; Lindell, L.; Sehati, P.; Fahlman, M.; Anthony, J. E.; Hsu, J. W. P., Determination of energy level alignment at interfaces of hybrid and organic solar cells under ambient environment. *Journal of Materials Chemistry* **2011**, *21*, 1721-1729.
26. Bredas, J. L.; Street, G. B., Polarons, bipolarons, and solitons in conducting polymers. *Accounts of Chemical Research* **1985**, *18*, 309-315.
27. Sariciftci, N. S., Polymeric photovoltaic materials. *Current Opinion in Solid State Material Science* **1999**, *4*, 373-378.
28. Kongkanand, A.; Tvrdy, K.; Takechi, K.; Kuno, M.; Kamat, P. V., Quantum dot solar cells. Tuning photoresponse through size and shape control of CdSe-TiO₂ architecture. *Journal of the American Chemical Society* **2008**, *130*, 4007-4015.
29. Pernik, D. R.; Tvrdy, K.; Radich, J. G.; Kamat, P. V., Tracking the Adsorption and Electron Injection Rates of CdSe Quantum Dots on TiO₂: Linked versus Direct Attachment. *Journal of Physical Chemistry C* **2011**, *115*, 13511-13519.
30. Lee, H.; Wang, M. K.; Chen, P.; Gamelin, D. R.; Zakeeruddin, S. M.; Gratzel, M.; Nazeeruddin, M. K., Efficient CdSe Quantum Dot-Sensitized Solar Cells Prepared by an Improved Successive Ionic Layer Adsorption and Reaction Process. *Nano Letters* **2009**, *9*, 4221-4227.
31. Salant, A.; Shalom, M.; Hod, I.; Faust, A.; Zaban, A.; Banin, U., Quantum Dot Sensitized Solar Cells with Improved Efficiency Prepared Using Electrophoretic Deposition. *ACS Nano* **2010**, *4*, 5962-5968.

32. Roy, P.; Berger, S.; Schmuki, P., TiO₂ Nanotubes: Synthesis and Applications. *Angewandte Chemie-International Edition* **2011**, *50*, 2904-2939.
33. Park, J. T.; Patel, R.; Jeon, H.; Kim, D. J.; Shin, J. S.; Kim, J. H., Facile fabrication of vertically aligned TiO₂ nanorods with high density and rutile/anatase phases on transparent conducting glasses: high efficiency dye-sensitized solar cells. *Journal of Materials Chemistry* **2012**, *22*, 6131-6138.
34. Liu, B.; Khare, A.; Aydil, E. S., Synthesis of single-crystalline anatase nanorods and nanoflakes on transparent conducting substrates. *Chemical Communications* **2012**, *48*, 8565-8567.
35. Haring, A.; Morris, A.; Hu, M., Controlling Morphological Parameters of Anodized Titania Nanotubes for Optimized Solar Energy Applications. *Materials* **2012**, *5*, 1890-1909.
36. Yoriya, S.; Mor, G.; Sharma, S.; Grimes, C., Synthesis of ordered arrays of discrete, partially crystalline titania nanotubes by Ti anodization using diethylene glycol electrolytes. *Journal of Materials Chemistry* **2008**, *18*, 3332-3336.
37. Chaudhuri, T.; Kothari, A., ZnO flowers by forced hydrolysis of ammonium zinc complex on hot glass substrates. *J. Optoelect. Biomed. Mat.* **2009**, *1*, 20-24.
38. Wang, Y. X.; Li, X. Y.; Wang, N.; Quan, X.; Chen, Y. Y., Controllable synthesis of ZnO nanoflowers and their morphology-dependent photocatalytic activities. *Separation and Purification Technology* **2008**, *62*, 727-732.
39. Hamann, T. W.; Ondersma, J. W., Dye-sensitized solar cell redox shuttles. *Energy & Environmental Science* **2011**, *4*, 370-381.
40. Ito, S.; Murakami, T. N.; Comte, P.; Liska, P.; Gratzel, C.; Nazeeruddin, M. K.; Gratzel, M., Fabrication of thin film dye sensitized solar cells with solar to electric power conversion efficiency over 10%. *Thin Solid Films* **2008**, *516*, 4613-4619.
41. De Silvestro, J.; Gratzel, M.; Kavan, L.; Moser, J.; Augustynski, J., Highly Efficient Sensitization of Titanium-Dioxide. *Journal of the American Chemical Society* **1985**, *107*, 2988-2990.
42. Vlachopoulos, N.; Liska, P.; Augustynski, J.; Gratzel, M., Very Efficient Visible-Light Energy Harvesting and Conversion by Spectral Sensitization of High Surface-Area

- Polycrystalline Titanium-Dioxide Films. *Journal of the American Chemical Society* **1988**, *110*, 1216-1220.
43. O'Regan, B.; Gratzel, M., A Low-Cost, High-Efficiency Solar-Cell Based on Dye-Sensitized Colloidal TiO₂ Films. *Nature* **1991**, *353*, 737-740.
 44. Hagfeldt, A.; Boschloo, G.; Sun, L. C.; Kloo, L.; Pettersson, H., Dye-Sensitized Solar Cells. *Chem. Rev.* **2010**, *110*, 6595-6663.
 45. Tvrdy, K.; Frantsuzov, P. A.; Kamat, P. V., Photoinduced Electron Transfer from Semiconductor Quantum Dots to Metal Oxide Nanoparticles. *Proceedings of the National Academy of Sciences of the United States of America* **2011**, *108*, 29-34.
 46. Robel, I.; Kuno, M.; Kamat, P. V., Size-Dependent Electron Injection from Excited CdSe Quantum Dots into TiO₂ Nanoparticles. *Journal of the American Chemical Society* **2007**, *129*, 4136-4137.
 47. Gopidas, K. R.; Bohorquez, M.; Kamat, P. V., Photoelectrochemistry in Semiconductor Particulate Systems. 16. Photophysical and Photochemical Aspects of Coupled Semiconductors - Charge-Transfer Processes in Colloidal CdS-TiO₂ and CdS-AgI Systems. *Pharmaceutical and Pharmacological Letters* **1990**, *94*, 6435-6440.
 48. Yu, W. W.; Qu, L. H.; Guo, W. Z.; Peng, X. G., Experimental Determination of the Extinction Coefficient of CdTe, CdSe, and CdS Nanocrystals. *Chemistry of Materials* **2003**, *15*, 2854-2860.
 49. Yu, W. W.; Qu, L. H.; Guo, W. Z.; Peng, X. G., Experimental Determination of the Extinction Coefficient of CdTe, CdSe and Cds Nanocrystals. *Chemistry of Materials* **2004**, *16*, 560-560.
 50. Yella, A.; Lee, H. W.; Tsao, H. N.; Yi, C. Y.; Chandiran, A. K.; Nazeeruddin, M. K.; Diao, E. W. G.; Yeh, C. Y.; Zakeeruddin, S. M.; Gratzel, M., Porphyrin-Sensitized Solar Cells with Cobalt^(II/III)-Based Redox Electrolyte Exceed 12% Efficiency. *Science* **2011**, *334*, 629-634.
 51. Mathew, S.; Yella, A.; Gao, P.; Humphry-Baker, R.; Curchod, B. F. E.; Ashari-Astani, N.; Tavernelli, I.; Rothlisberger, U.; Nazeeruddin, M. K.; Gratzel, M., Dye-Sensitized Solar Cells with 13% Efficiency Achieved Through the Molecular Engineering of Porphyrin Sensitizers. *Nature Chemistry*, **2014**, *6*, 242-247.

52. Wang, J.; Mora-Sero, I.; Pan, Z. X.; Zhao, K.; Zhang, H.; Feng, Y. Y.; Yang, G.; Zhong, X. H.; Bisquert, J., Core/Shell Colloidal Quantum Dot Exciplex States for the Development of Highly Efficient Quantum-Dot-Sensitized Solar Cells. *Journal of the American Chemical Society* **2013**, *135*, 15913-15922.
53. Fisher, A. C.; Peter, L. M.; Ponomarev, E. A.; Walker, A. B.; Wijayantha, K. G. U., Intensity Dependence of the Back Reaction and Transport of Electrons in Dye-Sensitized Nanocrystalline TiO₂ Solar Cells. *Journal of Physical Chemistry B* **2000**, *104*, 949-958.
54. Huang, S. Y.; Schlichthorl, G.; Nozik, A. J.; Gratzel, M.; Frank, A. J., Charge Recombination in Dye-Sensitized Nanocrystalline TiO₂ Solar Cells. *Journal of Physical Chemistry B* **1997**, *101*, 2576-2582.
55. Gardner, J. M.; Giaimuccio, J. M.; Meyer, G. J., Evidence for Iodine Atoms as Intermediates in the Dye Sensitized Formation of I-I Bonds. *Journal of the American Chemical Society* **2008**, *130*, 17252-17253.
56. Nazeeruddin, M. K.; Kay, A.; Rodicio, I.; Humphrybaker, R.; Muller, E.; Liska, P.; Vlachopoulos, N.; Gratzel, M., Conversion of Light to Electricity by *cis*-X₂Bis(2,2'-Bipyridyl-4,4'-Dicarboxylate)Ruthenium(II) Charge-Transfer Sensitizers (X = Cl⁻, Br⁻, I⁻, CN⁻, and SCN⁻) on Nanocrystalline TiO₂ Electrodes. *Journal of the American Chemical Society* **1993**, *115*, 6382-6390.
57. Nakatani, K.; Matsudaira, S.; Tsubomura, H., Photoanodic Behavior of n-type Cadmium-Sulfide in Acetonitrile Solutions Containing Iodide-Ion. *Journal of the Electrochemical Society* **1978**, *125*, 406-409.
58. Radich, J. G.; Dwyer, R.; Kamat, P. V., Cu₂S Reduced Graphene Oxide Composite for High-Efficiency Quantum Dot Solar Cells. Overcoming the Redox Limitations of S₂⁻/S_n²⁻ at the Counter Electrode. *Journal of Physical Chemistry Letters* **2011**, *2*, 2453-2460.
59. Kamat, P. V.; Christians, J. A.; Radich, J. G., Quantum Dot Solar Cells: Hole Transfer as a Limiting Factor in Boosting the Photoconversion Efficiency. *Langmuir* **2014**, *10.1021/la500555w*.
60. Nusbaumer, H.; Moser, J. E.; Zakeeruddin, S. M.; Nazeeruddin, M. K.; Gratzel, M., Co-II(dbbp)₂²⁺ Complex Rivals Tri-Iodide/Iodide Redox Mediator in Dye-Sensitized Photovoltaic Cells. *Journal of Physical Chemistry B* **2001**, *105*, 10461-10464.

61. Sapp, S. A.; Elliott, C. M.; Contado, C.; Caramori, S.; Bignozzi, C. A., Substituted Polypyridine Complexes of Cobalt^(II/III) as Efficient Electron-Transfer Mediators in Dye-Sensitized Solar Cells. *Journal of the American Chemical Society* **2002**, *124*, 11215-11222.
62. Nusbaumer, H.; Zakeeruddin, S. M.; Moser, J. E.; Gratzel, M., An Alternative Efficient Redox Couple for the Dye-Sensitized Solar Cell System. *Chemistry European Journal* **2003**, *9*, 3756-3763.
63. Yum, J. H.; Baranoff, E.; Kessler, F.; Moehl, T.; Ahmad, S.; Bessho, T.; Marchioro, A.; Ghadiri, E.; Moser, J. E.; Yi, C. Y.; Nazeeruddin, M. K.; Gratzel, M., A Cobalt Complex Redox Shuttle for Dye-Sensitized Solar Cells with High Open-Circuit Potentials. *Nature Communications* **2012**, *3*, 631.
64. Feldt, S. M.; Wang, G.; Boschloo, G.; Hagfeldt, A., Effects of Driving Forces for Recombination and Regeneration on the Photovoltaic Performance of Dye-Sensitized Solar Cells using Cobalt Polypyridine Redox Couples. *Journal of Physical Chemistry C* **2011**, *115*, 21500-21507.
65. Achari, M. B.; Elumalai, V.; Vlachopoulos, N.; Safdari, M.; Gao, J. J.; Gardner, J. M.; Kloo, L., A Quasi-Liquid Polymer-Based Cobalt Redox Mediator Electrolyte for Dye-Sensitized Solar Cells. *Physical Chemistry Chemical Physics* **2013**, *15*, 17419-17425.
66. Lee, H. J.; Yum, J. H.; Leventis, H. C.; Zakeeruddin, S. M.; Haque, S. A.; Chen, P.; Seok, S. I.; Gratzel, M.; Nazeeruddin, M. K., CdSe Quantum Dot-Sensitized Solar Cells Exceeding Efficiency 1% at Full-Sun Intensity. *Journal of Physical Chemistry C* **2008**, *112*, 11600-11608.
67. Lee, H. J.; Chen, P.; Moon, S. J.; Sauvage, F.; Sivula, K.; Bessho, T.; Gamelin, D. R.; Comte, P.; Zakeeruddin, S. M.; Il Seok, S.; Gratzel, M.; Nazeeruddin, M. K., Regenerative PbS and CdS Quantum Dot Sensitized Solar Cells with a Cobalt Complex as Hole Mediator. *Langmuir* **2009**, *25*, 7602-7608.
68. Gregg, B. A.; Pichot, F.; Ferrere, S.; Fields, C. L., Interfacial Recombination Processes in Dye-Sensitized Solar Cells and Methods to Passivate the Interfaces. *Journal of Physical Chemistry B* **2001**, *105*, 1422-1429.
69. Perera, I. R.; Gupta, A.; Xiang, W.; Daeneke, T.; Bach, U.; Evans, R. A.; Ohlin, C. A.; Spiccia, L., Introducing Manganese Complexes as Redox Mediators for Dye-Sensitized Solar Cells. *Physical Chemistry Chemical Physics* **2014**, *10.1039/C3CP54894E*.

70. Liu, Y. R.; Jennings, J. R.; Huang, Y.; Wang, Q.; Zakeeruddin, S. M.; Gratzel, M., Cobalt Redox Mediators for Ruthenium-Based Dye-Sensitized Solar Cells: A Combined Impedance Spectroscopy and Near-IR Transmittance Study. *Journal of Physical Chemistry C* **2011**, *115*, 18847-18855.
71. Santra, P. K.; Kamat, P. V., Mn-Doped Quantum Dot Sensitized Solar Cells: A Strategy to Boost Efficiency over 5%. *Journal of the American Chemical Society* **2012**, *134*, 2508-2511.
72. Yu, X. Y.; Lei, B. X.; Kuang, D. B.; Su, C. Y., High performance and reduced charge recombination of CdSe/CdS quantum dot-sensitized solar cells. *Journal of Materials Chemistry* **2012**, *22*, 12058-12063.
73. Hagfeldt, A.; Boschloo, G.; Sun, L. C.; Kloo, L.; Pettersson, H., Dye-Sensitized Solar Cells. *Chemical Reviews* **2010**, *110*, 6595-6663.
74. Zaban, A.; Greenshtein, M.; Bisquert, J., Determination of the Electron Lifetime in Nanocrystalline Dye Solar Cells by Open-Circuit Voltage Decay Measurements. *ChemPhysChem* **2003**, *4*, 859-864.
75. Fu, Y. S.; Cole, A. S.; Swaddle, T. W., Solvent Dynamics and Pressure Effects in the Kinetics of the Tris(Bipyridine)Cobalt(III/II) Electrode Reaction in Various Solvents. *Journal of the American Chemical Society* **1999**, *121*, 10410-10415.
76. Ito, N.; Saji, T.; Aoyagui, S., Electrochemical Formation of Stable Ferrocene Ion and the Formal Rate-Constant of the Ferrocene^{0/-} Electrode. *Journal of Organometallic Chemistry* **1983**, *247*, 301-305.
77. Gonzalez-Pedro, V.; Xu, X. Q.; Mora-Sero, I.; Bisquert, J., Modeling High-Efficiency Quantum Dot Sensitized Solar Cells. *ACS Nano* **2010**, *4*, 5783-5790.
78. Mora-Sero, I.; Gimenez, S.; Fabregat-Santiago, F.; Gomez, R.; Shen, Q.; Toyoda, T.; Bisquert, J., Recombination in Quantum Dot Sensitized Solar Cells. *Accounts of Chemical Research* **2009**, *42*, 1848-1857.
79. Bisquert, J.; Fabregat-Santiago, F.; Mora-Sero, I.; Garcia-Belmonte, G.; Gimenez, S., Electron Lifetime in Dye-Sensitized Solar Cells: Theory and Interpretation of Measurements. *Journal of Physical Chemistry C* **2009**, *113*, 17278-17290.

80. Gonzalez-Pedro, V.; Sima, C.; Marzari, G.; Boix, P. P.; Gimenez, S.; Shen, Q.; Dittrich, T.; Mora-Sero, I., High Performance PbS Quantum Dot Sensitized Solar Cells Exceeding 4% Efficiency: The Role of Metal Precursors in the Electron Injection and Charge Separation. *Physical Chemistry Chemical Physics* **2013**, *15*, 13835-13843.
81. Nelson, J. J.; Amick, T. J.; Elliott, C. M., Mass Transport of Polypyridyl Cobalt Complexes in Dye-Sensitized Solar Cells with Mesoporous TiO₂ Photoanodes. *Journal of Physical Chemistry C* **2008**, *112*, 18255-18263.
82. Klahr, B. M.; Hamann, T. W., Performance Enhancement and Limitations of Cobalt Bipyridyl Redox Shuttles in Dye-Sensitized Solar Cells. *Journal of Physical Chemistry C* **2009**, *113*, 14040-14045.
83. Boucle, J.; Ackermann, J., Solid-state dye-sensitized and bulk heterojunction solar cells using TiO₂ and ZnO nanostructures: recent progress and new concepts at the borderline. *Polymer International* **2012**, *61*, 355-373.
84. Zhou, Y. F.; Eck, M.; Kruger, M., Bulk-heterojunction hybrid solar cells based on colloidal nanocrystals and conjugated polymers. *Energy & Environmental Science* **2010**, *3*, 1851-1864.
85. Bredas, J. L.; Beljonne, D.; Coropceanu, V.; Cornil, J., Charge-transfer and energy-transfer processes in pi-conjugated oligomers and polymers: A molecular picture. *Chemical Reviews* **2004**, *104*, 4971-5003.
86. Clarke, T. M.; Ballantyne, A. M.; Tierney, S.; Heaney, M.; Duffy, W.; McCulloch, I.; Nelson, J.; Durrant, J. R., Charge photogeneration in low band gap polyselenophene/fullerene blend films. *Journal of Physical Chemistry C* **2010**, *114*, 8068-8075.
87. Berhe, S. A.; Zhou, J. Y.; Haynes, K. M.; Rodriguez, M. T.; Youngblood, W. J., Electron transport in acceptor-sensitized polymer-oxide solar cells: the importance of surface dipoles and electron cascade effects. *ACS Applied Materials & Interfaces* **2012**, *4*, 2955-2963.
88. Ashcroft, M., Inhomogenous Semiconductors. In *Solid State Physics*, Brooks/Cole: Belmont, CA, 1976; pp 592-597.

89. Jennings, P. C.; Pollet, B. G.; Johnston, R. L., Electronic properties of Pt-Ti nanoalloys and the effect on reactivity for use in PEMFCs. *Journal of Physical Chemistry C* **2012**, *116*, 15241-15250.
90. Greiner, M. T.; Helander, M. G.; Tang, W. M.; Wang, Z. B.; Qiu, J.; Lu, Z. H., Universal energy-level alignment of molecules on metal oxides. *Nature Materials* **2012**, *11*, 76-81.
91. Ley, L.; Smets, Y.; Pakes, C. I.; Ristein, J., Calculating the universal energy-level alignment of organic molecules on metal oxides. *Advanced Functional Materials* **2013**, *23*, 794-805.
92. While band bending typically refers to phenomenon in materials having a band structure, it is recognized that localized wave functions in organic materials do not form bands. Herein, the more general use of the term 'band' is used to represent a distribution of electronic states, although the band bending phenomenon is equivalent. This is consistent with the terminology used by the scientific community concerned with band bending in organic materials.
93. Morris, A. J.; Meyer, G. J., TiO₂ surface functionalization to control the density of states. *Journal of Physical Chemistry C* **2008**, *112*, 18224-18231.
94. Moulder, J. F. S., W.F.; Sobol, P.E.; Bombem, K.D., *Handbook of X-ray Photoelectron Spectroscopy*. Physical Electronics, Inc.: 1995.
95. Ishii, H.; Sugiyama, K.; Ito, E.; Seki, K., Energy level alignment and interfacial electronic structures at organic metal and organic organic interfaces. *Advanced Materials* **1999**, *11*, 605-625.
96. van Haare, J.; Havinga, E. E.; van Dongen, J. L. J.; Janssen, R. A. J.; Cornil, J.; Bredas, J. L., Redox states of long oligothiophenes: Two polarons on a single chain. *Chemistry-A European Journal* **1998**, *4*, 1509-1522.
97. Furukawa, Y., Electronic absorption and vibrational spectroscopies of conjugated conducting polymers. *Journal of Physical Chemistry* **1996**, *100*, 15644-15653.
98. Yu, W. J.; Zhou, J. W.; Bragg, A. E., Exciton conformational dynamics of poly(3-hexylthiophene) (P3HT) in solution from time-resolved resonant-raman spectroscopy. *Journal of Physical Chemistry Letters* **2012**, *3*, 1321-1328.

99. Santos, M. J. L.; Brolo, A. G.; Girotto, E. M., Study of polaron and bipolaron states in polypyrrole by in situ Raman spectroelectrochemistry. *Electrochimica Acta* **2007**, *52*, 6141-6145.
100. Salvador, P.; Hidalgo, M. G.; Zaban, A.; Bisquert, J., Illumination intensity dependence of the photovoltage in nanostructured TiO₂ dye-sensitized solar cells. *Journal of Physical Chemistry B* **2005**, *109*, 15915-15926.
101. Di Valentin, C.; Pacchioni, G.; Selloni, A., Reduced and n-Type Doped TiO₂: Nature of Ti³⁺ Species. *Journal of Physical Chemistry C* **2009**, *113*, 20543-20552.
102. Nowotny, M. K.; Bak, T.; Nowotny, J., Electrical properties and defect chemistry of TiO₂ single crystal. I. Electrical conductivity. *Journal of Physical Chemistry B* **2006**, *110*, 16270-16282.
103. Abdou, M. S. A.; Orfino, F. P.; Son, Y.; Holdcroft, S., Interaction of oxygen with conjugated polymers: Charge transfer complex formation with poly(3-alkylthiophenes). *Journal of the American Chemical Society* **1997**, *119*, 4518-4524.
104. Sperlich, A.; Kraus, H.; Deibel, C.; Blok, H.; Schmidt, J.; Dyakonov, V., Reversible and irreversible interactions of poly(3-hexylthiophene) with oxygen studied by spin-sensitive methods. *Journal of Physical Chemistry B* **2011**, *115*, 13513-13518.
105. Abdou, M. S. A.; Holdcroft, S., Mechanisms of photodegradation of poly(3-alkylthiophenes) in solution. *Macromolecules* **1993**, *26*, 2954-2962.
106. Hintz, H.; Peisert, H.; Egelhaaf, H. J.; Chasse, T., Reversible and irreversible light-induced p-doping of P3HT by oxygen studied by photoelectron spectroscopy (XPS/UPS). *Journal of Physical Chemistry C* **2011**, *115*, 13373-13376.
107. Tengstedt, C.; Osikowicz, W.; Salaneck, W. R.; Parker, I. D.; Hsu, C. H.; Fahlman, M., Fermi-level pinning at conjugated polymer interfaces. *Applied Physics Letters* **2006**, *88*.
108. Markus, T. Z.; Itzhakov, S.; Akotzer, Y. I.; Cahen, D.; Hodes, G.; Oron, D.; Naaman, R., Energetics of CdSe quantum dots adsorbed on TiO₂. *Journal of Physical Chemistry C* **2011**, *115*, 13236-13241.
109. Liu, Y. X.; Scully, S. R.; McGehee, M. D.; Liu, J. S.; Luscombe, C. K.; Frechet, J. M. J.; Shaheen, S. E.; Ginley, D. S., Dependence of band offset and open-circuit voltage on the

- interfacial interaction between TiO₂ and carboxylated polythiophenes. *Journal of Physical Chemistry B* **2006**, *110*, 3257-3261.
110. Agarwala, S.; Kevin, M.; Wong, A. S. W.; Peh, C. K. N.; Thavasi, V.; Ho, G. W., Mesophase ordering of TiO₂ film with high surface area and strong light harvesting for dye-sensitized solar cell. *ACS Applied Materials & Interfaces* **2010**, *2*, 1844-1850.
 111. Fitzmaurice, D., Using spectroscopy to probe the band energetics of transparent nanocrystalline semiconductor-films. *Solar Energy Materials and Solar Cells* **1994**, *32*, 289-305.
 112. Ondersma, J. W.; Hamann, T. W., Conduction band energy determination by variable temperature spectroelectrochemistry. *Energy & Environmental Science* **2012**, *5*, 9476-9480.
 113. Curran, J. S.; Lamouche, D., Transport and kinetics in photoelectrolysis by semiconductor particles in suspension. *Journal of Physical Chemistry* **1983**, *87*, 5405-5411.
 114. Albery, W. J.; Bartlett, P. N., The transport and kinetics of photogenerated carriers in colloidal semiconductor electrode particles. *Journal of the Electrochemical Society* **1984**, *131*, 315-325.
 115. Emeline, A. V.; Ryabchuk, V. K.; Serpone, N., Spectral dependencies of the quantum yield of photochemical processes on the surface of nano-/microparticulates of wide-band-gap metal oxides. 1. Theoretical approach. *Journal of Physical Chemistry B* **1999**, *103*, 1316-1324.
 116. Kytin, V.; Dittrich, T.; Bisquert, J.; Lebedev, E. A.; Koch, F., Limitation of the mobility of charge carriers in a nanoscaled heterogeneous system by dynamical Coulomb screening. *Physical Review B* **2003**, *68*, 195308.
 117. Law, M.; Greene, L. E.; Johnson, J. C.; Saykally, R.; Yang, P. D., Nanowire dye-sensitized solar cells. *Nature Materials* **2005**, *4*, 455-459.
 118. Hagfeldt, A.; Gratzel, M., Light-induced redox reactions in nanocrystalline systems. *Chemical Reviews* **1995**, *95*, 49-68.

119. Hayashi, N.; Ishii, H.; Ouchi, Y.; Seki, K., Examination of band bending at buckminsterfullerene (C-60)/metal interfaces by the Kelvin probe method. *Journal of Applied Physics* **2002**, *92*, 3784-3793.
120. Huang, S. Y.; Schlichthorl, G.; Nozik, A. J.; Gratzel, M.; Frank, A. J., Charge recombination in dye-sensitized nanocrystalline TiO₂ solar cells. *Journal of Physical Chemistry B* **1997**, *101*, 2576-2582.
121. Goh, C.; Scully, S. R.; McGehee, M. D., Effects of molecular interface modification in hybrid organic-inorganic photovoltaic cells. *Journal of Applied Physics* **2007**, *101*.
122. Dipole moments of aromatic heterocycles. In *Theoretical Organic Chemistry*, Parkanyi, C., Ed. Elsevier Science: Amsterdam, 1998; p 234.
123. Cahen, D.; Hodes, G.; Gratzel, M.; Guillemoles, J. F.; Riess, I., Nature of photovoltaic action in dye-sensitized solar cells. *Journal of Physical Chemistry B* **2000**, *104*, 2053-2059.
124. Ruiz, A. M.; Dezanneau, G.; Arbiol, J.; Cornet, A.; Morante, J. R., Insights into the structural and chemical modifications of Nb additive on TiO₂ nanoparticles. *Chemistry of Materials* **2004**, *16*, 862-871.
125. Nikolay, T.; Larina, L.; Shevaleevskiy, O.; Ahn, B. T., Electronic structure study of lightly Nb-doped TiO₂ electrode for dye-sensitized solar cells. *Energy & Environmental Science* **2011**, *4*, 1480-1486.
126. Stengl, V.; Hougkova, V.; Bakardjieva, S.; Murafa, N.; Bezdicka, P., Niobium and tantalum doped titania particles. *Journal of Materials Research* **2010**, *25*, 2015-2024.
127. Devi, L. G.; Murthy, B. N.; Kumar, S. G., Photocatalytic activity of TiO₂ doped with Zn²⁺ and V⁵⁺ transition metal ions: Influence of crystallite size and dopant electronic configuration on photocatalytic activity. *Materials Science and Engineering B-Advanced Functional Solid-State Materials* **2010**, *166*, 1-6.
128. Ryno, S. M.; Lee, S. R.; Sears, J. S.; Risko, C.; Bredas, J. L., Electronic polarization effects upon charge injection in oligoacene molecular crystals: description via a polarizable force field. *Journal of Physical Chemistry C* **2013**, *117*, 13853-13860.

Appendix

Controlling Morphological Parameters of Anodized Titania Nanotubes for Optimized Solar Energy Applications

1. Introduction

Ordered TiO₂ nanostructures, including nanoparticles, nanotubes, and nanorods^{1, 2} have garnered much research for their use in solar energy applications.³⁻⁵ In hybrid solar cells, the titania nanostructures accept electrons from photoexcited dye molecules or polymers adsorbed to the surface and direct the electrons to an external circuit. In photoelectrochemical cells for the degradation of pollutants or the oxidation of water, the photoexcited titania nanostructures donate electrons or holes to chemical species adsorbed to the surface. TiO₂ nanotubes have also been experimentally applied as gas sensors and supercapacitors but these applications will not be discussed.

In 1999, Zwillling *et al.* reported on the anodization of titanium in solutions of fluoride-containing electrolytes to form porous titania nanotubes and Gong *et al.* later formed nanotubes using higher voltages (Figure A-1).^{8, 9} Although titania nanotubes can also be formed by other routes¹⁰ the anodization method leads to an aligned array with an adjustable morphology that can be optimized for its various applications. The morphological parameters, e.g., nanotube length, diameter, smoothness, depend on the anodization conditions, such as voltage, electrolyte composition, temperature, and duration. After anodization, the amorphous nanotubes can be annealed to increase the electron mobility, sensitized with dyes or polymers to increase solar photon absorption, and doped or surface-functionalized to adjust the density of states.¹¹⁻¹³

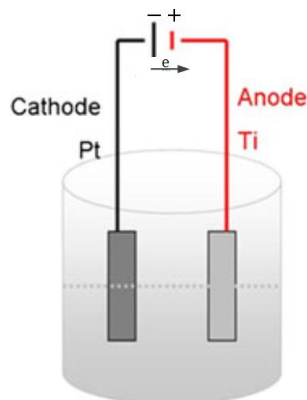


Figure A-1. Basic setup for the anodization of titanium to titania nanotubes. Reprinted with permission from.¹⁴

Since Honda and Fujishima reported water oxidation by titania thin films in 1972, titania nanoparticles, nanorods and nanotubes have been investigated.¹⁵⁻¹⁸ Due to their hollow nature, nanotubes have twice the surface area per unit volume compared to nanoparticles and nanorods that have the same outside diameter as the nanotubes. Recently, Zhang and Wang fabricated a photoelectrochemical cell for water splitting that achieved a photoconversion efficiency of 0.84% under AM 1.5 illumination using titania nanotubes without any catalysts.¹⁸

Hybrid solar cells with titania nanotubes, illustrated in Figure A-2, have several advantages over other nanostructures and planar solar cells. Nanotubes, which are aligned perpendicular to the conducting substrate, increase electron mobility within the nanotube by directing electrons along a shorter path than nanoparticles.^{19, 20} The high surface area of nanotubes, compared to nanorods or flat surfaces, allows for more adsorption by electron donors such as molecular dyes and polymers, thus increasing solar photon absorption and charge collection.²¹ Commonly used donors include ruthenium polypyridyl complexes (N719, N749), porphyrin dyes, poly(3-hexylthiophene), and poly(*p*-phenylene vinylene) derivatives.²²⁻²⁵ Although titania nanotubes have attracted extensive research as photoanodes in hybrid solar cells, there are several complications that need to be overcome, including phase separation between electron donors and titania, polymer penetration into the nanotubes, and efficient electrical contact with conductive glass.^{20, 26}

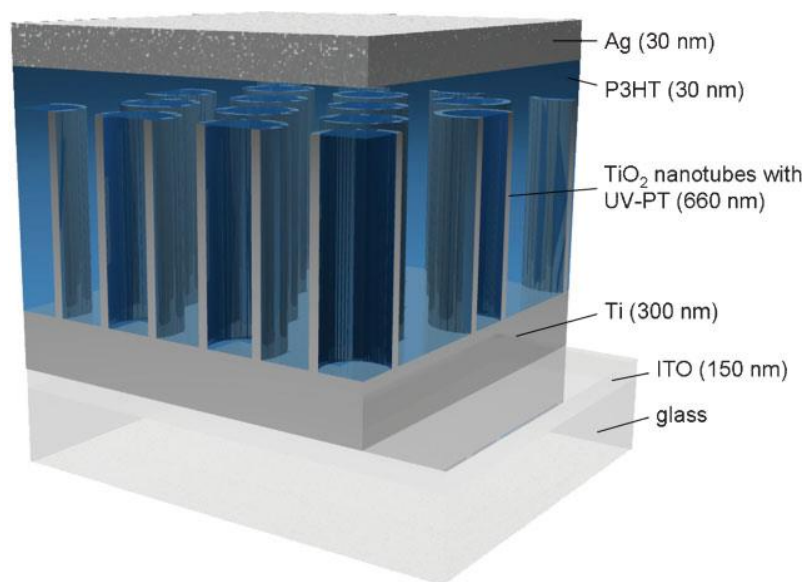
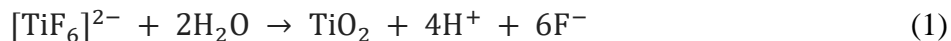


Figure A-2. Solid-state solar cell with nanotubes sensitized by polythiophene formed in the nanotubes. Reprinted with permission from.²¹ Copyright 2009 Wiley.

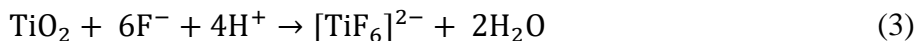
2. Anodized Titania Nanotube Formation

The formation of titania nanotubes by potentiostatic anodization proceeds by similar mechanisms as that of porous alumina.^{27, 28} In the first step of the anodization process, the titanium

surface is electrochemically oxidized. A compact layer of titanium oxide is formed on the titanium surface through Equation (1).²⁷⁻²⁹



The electrolyte typically contains 0.1 M HF or NH_4F , providing fluoride ions that complex with Ti^{4+} , Equation (2), and dissolve TiO_2 , Equation (3).²⁷⁻²⁹



Pitting of the oxide layer provides preferential locations for the field-assisted chemical dissolution of TiO_2 by fluoride ions through Equations (2) and (3).²⁷⁻²⁹ Nanotubes are formed as the pits are chemically dissolved further into the oxide layer; the pits provide the least resistive route for the current; therefore the high dissolution rate forms the inside of the tubes from the pits. To form highly ordered nanotubes, the first nanotube array is often removed from the titanium foil, leaving indentations that facilitate the pitting behavior during re-anodization (Figure A-3).³⁰ During the formation, the current typically behaves as illustrated in Figure A-4. As the voltage increases to its set magnitude, the current increases (Region I) until the oxide layer provides enough resistance that the current decreases (Region II). The current increases again as Equation (2) begins to increase the surface area and thin the oxide layer. The oxidation continues and a steady state between Equations (1)–(3) is reached in Region III (Figure A-4).^{3, 28} Wang *et al.* recently published on the formation of metal oxides by anodization and analyze the formation thermodynamically and mechanistically.²⁷

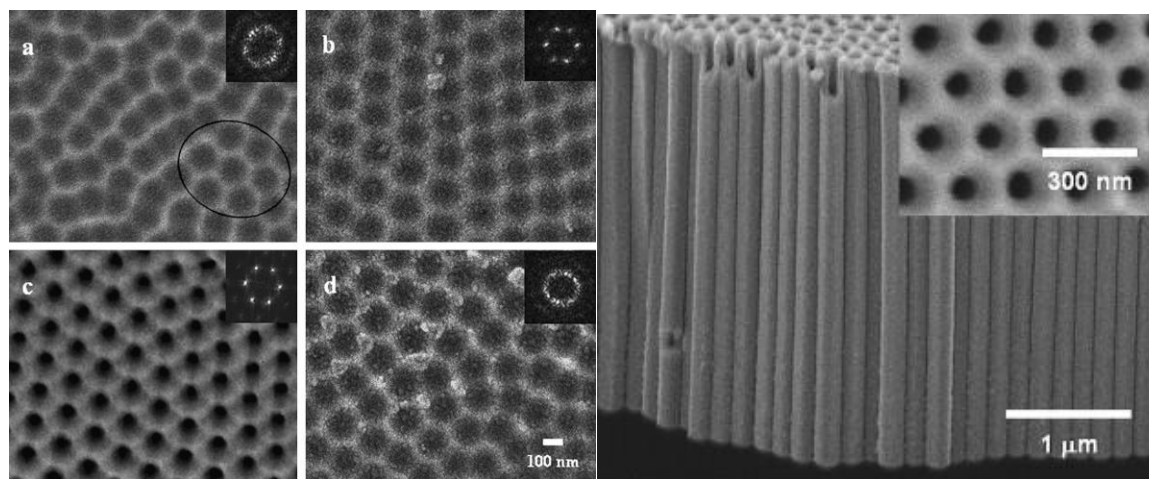


Figure A-3. Scanning electron micrographs (SEM) of titanium substrate after removal of (a) first; (b) second; and (d) third nanotube array. Reprinted with permission from²⁹ Copyright 2007 Elsevier.

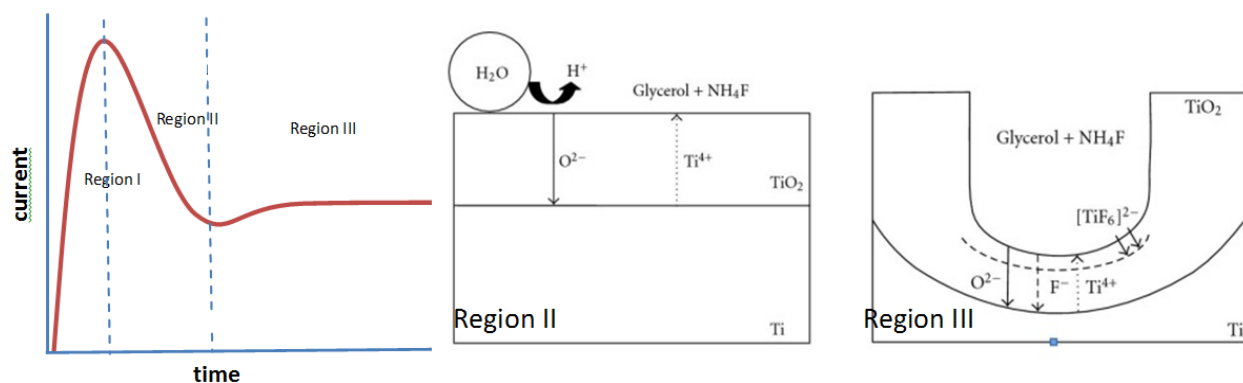


Figure A-4. The current profile and nanotube formation scheme are shown. The current increases sharply in Region I as voltage is applied across the electrolyte and bare titanium foil. A compact titanium dioxide layer forms in Region II. In Region III, oxide formation and dissolution reach a steady state and nanotubes form (Equations (1)–(3)). Illustrations reprinted from³⁰ Creative Commons 2010.

2.1. Control of Morphology

Many experimental conditions of the anodization process are controlled to form nanotubes with the desired morphology: duration, applied voltage, temperature, Ti foil roughness, electrolyte composition. While the duration, voltage, and fluoride concentration primarily control the nanotube length, diameter, and growth rate, many characteristics of the electrolyte affect the process, including the solvent, water content, pH, viscosity, conductivity, and organic additives. Table A-1 shows the range of conditions that have been used to form titania nanotubes.

Table A-1. Range of conditions used to control the nanotube morphology. Electrolyte age refers to its previous use for titanium anodization.

| | | | |
|-----------------|---|-----------------------|--|
| Voltage | 10–240V ^{31, 32} | Electrolyte Solvent | water, ethylene glycol, diethylene glycol, DMSO, DMF, formamide, acetic acid ^{33, 34} |
| Duration | seconds–9 days ^{35, 36} | Water Content | 0%–100% ³⁷ |
| Etching species | HF, NH ₄ F, Bu ₄ NF ³³ | Electrolyte Additives | Na ₂ EDTA, H ₂ O ₂ lactic acid ^{30, 34, 36} |
| Fluoride Conc. | 0.05–0.5M NH ₄ F ^{3, 30} | Electrolyte Age | unused-120 h ³⁸ |

2.1.1. Nanotube Length

It is well established that the titania nanotube growth rate is directly proportional to the duration of anodization,^{3, 39-43} the concentration of fluoride ions,^{3, 4, 41, 43, 44} the voltage (Figure A-5),^{3, 41-45} and the electrolyte conductivity.^{38, 44, 46} Aqueous electrolytes limit the nanotube

length to 500 nm for acidic and 2 μm for neutral electrolytes, since the rate of Equation (3) is faster in aqueous electrolytes³. The longest nanotubes reported, 1 mm, required nine days of anodization at 60 V with 0.5 wt % NH_4F and 3% water in ethylene glycol.⁴⁷ With the same electrolyte concentration and voltage, 5 μm long nanotubes were obtained after 17 h.⁴³

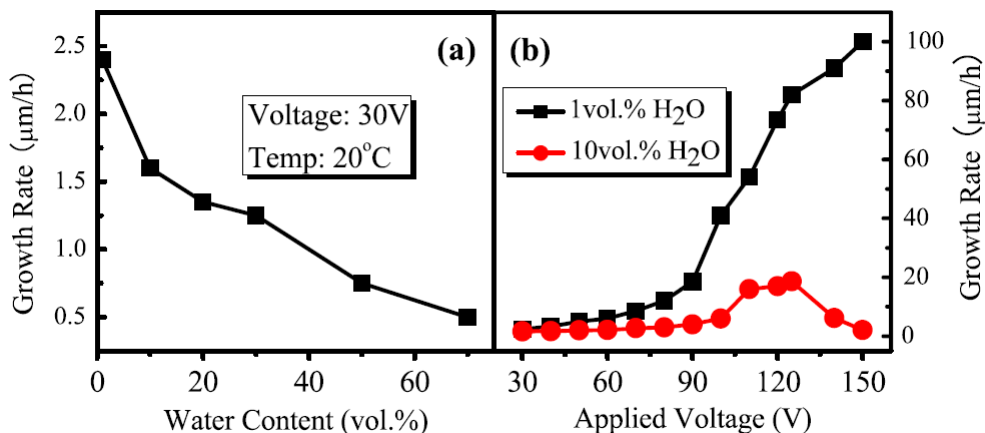


Figure A-5. Effect of (a) water content and (b) anodization voltage on the nanotube growth rate using 0.09 M (0.3 wt %) NH_4F in ethylene glycol. Reprinted with permission from³⁵. Copyright 2010 IOP Publishing.

Nanotube formation requiring long anodization durations would not be time-efficient on an industrial scale and several routes have addressed the concern and achieved fast growth rates. Most notably, nanotubes 7 μm long have been grown in 15 s by the addition of 1.5 M lactic acid to the electrolyte solution (Table A- 2).³⁴ Addition of Na_2EDTA , H_2O_2 , and up to 0.5 M NH_4F have been used to increase the nanotube growth rate.^{30, 35, 36} Lactic acid and EDTA assist fluoride by chelating Ti^{4+} and H_2O_2 provides an alternate source for oxygen, possibly through radical species.^{30, 34, 36} Fast nanotube growth rates are also determined by a balance between water and fluoride concentration. High fluoride concentration (>0.1 M NH_4F) enhances the dissolution of TiO_2 by Equation (3), while addition of water allows for a sufficient rate of titanium oxidation by Equation (1). However, addition of water also slows the dissolution of titania by Equation (3) as supported by experimental results. Upon addition of 1% water to 0.5 M NH_4F in anhydrous ethylene glycol, the growth rate increased from 83 nm/min to 308 nm/min at 60 V but 2% water only increased the formation rate to 217 nm/min.⁴⁰

Table A- 2. Experimental conditions to achieve efficient lengths.

| Length (μm) | Duration | Electrolyte | Voltage (V) | Reference |
|--------------------------|----------|--|-------------|--------------------|
| 20 | 2 h | 0.09 M NH_4F ethylene glycol | 60 | ⁴⁵ (SI) |
| 20 | 0.5 h | 0.5 M NH_4F , 0.25 M Na_2EDTA , 5% water, ethylene glycol | 80 | ³⁰ |

Liu *et al.* used a theoretical model, based on the reduction of oxygen, to determine the most efficient dimensions of un-sensitized titania nanotubes for photocatalysis.⁴⁶ Based on the diffusion of oxygen and the molar absorptivity of TiO₂, the photocatalytic efficiency plateaus with nanotubes greater than 5 μm long (Figure A-6).⁴⁶ Experimental results show similar saturation behavior, albeit at longer nanotube lengths.⁴⁸⁻⁵¹ For example, un-sensitized nanotube arrays 12 μm long were most efficient for the degradation of gaseous benzene and toluene compared to nanotubes ranging from 800 nm to 12 μm in length.⁴⁸ Similarly, for the catalysis of acetaldehyde and phenol, the efficiency continued to increase with nanotube length ranging from 200 nm to 17 μm.^{49, 50}

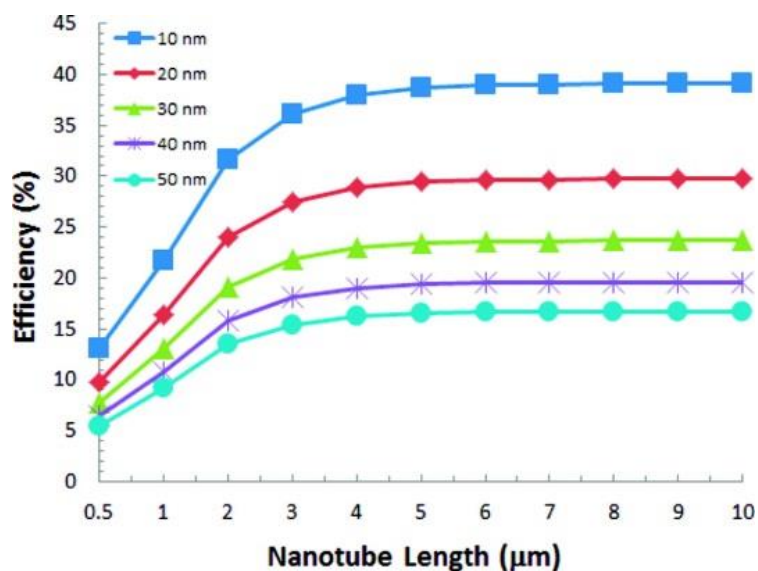


Figure A-6. Theoretically efficient nanotube lengths for the reduction of oxygen. The theoretical model considers un-sensitized nanotubes illuminated by UV light. The series corresponds to the inner radius of the nanotubes, ranging from 10 nm to 50 nm. Reprinted with permission from⁴⁶ Copyright 2012 American Chemical Society.

In solar cells using titania nanotubes as the photoanode, there is a balance between absorbing the most photons and reducing the distance the electron must travel in the nanotubes. In accordance with the Beer-Lambert law, more photons are harvested with longer nanotubes that can adsorb more dye or polymer (Figure A-4). However, longer nanotubes have more recombination centers, higher series resistance, and lower open circuit potentials.^{52, 53} Thus, to ensure efficient electron collection, optimized nanotubes lengths do not exceed the electron diffusion length, estimated to be 10–100 μm in titania nanotubes and 10 μm in nanoparticles.⁵³⁻⁵⁶

Experimental results demonstrate that the efficiency of hybrid solar cells employing nanotubes decreases after a certain length is exceeded (Figure A-7). Park *et al.* found that the photocurrent density increased with increasing TiO₂ nanotube length up to 35 μm and attributed the effect to the higher surface area for dye-loading.⁵⁷ Dubey *et al.* found that the photocurrent density and energy conversion efficiency were a maximum for 22 μm long nanotubes (16.3 mA/cm², 6.12%) and decreased at 38 μm because of increased recombination at surface defects.⁵⁸

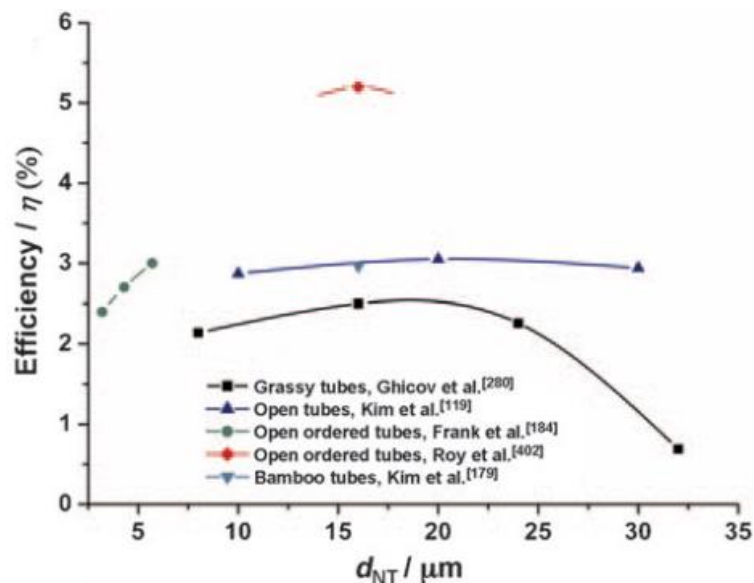


Figure A-7. Effect of the length of nanotubes in dye-sensitized solar cells (DSSCs) on the solar power conversion efficiency. Reprinted with permission from ³. Copyright 2011 Wiley.

2.1.2. Diameter and Wall Thickness

Although great control over the nanotube length has been demonstrated, primarily adjusted by the anodization duration, less systematic control over the nanotube diameter and wall thickness has been shown. The nanotube diameter mostly varies with the anodization voltage (Figure A-8),^{3, 28, 38, 41-43, 59} but also varies with the solvent,^{28, 31, 60} duration,^{38, 43} the water content,³⁵ and the fluoride concentration.^{11, 42} Nanotubes have been synthesized by anodization that range from 15 nm to 709 nm by adjusting the voltage, solvent, and duration as seen in Table A-3.^{31, 60}

Table A-3. Experimental conditions to achieve nanotubes with different inner diameters.

| Inner Diameter | Duration | Electrolyte | Voltage | Reference |
|----------------|----------|--|---------|-----------|
| 15 nm | 24 h | 0.2 M HF, 3.6% water, ethylene glycol | 10 V | 31 |
| 709 nm | 47 h | 0.25% HF, 1% water, diethylene glycol | 120 V | 60 |
| 80 nm | 1.5 h | 0.15 M NH ₄ F, 3% water, glycerol | 80 V | 28 |

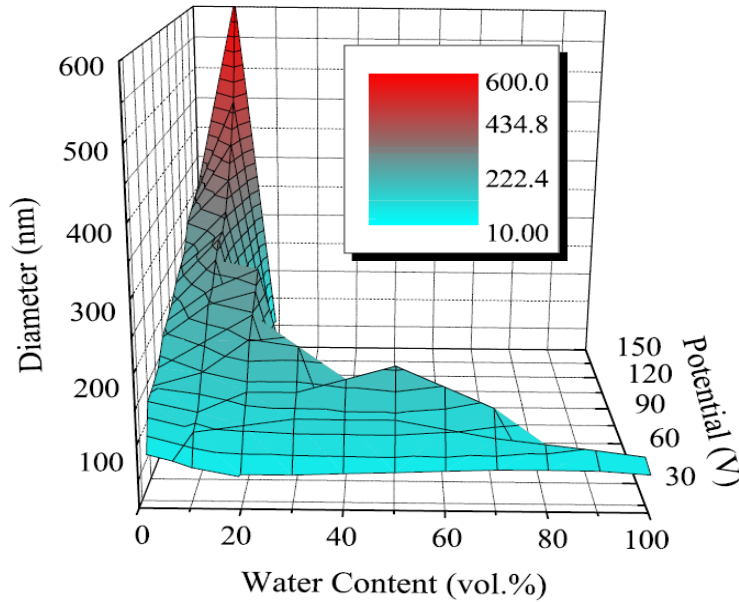


Figure A-8. Effect of water content and voltage on the nanotube diameter. Water content under 20% increases the nanotube diameter while limiting the voltage at which nanotubes are formed. Reprinted with permission from³⁵. Copyright 2010 IOP Publishing.

In addition to the nanotube length, the surface area and efficiency of a nanotube array are determined by the relationship between its diameter and wall thickness (Figure A-9).^{48, 61} Kontos *et al.* calculated the porosity of their nanotube arrays and compared it to the surface area per unit volume. It was calculated by

$$P = 1 - \frac{2\pi W(W + D)}{\sqrt{3}(2W + D)^2} \quad (4)$$

where W is the wall thickness and D is the inner diameter. Based the theoretical model used by Liu *et al.*, 20 nm is the most efficient inside diameter for photocatalysis of gaseous reactants (Figure A-6) and 20–30 nm, is the most efficient wall thickness.⁴⁶

In hybrid solar cells, the high surface area for contact between the electron donor and acceptor (titania) reduces the distance excitons must travel before electrons are collected at the donor-acceptor interface. Thus, excitons are less likely to decay and a higher incident-photon-to-current efficiency (IPCE) is expected, compared to planar solar cells of the same thickness. Exciton

diffusion lengths for commonly used organic polymer sensitizers are 8–20 nm for poly(3-hexylthiophene) (P3HT),²² 20 nm for the poly(*p*-phenylene vinylene) derivative MEH-PPV,²⁴ and 14 nm for ladder-type poly(*p*-phenylene).⁶²

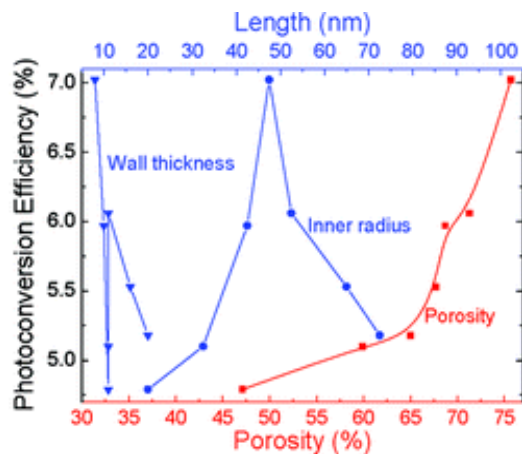


Figure A-9. Experimental effect of the porosity (determined by the wall thickness and diameter) on the photoconversion efficiency of water-splitting cells. Reprinted with permission from⁶¹. Copyright 2012 American Chemical Society.

Correspondingly, Ghicov *et al.* found that the nanotube diameter in DSSCs correlated with the solar cell's short circuit current and photoconversion efficiency, which was attributed to higher dye-loading due to higher surface area (Figure A-10).⁵² However, for polymeric sensitizers, small diameter nanotubes that have high porosity present an issue for polymer packing within the nanotubes. In the bulk, exciton mobility is enhanced by π - π stacking which allows excitons to delocalize over multiple polymer chains.⁶³ However, in confining nanotubes, disordered configurations are favored and π - π stacking is largely prevented.⁶³ Although So *et al.* report that changing the nanotube diameter within 100–200 nm has no significant effect on the solar cell efficiency, 100 nm diameter nanotubes are more efficient at certain lengths (Figure A-10).^{34, 52}

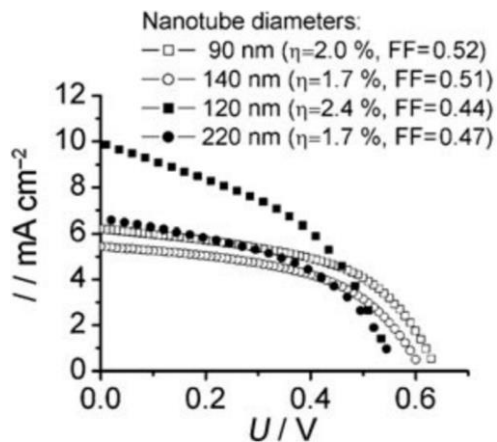


Figure A-10. Current-voltage characteristics of DSSCs based on different diameter nanotubes (empty symbols correspond to 8 μm and filled symbols to 16 μm nanotube length). Reprinted with permission from⁵². Copyright 2009 Wiley.

2.1.3. Nanotube Roughness and Intertube Spacing

Titania nanotubes with smooth walls are grown using viscous solvents for anodization. Solvents with high viscosity (Table A- 4) reduce the mobility of fluoride ions and other ionic species, reducing the growth rate, but also reducing current fluctuations and therefore forming smoother nanotube walls.^{28,33,40,64} The diffusion rate through a fluid is inversely proportional to the viscosity of the fluid according to the Stokes-Einstein equation:

$$D = \frac{k_B T}{6\pi\eta r} \quad (5)$$

where D is the diffusion coefficient of a particle with radius r , in a fluid with viscosity η , at temperature T , and k_B is the Boltzmann constant.^{14,28} Current fluctuations during the anodization process result from local inhomogenities of the concentration of ionic species, which cause rough nanotube walls to form.^{65,66}

Table A-4. Solvent viscosities.

| Electrolyte Solvent | glycerol | ethylene glycol | formamide | DMSO | water |
|------------------------------|----------|-----------------|-----------|------|-------|
| Viscosity (cP) ⁶⁷ | 934 | 16.1 | 3.34 | 1.99 | 0.89 |

Spacing between nanotubes, on the order of 100 nm, has been achieved by increasing the fluoride concentration and using di(ethylene glycol). Nanotube arrays grown in di(ethylene glycol) electrolytes have intertube space, but require 48 h of anodization to reach 7–20 μm in length.³³ Nanotubes spaced almost 1 μm apart have also been obtained by increasing the HF concentration to 4 wt % in ethylene glycol.⁶⁸

Well-ordered nanotube arrays with smooth walls and no intertube contact enhance electron transport by directing the injected electrons toward the conducting substrate and preventing undesired lateral transport between nanotubes.⁶⁹ Also, dyes or polymers can be adsorbed to the outside of the nanotubes if they are spaced apart, fully utilizing the available surface area. Intertube spacing smaller than that currently obtained (100 nm to 1 μm) should be more efficient by maximizing the number of nanotubes per unit area. However, no studies on the solar cell or photocatalytic efficiencies of nanotube arrays with any intertube space have been published.

2.2. Control of Crystallinity

Amorphous titania nanotubes have minimal use in solar energy applications due to the high concentration of recombination centers (Table A- 5, “unannealed”).^{11,41,70} The anatase crystalline

phase of titania is favored due to its higher electron mobility and larger surface area compared to the rutile phase.^{1, 10, 71, 72} Although titania nanotubes transformed to mostly rutile by annealing at 750 °C, the nanotubes collapse at that temperature, preventing the experimental comparison between pure rutile and pure anatase nanotubes.⁴¹ Rather, amorphous titania nanotubes are typically annealed at 450 °C in various atmospheres to form the anatase phase.⁵³ By annealing the nanotubes at temperatures between 450 °C and 750 °C, mixtures of anatase and rutile is formed.⁴¹

The annealing atmosphere affects the anatase-to-rutile phase transformation, and oxygen vacancies and other defects referred to as Ti⁺³ states, which lead to different recombination mechanisms and kinetics.^{10, 11, 73} Ti⁺³ states create an impurity band in the titania nanotubes and limit electron transport, but the number of Ti⁺³ states can be reduced by annealing the nanotubes in an oxygen rich atmosphere.⁷⁴ Dry atmospheres inhibit the transformation of anatase to rutile in the nanotube walls, while the interfacial region between the nanotubes and the Ti foil substrate transforms to rutile even at 430–450 °C, which may give the false indication that rutile is present throughout the nanotube array.^{10, 11}

Although uncollapsed pure rutile nanotubes have not been studied, mixed phase nanotubes have been shown to be more efficient for photocatalysis than pure anatase nanotubes. The photocatalytic degradation of methyl orange using titania nanotubes is enhanced with rutile/anatase mixing by annealing the nanotube array at 550 °C.⁷⁵ Likewise, photodegradation of toluene and rhodamine B by titania powder and nanofibers, respectively, is enhanced when both rutile and anatase are present (3/97 wt %) by using calcination temperatures ≥ 600 °C.^{76, 77} Water oxidation is also most efficient after annealing nanotubes at 580 °C where both phases are present.⁷⁸

Table A-5. Data from ⁴¹ on the photoconversion efficiency of un-sensitized titania nanotubes annealed at different temperatures in an oxygen atmosphere and illuminated under UV light. All of the samples were fabricated at 30 V for 3 h in 0.27 M NH₄F, 50 vol % glycerol in water.

| Annealing Temperature (°C) | unannealed | 350 | 450 | 550 | 650 | 750 |
|--------------------------------|------------|-------|-------|-------|-------|--------|
| Anatase/Rutile Mass Fraction | amorphous | 100/0 | 100/0 | 1/1.2 | 1/2.2 | 1/37.2 |
| Photoconversion Efficiency (%) | 1.4 | 5.86 | 5.93 | 7.25 | 8.56 | 0.4 |

To explain the mixed-phase phenomenon, Li *et al.* proposed that the rutile crystals provide electron trapping sites that extend the lifetime of photo-generated electron-hole pairs (Figure A-11).⁷⁶ However, Richter *et al.* found that rather than increasing the electron lifetime, the calcination temperature reduces the number of exciton-like trap states from oxygen vacancies, therefore improving electron transport.⁷⁴ Ghicov *et al.* attributed the mixed-phase phenomenon to increased crystallization at 600 °C, which minimized the number of recombination centers by reducing the amount of grain boundaries and amorphous TiO₂.¹¹

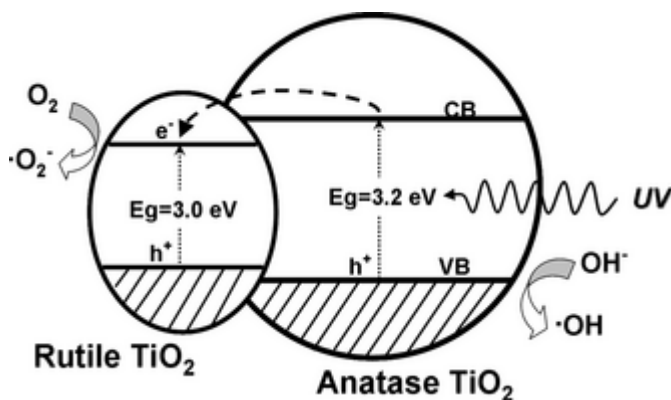


Figure A-11. Proposed schematic illustration of the band structure related to photocatalytic mechanism of un-sensitized mixed-phase TiO_2 structure. Reprinted with permission from⁷⁶. Copyright 2011 Wiley.

Although there are many studies on un-sensitized crystalline nanotubes, systematic studies of crystallinity on titania nanotube solar cells is lacking. However, the crystallinity of nanoparticles has been studied. Anatase nanoparticle films have a higher energy conversion efficiency (21%), photocurrent (30%), and electron diffusion length (10 \times) than rutile nanoparticle films of the same thickness.⁷⁹ The difference was partly attributed to the increased interparticle contact and dye loading from the higher surface area of the anatase nanoparticles.⁷⁹

3. Solar Cell Fabrication

Hybrid solar cells benefit from front-side illumination where light is incident on the transparent conducting oxide and immediately reaches the sensitized TiO_2 nanotube array (Figure A-12b,c).^{30, 45} In this orientation, reflection and absorption of light by the counter electrode and electrolyte are avoided. Nanotube arrays left on the titanium foil substrate can only be used in the less efficient back-side illuminated solar cell configuration, since the foil is opaque (Figure A-15a).^{30, 45} Two routes have been used to fabricate front-side illuminated solar cells with TiO_2 nanotube arrays: (1) transferring the nanotube array from the titanium foil to fluorine-doped tin oxide coated glass (FTO glass)^{45, 57} and (2) anodizing a film of titanium sputter-coated onto FTO glass.²⁸

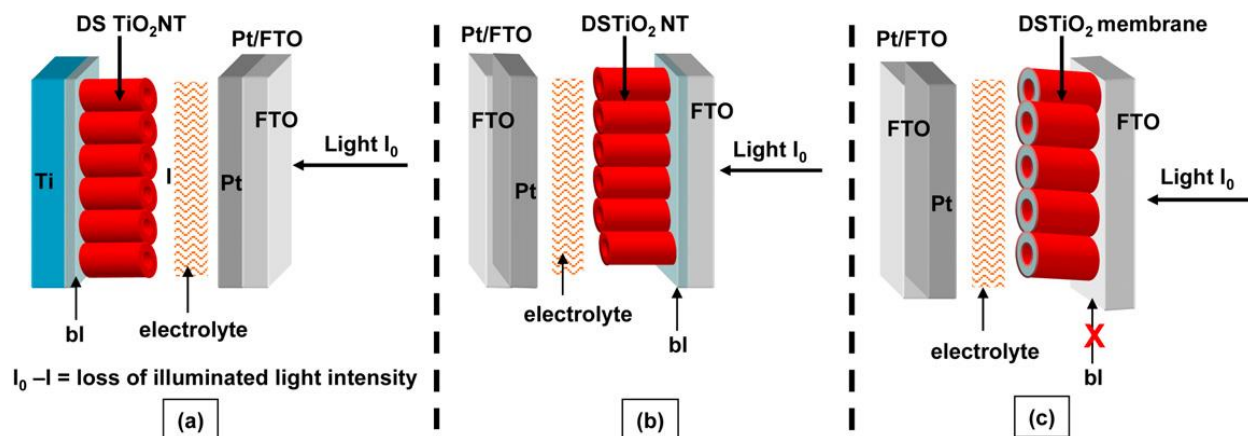


Figure A-12. Different orientations of DSSCs with TiO₂ nanotubes. “bl” represents the barrier layer of TiO₂ at the closed ends of the nanotubes. (a) Backside illumination with nanotubes on titanium foil; (b) Front-side illumination with nanotubes on fluorine-doped tin oxide coated glass (FTO glass); (c) Frontside illumination with nanotubes open on both ends. Reprinted with permission from³⁰. Copyright 2010 IOP Publishing.

3.1. Removing the Array

Titania nanotube arrays have been removed from the Ti by dissolution in a bromine/methanol solution,⁸⁰ aqueous HCl,^{57, 81} solvent-evaporation of methanol,⁸² ultrasonication in water,⁴³ acetone,⁸¹ ethanol/water solutions,⁸³ and drying in air.³⁰ After removing the nanotube array, it can be attached to FTO glass with a few drops of 100 mM titanium isopropoxide or a layer of TiO₂ nanoparticle paste 3 μm thick and then annealed (Figure A-13d).^{30, 57, 58, 76} Dubey *et al.* enhanced the adhesion by putting a 100 g weight onto the nanotube-FTO glass assembly in a freezer.⁵⁸

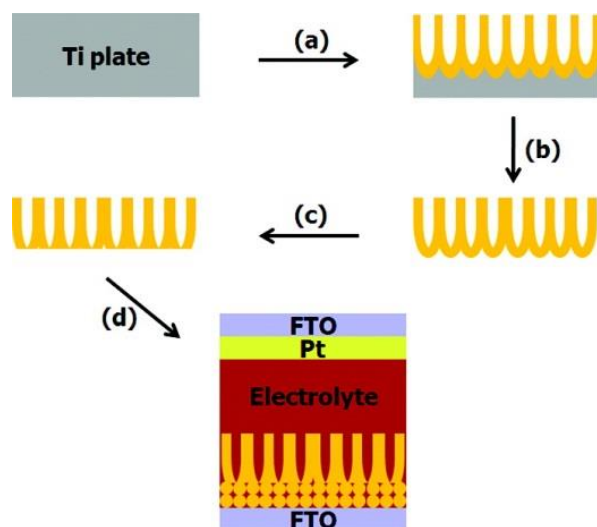


Figure A-13. Scheme illustrating the transfer of a nanotube array from titanium foil to FTO glass coated with TiO₂ nanoparticles for adhesion. Process (a) is the anodization; (b) the nanotube removal; (c) the removal of the barrier layer; and (d) the adhesion to FTO glass. Reprinted with permission from⁸⁴. Copyright 2012 American Chemical Society.

3.2. Anodizing on Conductive Substrates

Titania nanotubes have been grown by anodization of titanium films sputter-coated on alumina, indium-doped tin oxide⁸⁵ coated poly(ethylene terephthalate) (ITO PET),²⁸ fluorine-doped tin oxide coated glass.^{28, 45} Titania films 0.5 to 20 μm thick have been coated onto the conducting substrates by RF or DC magnetron sputtering and subsequently anodized in electrolytes containing fluoride to form nanotubes.²⁸ To improve the adhesion of titanium films to FTO glass, the glass is heated to 45–400 °C before deposition^{28, 45} and bombarded with Ar⁺ during deposition of the titanium films.⁴⁵ By bombarding the titanium film with ions during deposition, weakly bound titanium atoms are removed, leaving the titanium atoms strongly bound to the substrate.

3.3. Removal of Barrier Layer

The closed ends of the nanotubes (barrier layer), originally attached to the titanium foil hinder light absorption from front-side illuminated hybrid solar cells.^{30, 84} Although nanotubes grown directly on conductive substrates suffer from the light reflection by the barrier layer, the barrier layer can be removed from nanotube arrays transferred from titanium foil. After removing the nanotube array from the titanium foil, the barrier layer can be removed by HF etching³⁰ or ion milling,⁸⁴ similar to ion milling carbon nanotubes.⁸⁶ In the ion milling technique, the barrier layer is bombarded with Ar⁺ and removed by the sputtering process.

The barrier layer thickness decreases with increasing argon ion milling duration (0–90 min) and the barrier layer is perforated after 90 min as seen in Figure A-14d.⁸⁴ Under backside-illumination

of the ion milled N-719 sensitized solar cell, the photocurrent and energy conversion efficiency increased by 46% and 48% to 7.85 mA/cm^2 and 3.7% , respectively, after 90 min of ion milling the nanotubes. ⁸⁴ From electrochemical impedance spectroscopy measurements, Rho *et al.* determined that the barrier layer contributes to transport resistance in the nanotubes (Figure A-15). ⁸⁴ Since the open-circuit voltage, V_{oc} , is dependent on the recombination rate and there is no significant difference among the V_{oc} for different barrier thicknesses, only the electron transport rate is affected. ⁸⁴

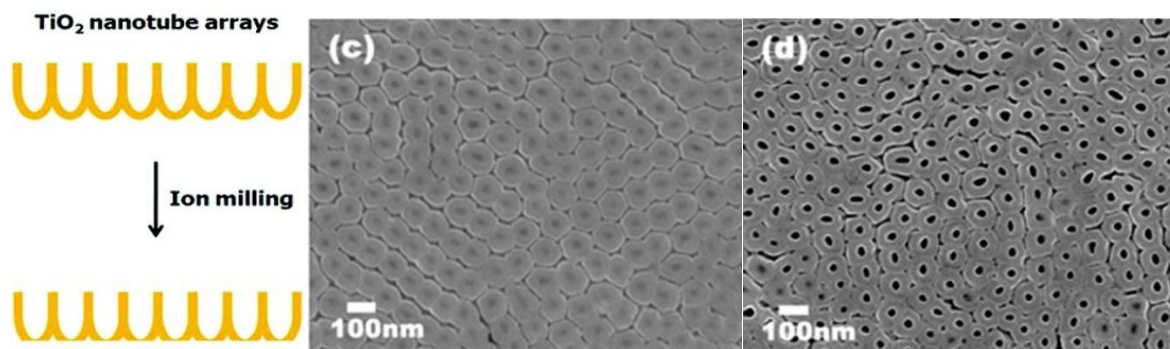


Figure A-14. SEM images of the closed-end/backside of TiO₂ nanotube arrays removed from the Ti foil after (c) 30 min and (d) 90 min of ion milling. Reprinted with permission from⁸⁴. Copyright 2012 American Chemical Society.

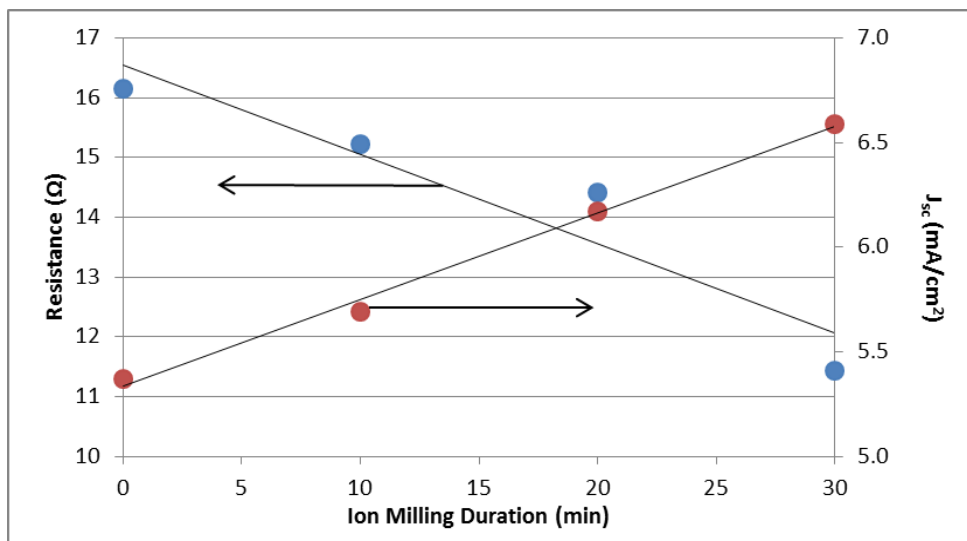


Figure A-15. Effect of argon ion milling duration on the nanotube transport resistance and short circuit current measured from electrochemical impedance spectra. The nanotubes were sensitized with N-719 dye and illuminated with AM 1.5 illumination. Data from ⁸⁴. Copyright 2012 American Chemical Society.

As an alternative to removing the barrier layer, Dubey *et al.* configured solar cells with the nanotube opening facing the FTO glass, effectively removing the barrier layer from the nanotube-FTO glass interface.⁵⁸ This configuration led to better contact with the FTO layer, higher photoconversion efficiencies ($\eta = 6.1\%$ vs. 3.8%), and open-circuit current densities, attributed to reduced recombination from better contact and twice the dye loading.⁵⁸ Dubey *et al.* achieved higher efficiencies with their inverse nanotube configuration than did Rho *et al.* with their ion milling technique (6.1% vs. 3.7%) using the same dye (N-719) and similar nanotube lengths ($22\ \mu\text{m}$ vs. $18\ \mu\text{m}$).⁸⁴ The adhesion of the inverse nanotube configuration to the FTO glass may be superior to the ion milled nanotubes since Dubey *et al.* applied pressure and cold temperatures as described in Section 3.1.

4. Conclusions

The extensive research on anodized titania nanotube arrays has led to steady improvements of its morphological control.^{3, 25} A wide range of nanotube array dimensions have been grown and tested in various solar energy conversion applications for optimum performance (Table A- 1). Great advances have been made in controlling the nanotube length since the first anodized titania nanotube report, but systematically controlling the nanotube diameter and wall thickness to the narrow dimensions that are theoretically efficient requires continued research. Considering that the titania nanotubes' crystallinity drastically affects its photoconversion efficiency and electron dynamics, the electron behavior in mixed-phase nanotubes requires attention to resolve disagreement in the literature.^{11, 74, 76} Studies on hybrid solar cells with mixed-phase titania nanotubes may contribute to the understanding of the mixed-phase phenomenon in un-sensitized nanotubes.

Further optimization and characterization of the attachment of nanotube arrays to conductive substrates could benefit electron transport by reducing transport resistance between the phases.^{28, 38, 58} For BHJs, improving polymer π - π packing and preventing phase separation with titania is needed to fully utilize the surface area available in the nanotubes and enhance photoconversion efficiencies.²¹

Acknowledgments

The authors acknowledge Oak Ridge Associated Universities for the Ralph E. Powe Junior Faculty Enhancement Award and the partial sponsorship by the Laboratory Directed Research and Development (LDRD) and SEED Program of Oak Ridge National Laboratory (ORNL), managed by UT-Battelle, LLC for the U.S. Department of Energy under Contract No. DE-AC05-00OR22725.

References

1. Park, J. T.; Patel, R.; Jeon, H.; Kim, D. J.; Shin, J.-S.; Kim, J. H., Facile Fabrication of vertically aligned TiO₂ nanorods with high density and rutile/anatase phases on transparent conducting glasses: high efficiency dye-sensitized solar cells. *Journal of Materials Chemistry* **2012**, *22*, 6131-6138.
2. Chen, R.; Chen, C.; Tsai, H.; Wang, W.; Huang, Y., Ultrahigh efficient single-crystalline TiO₂ nanorod photoconductors. *Applied Physics Letters* **2012**, *100*, 123108.
3. Roy, P.; Berger, S.; Schmuki, P., TiO₂ nanotubes: synthesis and applications. *Angewandte Chemie International Edition* **2011**, *50*, 2904-2939.
4. Lockman, Z.; Ismail, S.; Sreekantan, S.; Schmidt-Mende, L.; MacManus-Driscoll, J. L., The rapid growth of 3 μm long titania nanotubes by anodization of titanium in a neutral electrochemical bath. *Nanotechnology* **2009**, *21*, 055601.
5. Paulose, M.; Mor, G. K.; Varghese, O. K.; Shankar, K.; Grimes, C. A., Visible light photoelectrochemical and water-photoelectrolysis properties of titania nanotube arrays. *Journal of Photochemistry and Photobiology A: Chemistry* **2006**, *178*, 8-15.
6. Li, Y.; Yu, X.; Yang, Q., Fabrication of Nanotube Thin Films and Their Gas Sensing Properties. *Journal of Sensors* **2009**, *2009*.
7. Lu, X.; Wang, G.; Zhai, T.; Yu, M.; Gan, J.; Tong, Y.; Li, Y., Hydrogenated TiO₂ nanotube arrays for supercapacitors. *Nano letters* **2012**, *12*, 1690-1696.
8. Zwillig, V.; Aucouturier, M.; Darque-Ceretti, E., Anodic oxidation of titanium and TA6V alloy in chromic media. An electrochemical approach. *Electrochimica Acta* **1999**, *45*, 921-929.
9. Gong, D.; Grimes, C. A.; Varghese, O. K.; Hu, W.; Singh, R.; Chen, Z.; Dickey, E. C., Titanium oxide nanotube arrays prepared by anodic oxidation. *Journal of Materials Research* **2001**, *16*, 3331-3334.
10. Varghese, O. K.; Gong, D.; Paulose, M.; Grimes, C. A.; Dickey, E. C., Crystallization and high-temperature structural stability of titanium oxide nanotube arrays. *Journal of Materials Research* **2003**, *18*, 156-165.

11. Ghicov, A.; Tsuchiya, H.; Macak, J. M.; Schmuki, P., Annealing effects on the photoresponse of TiO₂ nanotubes. *Physica Status Solidi (a)* **2006**, *203*, R28-R30.
12. Fabregat-Santiago, F.; Barea, E. M.; Bisquert, J.; Mor, G. K.; Shankar, K.; Grimes, C. A., High carrier density and capacitance in TiO₂ nanotube arrays induced by electrochemical doping. *Journal of the American Chemical Society* **2008**, *130*, 11312-11316.
13. Morris, A. J.; Meyer, G. J., TiO₂ surface functionalization to control the density of states. *The Journal of Physical Chemistry C* **2008**, *112*, 18224-18231.
14. Sturgeon, M. R.; Lai, P.; Hu, M. Z., A comparative study of anodized titania nanotube architectures in aqueous and nonaqueous solutions. *Journal of Materials Research* **2011**, *26*, 2612-2623.
15. Fujishima, A., Electrochemical photolysis of water at a semiconductor electrode. *Nature* **1972**, *238*, 37-38.
16. Yun, H. J.; Lee, H.; Joo, J. B.; Kim, N. D.; Yi, J., Effect of TiO₂ nanoparticle shape on hydrogen evolution via water splitting. *Journal of Nanoscience and Nanotechnology* **2011**, *11*, 1688-1691.
17. Wolcott, A.; Smith, W. A.; Kuykendall, T. R.; Zhao, Y.; Zhang, J. Z., Photoelectrochemical water splitting using dense and aligned TiO₂ nanorod arrays. *Small* **2009**, *5*, 104-111.
18. Zhang, Z.; Wang, P., Optimization of photoelectrochemical water splitting performance on hierarchical TiO₂ nanotube arrays. *Energy & Environmental Science* **2012**, *5*, 6506-6512.
19. Ghicov, A.; Schmuki, P., Self-ordering electrochemistry: a review on growth and functionality of TiO₂ nanotubes and other self-aligned MO_x structures. *Chemical Communications* **2009**, 2791-2808.
20. Yan, J.; Zhou, F., TiO₂ nanotubes: structure optimization for solar cells. *Journal of Materials Chemistry* **2011**, *21*, 9406-9418.
21. Tepavcevic, S.; Darling, S. B.; Dimitrijevic, N. M.; Rajh, T.; Sibener, S. J., Improved hybrid solar cells via in situ UV polymerization. *Small* **2009**, *5*, 1776-1783.

22. Ayzner, A. L.; Tassone, C. J.; Tolbert, S. H.; Schwartz, B. J., Reappraising the need for bulk heterojunctions in polymer– fullerene photovoltaics: the role of carrier transport in all-solution-processed P3HT/PCBM bilayer solar cells. *The Journal of Physical Chemistry C* **2009**, *113*, 20050-20060.
23. Yella, A.; Lee, H.-W.; Tsao, H. N.; Yi, C.; Chandiran, A. K.; Nazeeruddin, M. K.; Diao, E. W.-G.; Yeh, C.-Y.; Zakeeruddin, S. M.; Grätzel, M., Porphyrin-sensitized solar cells with cobalt (II/III)–based redox electrolyte exceed 12 percent efficiency. *Science* **2011**, *334*, 629-634.
24. Kannan, B.; Castelino, K.; Majumdar, A., Design of nanostructured heterojunction polymer photovoltaic devices. *Nano Letters* **2003**, *3*, 1729-1733.
25. Roy, P.; Kim, D.; Lee, K.; Spiecker, E.; Schmuki, P., TiO₂ nanotubes and their application in dye-sensitized solar cells. *Nanoscale* **2010**, *2*, 45-59.
26. Bouclé, J.; Ackermann, J., Solid-state dye-sensitized and bulk heterojunction solar cells using TiO₂ and ZnO nanostructures: recent progress and new concepts at the borderline. *Polymer International* **2012**, *61*, 355-373.
27. Li, S.; Zhang, G.; Guo, D.; Yu, L.; Zhang, W., Anodization fabrication of highly ordered TiO₂ nanotubes. *The Journal of Physical Chemistry C* **2009**, *113*, 12759-12765.
28. Galstyan, V.; Vomiero, A.; Comini, E.; Faglia, G.; Sberveglieri, G., TiO₂ nanotubular and nanoporous arrays by electrochemical anodization on different substrates. *RSC Advances* **2011**, *1*, 1038-1044.
29. Zhang, G.; Huang, H.; Zhang, Y.; Chan, H. L.; Zhou, L., Highly ordered nanoporous TiO₂ and its photocatalytic properties. *Electrochemistry Communications* **2007**, *9*, 2854-2858.
30. Banerjee, S.; Misra, M.; Mohapatra, S. K.; Howard, C.; Mohapatra, S. K.; Kamilla, S. K., Formation of chelating agent driven anodized TiO₂ nanotubular membrane and its photovoltaic application. *Nanotechnology* **2010**, *21*, 145201.
31. Liu, N.; Lee, K.; Schmuki, P., Small diameter TiO₂ nanotubes vs. nanopores in dye sensitized solar cells. *Electrochemistry Communications* **2012**, *15*, 1-4.

32. Alivov, Y.; Pandikunta, M.; Nikishin, S.; Fan, Z., The anodization voltage influence on the properties of TiO₂ nanotubes grown by electrochemical oxidation. *Nanotechnology* **2009**, *20*, 225602.
33. Yoriya, S.; Mor, G. K.; Sharma, S.; Grimes, C. A., Synthesis of ordered arrays of discrete, partially crystalline titania nanotubes by Ti anodization using diethylene glycol electrolytes. *Journal of Material Chemistry* **2008**, *18*, 3332-3336.
34. So, S.; Lee, K.; Schmuki, P., Ultrafast growth of highly ordered anodic TiO₂ nanotubes in lactic acid electrolytes. *Journal of the American Chemical Society* **2012**, *134*, 11316-11318.
35. Yin, H.; Liu, H.; Shen, W., The large diameter and fast growth of self-organized TiO₂ nanotube arrays achieved via electrochemical anodization. *Nanotechnology* **2009**, *21*, 035601.
36. Sreekantan, S.; Wei, L. C.; Lockman, Z., Extremely fast growth rate of TiO₂ nanotube arrays in electrochemical bath containing H₂O₂. *Journal of the Electrochemical Society* **2011**, *158*, C397-C402.
37. Lee, K.; Kim, J.; Kim, H.; Lee, Y.; Tak, Y.; Kim, D.; Schmuki, P., Effect of electrolyte conductivity on the formation of a nanotubular TiO₂ photoanode for a dye-sensitized solar cell. *Journal of the Korean Physical Society* **2009**, *54*, 1027-1031.
38. Portan, D.; Papaefthymiou, K.; Arvanita, E.; Jiga, G.; Papanicolaou, G., A combined statistical and microscopic analysis of TiO₂ nanotubes synthesized under different electrochemical anodizing conditions. *Journal of Materials Science* **2012**, *47*, 4696-4705.
39. Chin, L. Y.; Zainal, Z.; Hussein, M. Z.; Tee, T. W., Fabrication of highly ordered TiO₂ nanotubes from fluoride containing aqueous electrolyte by anodic oxidation and their photoelectrochemical response. *Journal of Nanoscience and Nanotechnology* **2011**, *11*, 4900-4909.
40. Sreekantan, S.; Saharudin, K. A.; Lockman, Z.; Tzu, T. W., Fast-rate formation of TiO₂ nanotube arrays in an organic bath and their applications in photocatalysis. *Nanotechnology* **2010**, *21*, 365603.
41. Li, D.; Lin, S.; Li, S.; Huang, X.; Cao, X.; Li, J., Effects of geometric and crystal structures on the photoelectrical properties of highly ordered TiO₂ nanotube arrays. *Journal of Materials Research* **2012**, *27*, 1029-1036.

42. Yoriya, S.; Paulose, M.; Varghese, O. K.; Mor, G. K.; Grimes, C. A., Fabrication of vertically oriented TiO₂ nanotube arrays using dimethyl sulfoxide electrolytes. *The Journal of Physical Chemistry C* **2007**, *111*, 13770-13776.
43. Prakasam, H. E.; Shankar, K.; Paulose, M.; Varghese, O. K.; Grimes, C. A., A new benchmark for TiO₂ nanotube array growth by anodization. *The Journal of Physical Chemistry C* **2007**, *111*, 7235-7241.
44. Lai, C. W.; Sreekantan, S., Effect of applied potential on the formation of self-organized TiO₂ nanotube arrays and its photoelectrochemical response. *Journal of Nanomaterials* **2011**, *2011*, 11.
45. Varghese, O. K.; Paulose, M.; Grimes, C. A., Long vertically aligned titania nanotubes on transparent conducting oxide for highly efficient solar cells. *Nature Nanotechnology* **2009**, *4*, 592-597.
46. Liu, B.; Nakata, K.; Liu, S.; Sakai, M.; Ochiai, T.; Murakami, T.; Takagi, K.; Fujishima, A., Theoretical kinetic analysis of heterogeneous photocatalysis by TiO₂ nanotube arrays: the effects of nanotube geometry on photocatalytic activity. *The Journal of Physical Chemistry C* **2012**, *116*, 7471-7479.
47. Paulose, M.; Prakasam, H. E.; Varghese, O. K.; Peng, L.; Papat, K. C.; Mor, G. K.; Desai, T. A.; Grimes, C. A., TiO₂ nanotube arrays of 1000 μm length by anodization of titanium foil: phenol red diffusion. *The Journal of Physical Chemistry C* **2007**, *111*, 14992-14997.
48. Kontos, A.; Katsanaki, A.; Maggos, T.; Likodimos, V.; Ghicov, A.; Kim, D.; Kunze, J.; Vasilakos, C.; Schmuki, P.; Falaras, P., Photocatalytic degradation of gas pollutants on self-assembled titania nanotubes. *Chemical Physics Letters* **2010**, *490*, 58-62.
49. Liu, Z.; Zhang, X.; Nishimoto, S.; Murakami, T.; Fujishima, A., Efficient photocatalytic degradation of gaseous acetaldehyde by highly ordered TiO₂ nanotube arrays. *Environmental Science & Technology* **2008**, *42*, 8547-8551.
50. Liu, Z.; Zhang, X.; Nishimoto, S.; Jin, M.; Tryk, D. A.; Murakami, T.; Fujishima, A., Highly ordered TiO₂ nanotube arrays with controllable length for photoelectrocatalytic degradation of phenol. *The Journal of Physical Chemistry C* **2008**, *112*, 253-259.
51. Zhuang, H.-F.; Lin, C.-J.; Lai, Y.-K.; Sun, L.; Li, J., Some critical structure factors of titanium oxide nanotube array in its photocatalytic activity. *Environmental Science & Technology* **2007**, *41*, 4735-4740.

52. Ghicov, A.; Albu, S. P.; Hahn, R.; Kim, D.; Stergiopoulos, T.; Kunze, J.; Schiller, C. A.; Falaras, P.; Schmuki, P., TiO₂ nanotubes in dye-sensitized solar cells: Critical factors for the conversion efficiency. *Chemistry—An Asian Journal* **2009**, *4*, 520-525.
53. Jennings, J. R.; Ghicov, A.; Peter, L. M.; Schmuki, P.; Walker, A. B., Dye-sensitized solar cells based on oriented TiO₂ nanotube arrays: transport, trapping, and transfer of electrons. *Journal of the American Chemical Society* **2008**, *130*, 13364-13372.
54. Peter, L., Transport, trapping and interfacial transfer of electrons in dye-sensitized nanocrystalline solar cells. *Journal of Electroanalytical Chemistry* **2007**, *599*, 233-240.
55. Kang, S. H.; Kim, H. S.; Kim, J.-Y.; Sung, Y.-E., An investigation on electron behavior employing vertically-aligned TiO₂ nanotube electrodes for dye-sensitized solar cells. *Nanotechnology* **2009**, *20*, 355307.
56. Leng, W.; Barnes, P. R.; Juozapavicius, M.; O'Regan, B. C.; Durrant, J. R., Electron diffusion length in mesoporous nanocrystalline TiO₂ photoelectrodes during water oxidation. *The Journal of Physical Chemistry Letters* **2010**, *1*, 967-972.
57. HyeokáPark, J.; GuáKang, M., Growth, detachment and transfer of highly-ordered TiO₂ nanotube arrays: use in dye-sensitized solar cells. *Chemical Communications* **2008**, 2867-2869.
58. Dubey, M.; Shrestha, M.; Zhong, Y.; Galipeau, D.; He, H., TiO₂ nanotube membranes on transparent conducting glass for high efficiency dye-sensitized solar cells. *Nanotechnology* **2011**, *22*, 285201.
59. Dale, G.; Hamilton, J.; Dunlop, P.; Lemoine, P.; Byrne, J., Electrochemical growth of titanium oxide nanotubes: the effect of surface roughness and applied potential. *Journal of Nanoscience and Nanotechnology* **2009**, *9*, 4215-4219.
60. Mohammadpour, A.; Shankar, K., Anodic TiO₂ nanotube arrays with optical wavelength-sized apertures. *Journal of Materials Chemistry* **2010**, *20*, 8474-8477.
61. Liang, S.; He, J.; Sun, Z.; Liu, Q.; Jiang, Y.; Cheng, H.; He, B.; Xie, Z.; Wei, S., Improving photoelectrochemical water splitting activity of TiO₂ nanotube arrays by tuning geometrical parameters. *The Journal of Physical Chemistry C* **2012**, *116*, 9049-9053.

62. Haugeneder, A.; Neges, M.; Kallinger, C.; Spirkl, W.; Lemmer, U.; Feldmann, J.; Scherf, U.; Harth, E.; Gügel, A.; Müllen, K., Exciton diffusion and dissociation in conjugated polymer/fullerene blends and heterostructures. *Physical Review B* **1999**, *59*, 15346.
63. Coakley, K. M.; Liu, Y.; McGehee, M. D.; Frindell, K. L.; Stucky, G. D., Infiltrating Semiconducting Polymers into Self-assembled Mesoporous Titania Films for Photovoltaic Applications. *Advanced Functional Materials* **2003**, *13*, 301-306.
64. Macak, J. M.; Tsuchiya, H.; Taveira, L.; Aldabergerova, S.; Schmuki, P., Smooth anodic TiO₂ nanotubes. *Angewandte Chemie International Edition* **2005**, *44*, 7463-7465.
65. Macak, J. M.; Tsuchiya, H.; Schmuki, P., High-aspect-ratio TiO₂ nanotubes by anodization of titanium. *Angewandte Chemie International Edition* **2005**, *44*, 2100-2102.
66. Balaur, E.; Macak, J. M.; Tsuchiya, H.; Schmuki, P., Wetting behaviour of layers of TiO₂ nanotubes with different diameters. *Journal of Materials Chemistry* **2005**, *15*, 4488-4491.
67. Haynes, W. M., *CRC Handbook of Chemistry and Physics, 93rd Edition*. Taylor & Francis: 2012.
68. Chen, Y.; Lu, H.-h.; Wang, X.-m.; Lu, S.-s., Large-scale sparse TiO₂ nanotube arrays by anodization. *Journal of Materials Chemistry* **2012**, *22*, 5921-5923.
69. Zhu, K.; Vinzant, T. B.; Neale, N. R.; Frank, A. J., Removing structural disorder from oriented TiO₂ nanotube arrays: reducing the dimensionality of transport and recombination in dye-sensitized solar cells. *Nano Letters* **2007**, *7*, 3739-3746.
70. Allam, N. K.; Grimes, C. A., Room temperature one-step polyol synthesis of anatase TiO₂ nanotube arrays: photoelectrochemical properties. *Langmuir* **2009**, *25*, 7234-7240.
71. Lee, K.; Kim, D.; Roy, P.; Paramasivam, I.; Birajdar, B. I.; Spiecker, E.; Schmuki, P., Anodic formation of thick anatase TiO₂ mesosponge layers for high-efficiency photocatalysis. *Journal of the American Chemical Society* **2010**, *132*, 1478-1479.
72. Liu, B.; Khare, A.; Aydil, E. S., Synthesis of single-crystalline anatase nanorods and nanoflakes on transparent conducting substrates. *Chemical Communications* **2012**, *48*, 8565-8567.

73. Fàbrega, C.; Hernández-Ramírez, F.; Prades, J. D.; Jiménez-Díaz, R.; Andreu, T.; Morante, J. R., On the photoconduction properties of low resistivity TiO₂ nanotubes. *Nanotechnology* **2010**, *21*, 445703.
74. Richter, C.; Schmuttenmaer, C. A., Exciton-like trap states limit electron mobility in TiO₂ nanotubes. *Nature Nanotechnology* **2010**, *5*, 769-772.
75. Liao, Y.; Que, W., Preparation and photocatalytic activity of TiO₂ nanotube powders derived by a rapid anodization process. *Journal of Alloys and Compounds* **2010**, *505*, 243-248.
76. Li, H.; Zhang, W.; Pan, W., Enhanced photocatalytic activity of electrospun TiO₂ nanofibers with optimal anatase/rutile ratio. *Journal of the American Ceramic Society* **2011**, *94*, 3184-3187.
77. Berry, R. J.; Mueller, M. R., Photocatalytic decomposition of crude oil slicks using TiO₂ on a floating substrate. *Microchemical Journal* **1994**, *50*, 28-32.
78. Allam, N. K.; El-Sayed, M. A., Photoelectrochemical water oxidation characteristics of anodically fabricated TiO₂ nanotube arrays: structural and optical properties. *The Journal of Physical Chemistry C* **2010**, *114*, 12024-12029.
79. Park, N.-G.; Van de Lagemaat, J.; Frank, A., Comparison of dye-sensitized rutile-and anatase-based TiO₂ solar cells. *The Journal of Physical Chemistry B* **2000**, *104*, 8989-8994.
80. Albu, S. P.; Ghicov, A.; Macak, J. M.; Hahn, R.; Schmuki, P., Self-organized, free-standing TiO₂ nanotube membrane for flow-through photocatalytic applications. *Nano Letters* **2007**, *7*, 1286-1289.
81. Lai, C. W.; Sreekantan, S., Photoelectrochemical performance of smooth TiO₂ nanotube arrays: effect of anodization temperature and cleaning methods. *International Journal of Photoenergy* **2012**, *2012*.
82. Wang, J.; Lin, Z., Freestanding TiO₂ nanotube arrays with ultrahigh aspect ratio via electrochemical anodization. *Chemistry of Materials* **2008**, *20*, 1257-1261.
83. Chen, Q.; Xu, D.; Wu, Z.; Liu, Z., Free-standing TiO₂ nanotube arrays made by anodic oxidation and ultrasonic splitting. *Nanotechnology* **2008**, *19*, 365708.

84. Rho, C.; Min, J.-H.; Suh, J. S., Barrier layer effect on the electron transport of the dye-sensitized solar cells based on TiO₂ nanotube arrays. *The Journal of Physical Chemistry C* **2012**, *116*, 7213-7218.
85. Kim, D.; Lee, K.; Roy, P.; Birajdar, B. I.; Spiecker, E.; Schmuki, P., Formation of a non-thickness-limited titanium dioxide mesosponge and its use in dye-sensitized solar cells. *Angewandte Chemie* **2009**, *121*, 9490-9493.
86. Jung, H. Y.; Jung, S. M.; Gu, G. H.; Suh, J. S., Anodic aluminum oxide membrane bonded on a silicon wafer for carbon nanotube field emitter arrays. *Applied Physics Letters* **2006**, *89*, 13121-13500.